Stony Brook University

High Resolution Chemical Mapping via Scanning Transmission X-ray Microscopy

A Dissertation Presented

by

Holger Fleckenstein

to

The Graduate School

in Partial Fulfillment of the Requirements

for the Degree of

Doctor of Philosophy

in

Physics

Stony Brook University

August 2008

Stony Brook University

The Graduate School

Holger Fleckenstein

We, the dissertation committee for the above candidate for the Doctor of Philosophy degree, hereby recommend acceptance of this dissertation.

Chris Jacobsen – Dissertation Advisor
Professor, Department of Physics and Astronomy

Adam Durst – Chairperson of Defense
Assistant Professor, Department of Physics and Astronomy

Dominik Schneble
Assistant Professor, Department of Physics and Astronomy

Antonio Lanzirotti
Senior Research Associate
Consortium for Advanced Radiation Sources, The University of Chicago

This dissertation is accepted by the Graduate School.

Lawrence Martin
Dean of the Graduate School

Abstract of the Dissertation

High Resolution Chemical Mapping via Scanning Transmission X-ray Microscopy

by

Holger Fleckenstein

Doctor of Philosophy

in

Physics

Stony Brook University

2008

Scanning transmission x-ray microscopy (STXM) combines imaging at sub-50 nanometer spatial resolution in the soft x-ray region with x-ray absorption spectroscopy at an energy resolution of 0.1 eV and better. The sensitivity to light elements and their chemical bonding states in the near-edge x-ray absorption region together with 2D microscopy allow to map out the chemical composition of microscopic samples. Over the past decades STXM has been used by scientists from various fields such as material sciences, biology, earth and environmental sciences.

This thesis describes the upgrade of the STXM microscopes at the National Synchrotron Light Source in Brookhaven National Laboratory. The now 5^{th} generation was a retrofit of the existing microscopes with a three axes laser interferometer system for improved relative sample positioning. Included in the same project were a hardware change towards faster scan positioning and data acquisition electronics as well as a new software concept allowing

for remote control of the microscopes.

We also present the use of non-negative matrix factorization to analyze spectromicroscopic data sets. Since in many specimens of interest in biology or related fields a number of spectral signatures may be unknown, thickness maps of the chemical composition of a sample cannot be calculated directly. A previous method used principal component analysis to orthogonalize and noise filter spectromicroscopy data, followed by cluster analysis as a form of unsupervised pattern recognition to determine pixels with spectroscopic similarity. We tried a non-negative matrix factorization algorithm to find a parts-based representation of the same data. The non-negativity constraint allows for a physical interpretation of component spectra and thickness maps.

The STXM technique was utilized to investigate the composition of human sperm samples. We describe why the analysis of human sperm via x-ray spectromicroscopy can provide valuable information and what the results of our efforts were.

Contents

List of Figures

List of Tables

Acknowledgements

A big chapter of my life is drawing to an end and there are so many people whom I have to thank for their support and encouragement on the way. Without them I would not have made it!

I would like to say thanks to my advisor Chris Jacobsen for his guidance throughout my years in Stony Brook. Not only has he been a role model for his seemingly endless scientific interest and energy, also his friendly and encouraging nature guaranteed for a very pleasant work atmosphere. In addition he gave me and his other students ample opportunities to broaden our horizons at summer schools or workshops and to present our work at meetings and conferences.

Thanks to Sue Wirick for being my surrogate mom. She truly is the good soul of beamline X1A, making life on the experimental floor so much better with her kind and warm manner. Her generosity as well as her willingness to work after hours and on weekends to support users and students are without compare. "So long, and thanks for all the food!"

Benjamin Hornberger was my peer and good friend all throughout grad school. He was always willing to answer questions about IDL programming or general computer issues. We had many interesting discussions (not exclusively on physics) and problems solved. The same goes for Mirna Lerotić, who I worked with on the STXM 5 upgrade. During our good team work we had many delicious sushi lunches together with Sue.

Thanks to Tobias Beetz and Michael Feser for all the help received at my start-up into the world of x-rays, as well as to all other members of the Stony Brook X-ray Microscopy group during my time: Daniel Flickinger, Marc Häming, Christian Holzner, Xiaojing Huang, Bjorg Larson (my most reliable source in matters of the English language), Enju Lima, Ming Lu, Huijie Miao, Simon

Moser, Johanna Nelson, David Shapiro, Aaron Stein, Jan Steinbrener, Andrew Stewart and Joshua Turner. With many of them I established ties beyond the work place.

It was my special pleasure to work with Janos Kirz - alas on too few occasions since he left Stony Brook. He is an extraordinary physicist and outstanding personality, whose wisdom is only surpassed by his modesty.

The work on human sperm was done in collaboration with Yefim Sheynkin, urologist at Stony Brook University Hospital.

We thank NIH-NIBIB for its support of this work under grant *R01 EB00479-01A1*. We also thank the staff of the National Synchrotron Light Source (NSLS) at Brookhaven National Lab for their assistance, and the Department of Energy for its support of the NSLS.

My first three years of physics education I received at the University of Würzburg. The Physics Department there is maintaining an excellent exchange program with many universities in the US. I am thankful for their help in organizing my first year in Stony Brook as well as the financial support that I received during this period from the German Academic Exchange Service (DAAD).

I can't but mention Meghan Sumner (including Tobi, Noa and now Sylvie) my best friend in Stony Brook. She always had an open ear for all my problems outside of physics. Thanks for countless lunches, game nights, fun days, walks and talks!

Tüzer, Aleks, Natalia, Saša, Juana, Heather and all other friends who I can't list here I want to thank for numerous pleasant moments.

For many years the Stony Brook Gospel Choir and all its members gave me great joy and experiences that I will treasure for the rest of my life.

I am thankful to Allie and the other Lees for being my family over the past two years. You made me feel like in a bunch again!

Finally, I am immensely grateful to both my parents, my sister and the whole rest of my family in Germany for all their love and support throughout my entire life. I love you and you will always be in my heart, wherever my path will lead me.

Chapter 1

Introduction

This thesis is about the use of soft x-rays for absorption spectroscopy and microscopy. In this chapter, we begin with a discussion of x-ray sources, absorption spectroscopy and focusing, laying the groundwork for subsequent chapters.

1.1 X-ray sources

X-rays were discovered by Wilhelm Conrad Röntgen in 1895 in experiments using Hittorf-Crookes tubes, where an electron beam hitting a metal target generated x-rays, which were able to escape through the thin tube wall. Specialized x-ray tubes have since been developed. They are based on electrons impacting on a metal anode (often tungsten). The deceleration of the electrons in the metal gives rise to the emission of a continuous spectrum of x-rays called Bremsstrahlung. The Bremsstrahlungs background is overlaid with a series of emission peaks, that are characteristic for the anode material. When the impact of an incoming electron removes an inner shell electron from the metal, an outer shell electron can take its place. In this process characteristic photons are emitted.

While x-ray tubes are still being heavily used today for medical imaging for example, modern x-ray sources with high intensities, brightness and coherence have made whole new fields of science possible. They are based on charged particles (electrons in modern sources) at high energies in vacuum being accelerated by electric and magnetic fields and thus emitting photons. In first generation sources the x-rays were a mere byproduct of particle accelerators. The National Synchrotron Light Source (NSLS) at Brookhaven National Lab (BNL) was then designed in the late 1970's as a second generation source dedicated to produce x-rays only. Newer synchrotrons with improved technology are referred to as third generation sources. In the US there are for example the Advanced Photon Source (APS) near Chicago and the Advanced Light Source (ALS) in Berkeley. Free electron lasers (FEL) are referred to as fourth generation.

Several different magnet configurations are used as radiation sources in a synchrotron. Bending or dipole magnets not only keep the electrons on track in a storage ring, but they produce radiation with a broad and continuous spectrum and high photon flux Φ, but the area ΔA of the source and the solid angle of emission $\Delta\Omega$ are also large. Certain experiments require a small phase space of the radiation $\Delta A \cdot \Delta\Omega$. Insertion devices like undulators and

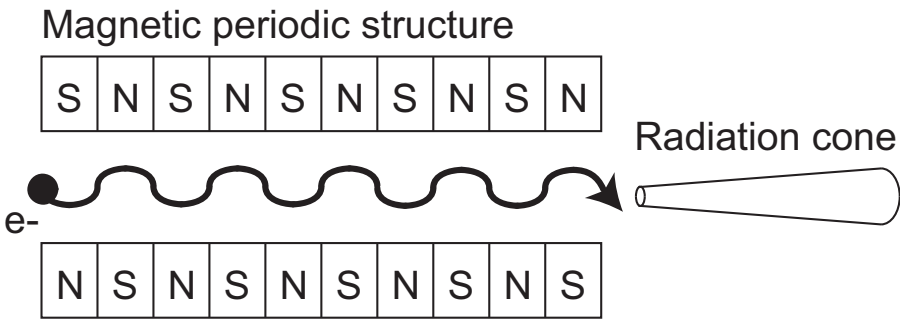

Figure 1.1: Schematic of an undulator. A periodically changing magnetic field makes the electrons go in sinuous lines and emit a narrow radiation cone in the forward direction.

wigglers have been designed to make x-rays with different properties available. An undulator is a periodic structure of permanent magnets assembled in a row with interchanging polarity (see Fig. 1.1). Electrons are passing through the oscillating magnetic field on a sinuous line, emitting photons in a forward beam cone with a small phase space. The photons have high temporal coherence and the emission spectrum of the undulator can be tuned by adjusting the strength of the sinusoidal magnetic field, which is accomplished by adjusting the mechanical gap between the top and bottom magnet structures of the undulator. Its small spectral bandwidth $\Delta E/E$ (in addition to small area and angular emittance) makes undulator radiation suitable for experiments with high brightness requirements. The spectral brightness B of an x-ray source is commonly defined as

$$B = \frac{\Phi}{\Delta A \cdot \Delta\Omega \cdot 0.1\% \Delta E/E} \,. \tag{1.1}$$

Fig. 1.2 shows a brightness comparison of a few x-ray sources. Plotted in red are the values for the X1 undulator at the NSLS, that was used for all experiments described in this thesis. The X1 undulator with 35 periods of 8 cm length can operate with a minimum gap of 32 mm [1] between the samarium cobalt permanent magnets.

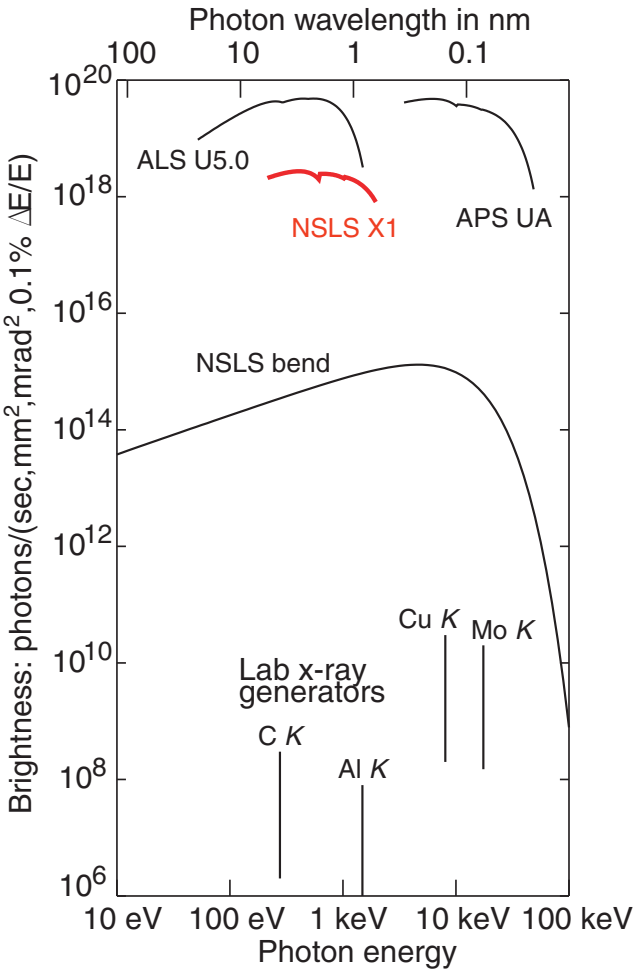

Figure 1.2: Brightness comparison of x-ray tubes and selected synchrotron sources. Highlighted in red is the source relevant for this work, the X1 undulator at the NSLS.

1.2 X-ray absorption spectroscopy

X-ray absorption spectroscopy (XAS) records the photon flux transmitted through a specimen relative to the incoming flux as it depends on the x-ray energy. The absorption spectra acquired are used to analyze the chemical nature of the sample. We generally have to distinguish between two types of XAS:

- **XANES spectroscopy:** X-ray absorption near-edge structure concentrates on the energy region around an element's absorption edge. It is characteristic for the bonding state of the element and can therefore be used to identify chemical phases within a sample.

- **EXAFS spectroscopy:** Extended x-ray absorption fine-structure on the other hand focuses on energies far away from an element's absorption edge. It can identify oscillations in the x-ray absorption caused by interference of ejected electrons and therefore determine distances between electron shells and between nuclei or "bond distances".

This thesis will deal with XANES spectra only. An incoming photon with an energy greater than or equal to the binding energy of an inner-shell electron can knock the electron into the so-called continuum leaving behind an ionized atom. In a spectrum depicting the absorption of photons (see Fig. 1.3 right) such a process would appear as a step-like increase (green line) defining an absorption edge. Another photon of a slightly smaller energy can also lift an electron from a lower to a higher orbital leaving the atom in an excited state (see Fig. 1.3 left). In the spectrum on the right side such a transition would appear as an absorption peak (orange line) in the vicinity of the absorption edge.

In molecules, a large number of electronic states exist with very low binding energies of a few eV corresponding to chemical bonds, as well as short-lived excited states above the classical binding energy. Excitation of inner-shell electrons into these states rather than to the vacuum leads to the presence of absorption resonances near the binding edge energy, with resonances at lower energies corresponding to longer-lived, bound states and resonances at higher energies matching shorter-lived, classically unbound states. These resonances are referred to as near-edge x-ray absorption fine-structure (NEXAFS) or x-

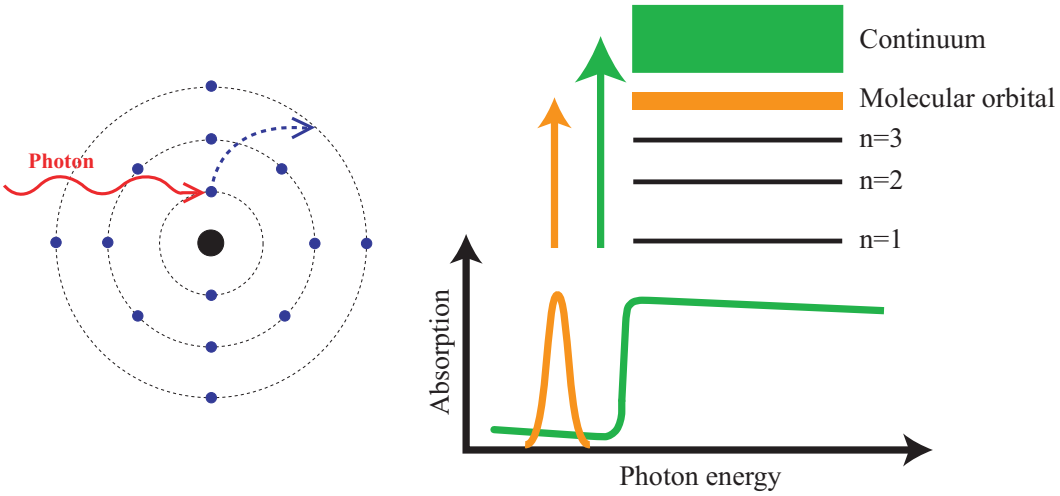

Figure 1.3: Schematic of an x-ray absorption near-edge structure (XANES) spectrum. An incoming photon (left) can lift an electron to a not fully occupied, higher orbital or remove it from the atom into the continuum. In the absorption spectrum (right) the ionization shows as a step function (green), while the excitation of electrons to orbitals just below the vacuum level show as overlaid absorption peaks (orange) close to the edge.

ray absorption near-edge structure (XANES).[1] So the bonding states of an element such as carbon can be determined by measuring within a very limited energy band. In our work we chose regions of about 5-20 eV below and above the edge.

1.3 Fresnel zone plates

The energy-dependent, complex index of refraction for x-rays is often defined as $n = 1 - \delta - i\beta$, where δ describes the phase shift in a material and β the absorption. In the x-ray regime δ is a small number, so that single refractive lenses do not have enough focusing power. While compound refractive lenses have been developed for hard x-rays [3], the high absorption of the lens material makes the use of refractive optics impossible for low energy x-rays. At the same time the extremely high requirements for surface roughness and ac-

[1] For extensive reading on this topic we recommend the book on NEXAFS spectroscopy by Stöhr [2].

curacy compromise the use of reflective mirror optics as high-resolution x-ray objectives. Most modern soft x-ray lenses are therefore based on diffraction.

Fresnel zone plates (ZP) are circular diffraction gratings used to produce a diffraction limited first[2] order focus. The width of individual zones is decreasing radially (see Fig. 1.4), so that rays with a path difference of one wavelength λ interfere constructively in the focal spot. The number of zones N on a zone plate depends on its diameter D and the width of the outermost zone $\mathrm{d}r_N$ as

$$N = \frac{D}{4\,\mathrm{d}r_N}\ . \tag{1.2}$$

Zone plates are chromatic lenses where the focal length f grows linearly with the photon energy:

$$f = \frac{D\ \mathrm{d}r_N}{\lambda} = \frac{D\ \mathrm{d}r_N}{hc}\ E \tag{1.3}$$

In imaging applications zone plates therefore need to be illuminated with monochromatic light. For best performance the monochromaticity should be higher than the number of zones:

$$\frac{\lambda}{\Delta\lambda} > N \tag{1.4}$$

Also the energy dependence of the focal length has to be taken into account when tuning the x-ray energy in zone plate based instruments (see Chap. 2).

The numerical aperture of a lens is defined as the sine of the half-opening angle θ. For a zone plate in small angle approximation this is

$$\mathrm{NA} = \sin\theta \approx \frac{\lambda}{2\,\mathrm{d}r_N}\ . \tag{1.5}$$

In imaging systems with uniform plane-wave illumination a zone plate can be treated as thin lens. The spot size of a circular lens is described by an Airy pattern [4], and the Rayleigh resolution criterion refers to the case where the first Airy minimum of the image of one point source lies on the center of the image of another point source, giving a resolution of

$$\delta_t = 0.610\,\frac{\lambda}{\mathrm{NA}} = 1.22\ \mathrm{d}r_N\ . \tag{1.6}$$

[2]The use of higher order foci is possible, but not considered in this work.

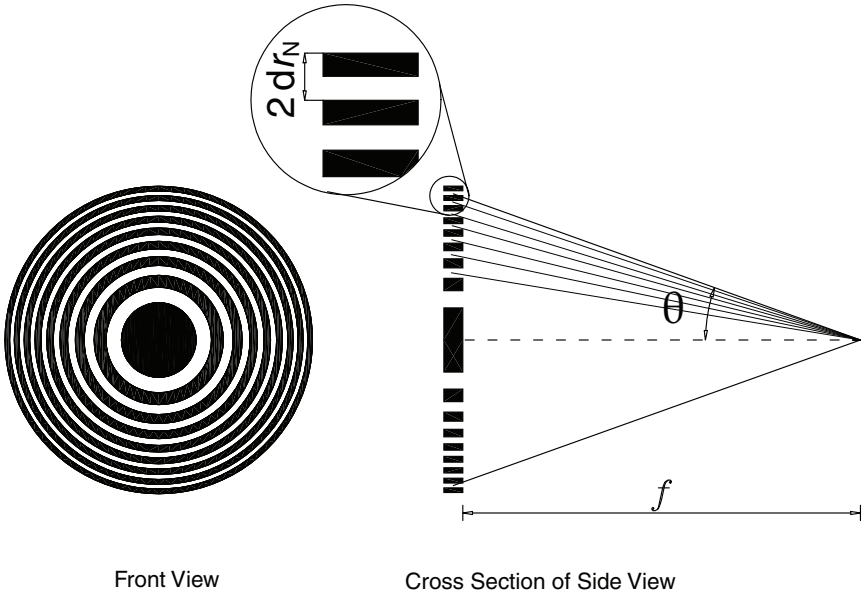

Figure 1.4: Schematic of a Fresnel zone plate. Concentric transparent and opaque zones alternate radially with decreasing width (left). The point where the path difference to neighboring transparent zones equals one wavelength λ is the first-order focus (right). Labeled are the outermost zone width $\mathrm{d}r_N$, the focal length f and the half-opening angle of the beam cone θ.

While the spatial resolution does not depend on the x-ray wavelength, the depth of focus, or longitudinal spot size, does:

$$\delta_l = 1.22\,\frac{\lambda}{(\mathrm{NA})^2} = 4.88\,\frac{(\mathrm{d}r_N)^2}{\lambda} \tag{1.7}$$

Zone plates typically employed in soft x-ray scanning microscopes (see Sec. 1.4) have diameters of 80 or 160 μm and outermost zone widths of 45 to 30 nm. The first order focus produced has a transverse spot size of about 35-55 nm and a depth of focus in the order of microns. Therefore, compared to electron microscopy rather thick samples and even whole cells can be imaged. The focal length is in the order of millimeters.

To block all diffraction orders other than the first, zone plates are fabricated with an opaque central stop of usually half their diameter. They are then used in a set with an order sorting aperture (OSA) - a pinhole of a little smaller diameter than the central stop - which is placed between zone plate and sample

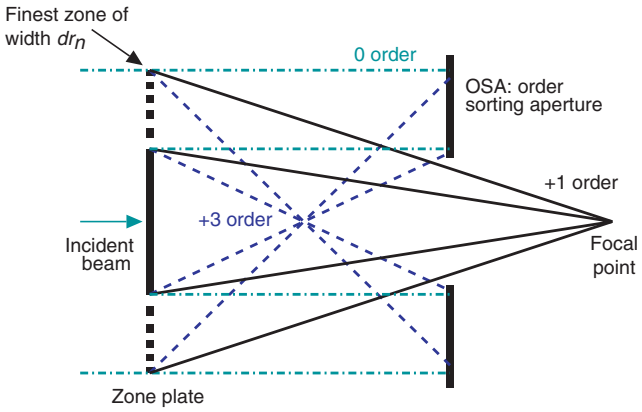

Figure 1.5: Working principle of the order sorting aperture. The pinhole of the OSA has to be a little smaller than the zone plates central stop. If aligned properly between zone plate and sample all diffraction orders except the positive first are blocked.

as illustrated in Fig. 1.5.

In traditional "amplitude" zone plates half the photon flux is absorbed in the opaque zones and ideally only π^{-2}, or about 10%, is diffracted into the first order focus. To improve the efficiency the zone materials with low absorption like nickel and gold can be used. Instead of absorbing the x-rays the zones then have to have the right thickness to introduce phase shift of π, again leading to constructive interference in the focal spot. Fabricating these "phase" zone plates [5] with thin zones of more than 100 nm thickness is a challenge and currently sets the resolution limit in zone plate based imaging systems.

1.4 X-ray microscopy

There are two ways to do microscopy by recording the x-ray flux transmitted through a sample. One is in a transmission x-ray microscope (TXM) and the other in a scanning transmission x-ray microscope (STXM). Schematics of both instruments are given in Fig. 1.6.

The TXM was pioneered by G. Schmahl et al. from the University of Göttingen in Germany. An entire sample area is illuminated by a large condenser zone plate and magnified with a high resolution objective zone plate onto an area-resolving detector like a CCD camera. Since the phase space and coherence

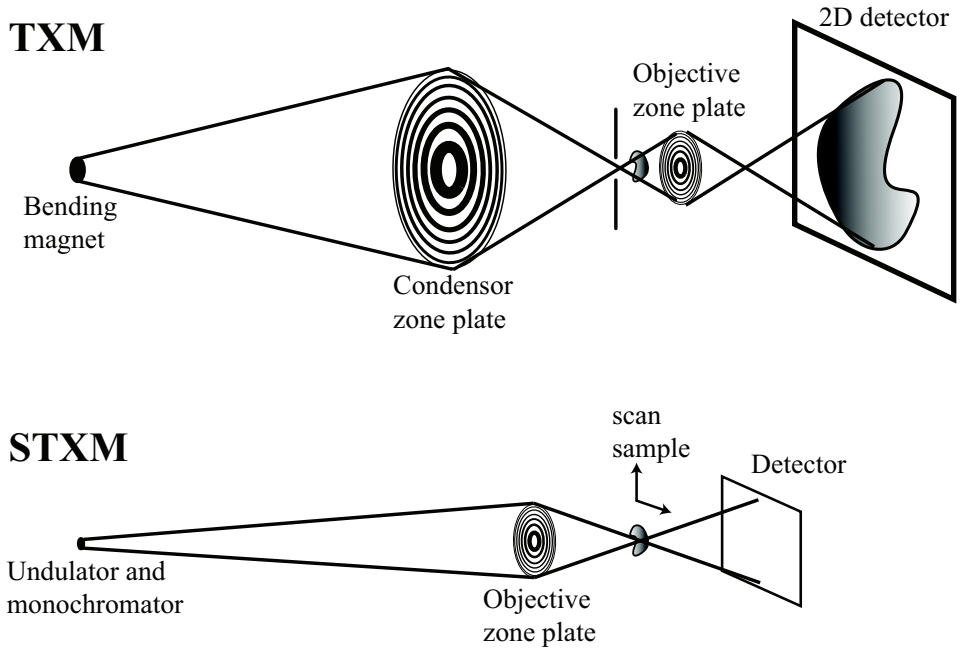

Figure 1.6: Schematic of the image formation in a transmission and a scanning transmission x-ray microscope

requirements of a TXM are much more relaxed than in STXM, a TXM can be used efficiently with a bending magnet source. In a TXM large images can be acquired within seconds making them well suited for 3D tomography, but the second zone plate before the detector makes a sufficiently high x-ray flux through the sample necessary, so that it experiences a great exposure. This can be a problem in particular for radiation-soft specimens. Also the energy resolution $E/\Delta E$ of TXM beamlines has been moderate in the past, making them less suitable for doing spectroscopy. Phase contrast imaging can be realized using the Zernike method [6], just as in visible light microscopy.

In STXM a sample is raster scanned through a focused x-ray spot and the transmitted signal is detected pixel by pixel by a large area detector. After the usefullness of such a system had been demonstrated with synchrotron radiation using a pinhole to collimate the beam [7], it was J. Kirz et al. from Stony Brook University who took on the development of STXM using high resolution zone plates as objective lenses. Because of the high brightness and coherence requirements in STXM, an undulator source is needed for best results. The acquisition of a single image, depending on the image resolution and pixel dwell time chosen, takes on the order of minutes. STXM beamlines can use high energy-resolution grating monochromators ($E/\Delta E \approx 3000...5000$), rendering

them well capable for spectroscopy. Microscopy and spectroscopy capabilities combined (called "spectromicroscopy") make for a powerful tool to investigate the chemical nature of a large variety of specimens. It is possible to either take point spectra of specifically chosen sample spots, or acquire so-called spectromicroscopic "stacks". A scan of an extended sample region is repeated over a whole series of photon energies - typically around an absorption edge of a chemical element of interest - providing the user with XANES spectra of each individual image pixel, used for chemical mapping.

Since the scanning in STXM leaves no phase relationship between individual pixels phase contrast can only be measured differentially. A 2D detector can be used to map out shifts in the transmitted beam cone introduced by phase gradients in a sample [8, 9]. There are STXM systems available at the ALS in Berkeley [10] and at BESSY II in Berlin [11]. A copy of the ALS STXM has been in operation at the Swiss Light Source since 2007. In the follwing chapter we will describe recent updates of the NSLS X1A STXM.

Chapter 2

The 5th Generation Scanning Transmission X-ray Microscope

2.1 STXM at the NSLS

The history of STXM at the NSLS goes back to the early 1980's at beamline U15 where Janos Kirz, Harvey Rarback and John Kenny of Stony Brook University built the first system using a Fresnel zone plate as focusing optics and achieved a measured resolution of 0.3 μm [12]. This instrument run between 1982 and 1986 is referred to retrospectively as STXM 1.

In 1987 a new STXM 2 was operated briefly at beamline X17T with a prototype undulator of only 10 periods until it was finally moved by Chris Buckley et al. [13] to the dedicated microscopy beamline X1A. The microscope used a two axes laser interferometer with the moderate resolution of 31.6 nm as feedback system for a plain piezo stage [14].

Since Chris Jacobsen in Stony Brook took over the main effort in the technical development of STXM, three more generations have been operated with the same undulator source until today. From 1992 on the improved spatial resolution of STXM 3 - using a Queensgate piezo system with capacitance micrometer feedback - made it possible to reslove 36 nm features in a gold test object [15].

The first version of beamline X1A (1990-1997) already had two branches that were both serviced by the same grating monochromator. Being at different angles from the grating, they could be run at different wavelengths simultaneously, but not be tuned independently. At the end of the last century beamline X1A was then rebuilt to serve two identical STXMs simultaneously with individual monochromators [1]. One branch (X1A1) is optimized for energies around the carbon K-absorption edge at 284.2 eV, while the other (X1A2) is dedicated to nitrogen energies around 409.9 eV and oxygen energies around 543.1 eV.

From 1999 on the STXM 4 endstations on both branches were the first fully motorized system with computer controlled scanning of the sample as well as the detector platform [16]. They also introduced an entirely new mounting system for the samples, again relying on capacitance micrometer feedback integrated in a 2D piezo stage[3] for high resolution scans.

STXM 5, the recent generation operating since 2005, is a retrofit of the existing microscope with a three axes differential laser interferometer system for improved sample positioning and faster scan and data acquisition electronics. Before we describe this upgrade in detail, we want to give the reader an

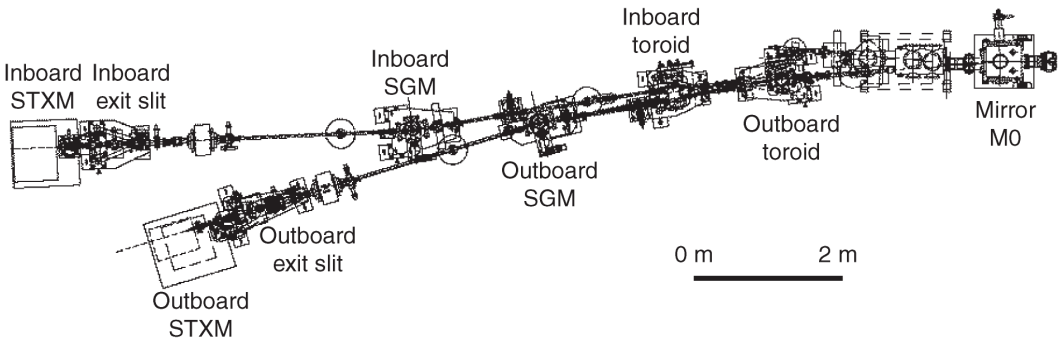

Figure 2.1: Layout of beamline X1A [adapted from [1]]. Beam from the X1 undulator is divided twice to simultaneously serve three beamlines. Mirror M0 does the first split between X1A and X1B (not shown) lines, while outboard's toroidal mirror further downstream divides the remaining beam to service outboard and inboard branch.

overview of beamline X1A and STXM 4.

2.1.1 Beamline X1A

The soft x-ray microscopy beamline X1A offers x-rays between 250 and 800 eV including the so-called water window between the carbon and oxygen K-edges. This region is of particular interest for biological (and other) applications, since specimens in their natural hydrated environment can be analyzed for their carbon chemistry. The x-ray beam from the X1 undulator services three beamlines, that can be run in parallel. The spectroscopy beamline X1B receives about 65% of the beam, while scraping mirror M0 [17] reflects the rest to the X1A branches (see Fig. 2.1). Further downstream outboard's toroidal mirror reflects half of the remaining beam to the "outboard" branch (X1A1) and the other half services the "inboard" branch (X1A2).

The general arrangement of optical components is the same in both X1A branches and shown schematically in Fig. 2.2. The toroidal mirror has two different radii of curvature in the horizontal and the vertical. In the horizontal plane it focuses beam onto an entrance slit (ENS) collimating the beam before the spherical grating monochromator (SGM). The SGM disperses the x-ray beam in the horizontal and at the same time refocuses the entrance slit on an exit slit (EXS). The exit slit picks a small bandwidth out of "rainbow of colors" in the positive first diffraction order from the grating. The SGM

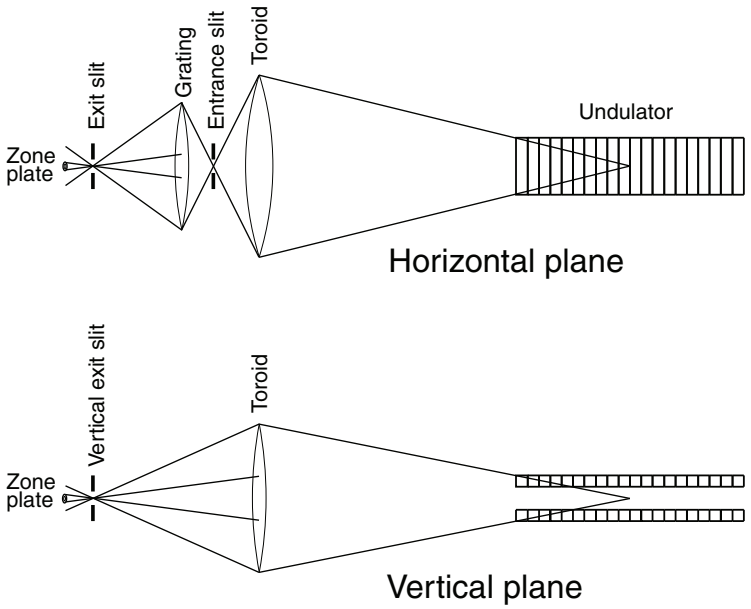

Figure 2.2: Schematic views of the optics in beamline X1A [adapted from [1]].

is rotated via a lever arm (linear in wavelength) in order to select a certain x-ray energy. While the energy range of photons reaching the zone plate gets smaller with the width of ENS and EXS chosen, the same is obviously true for the photon flux. In the vertical plane the toroid merely focuses the source onto a vertical exit slit (EXSY). The exit slits define the source size for the STXM experiment, providing the spatial coherence needed for the zone plate lens. Not shown in the schematic is a set of two parallel order sorting mirrors (OSM). Depending on their material (quartz or nickel) and the angle of grazing incidence the superpolished mirrors absorb higher energy photons from higher diffraction orders of the grating.

The SGM position as well as all slits are adjusted by computer controlled stepper motors. For the acquisition of point spectra the SGM can be made to move at constant speed between starting and ending energies.

2.1.2 STXM 4

This section describes the STXM 4 microscope as far as it is necessary to understand the upgrade steps to the 5^{th} generation that we have undertaken. For an extensive description of all microscope components see the Ph.D. thesis

by Michael Feser [18].

The 3D coordinate system in the microscope is defined to follow the right-hand rule with the positive Z direction coinciding with the downstream x-ray beam direction. Y is defined as being positive upwards and the X direction is therefore horizontal (being positive towards the outbard direction). The X/Y plane is therefore the image plane of a regular sample scan and the focal length of the zone plate changes in the Z direction.

Fig. 2.3 shows AutoCAD renderings of the vacuum chamber containing the main microscope components. The x-rays enter the chamber through a 100 nm thick and 250 μm squared silicon nitride membrane ("exit window") at the end of a small evacuated pipe called "exit snout". The zone plate and OSA, which come after, are each mounted on glass cones protruding from right angle brackets on four-axes tilt aligners.[1] The aligners allow to manually adjust the position as well as the tilt of zone plate and OSA with respect to the x-ray beam. In addition the OSA assembly sits on a stepping motor,[2] that allows to adjust its Z position during energy changes. The zone plate is connected to the sample over a U-shaped arm (see Fig. 2.4). The sample itself sits on a custom made mounting plate in a receptacle, that screws onto a two axes (X and Y) piezo-actuated scanning stage.[3] Under this is positioned a stack of three (X, Y and Z) stepping motor stages[2] sitting on an invar plate on the microscope bottom. The combination of piezo and stepper motors is needed to provide both high resolution positioning and large travel ranges. So coarse overview scans of large areas are possible as well as high resolution images of small sample regions.

Downstream of the sample stage follows the detector platform with slots for three different detectors. One slot carries a visible light microscope used for prefocusing and preselection of interesting sample regions, while the others are occupied by either a proportional counter, a charge integrating detector with segmented silicon chip, or whatever detectors users need for their experiments. The detector platform sits on a stack of three (X, Y and Z) stepping motors.[2] Tab. 2.1 lists all motor devices in STXM 4 along with their encoder resolutions and travel ranges. While the stepper motors all have optical encoders for positioning feedback, the piezo stage relies on capacitance micrometers. The high resolution of the Z sample stepper is needed to keep the sample in the

[1] New Focus model 9071

[2] by Newport Corp.

[3] by Physik Instrumente (PI) GmbH & Co.

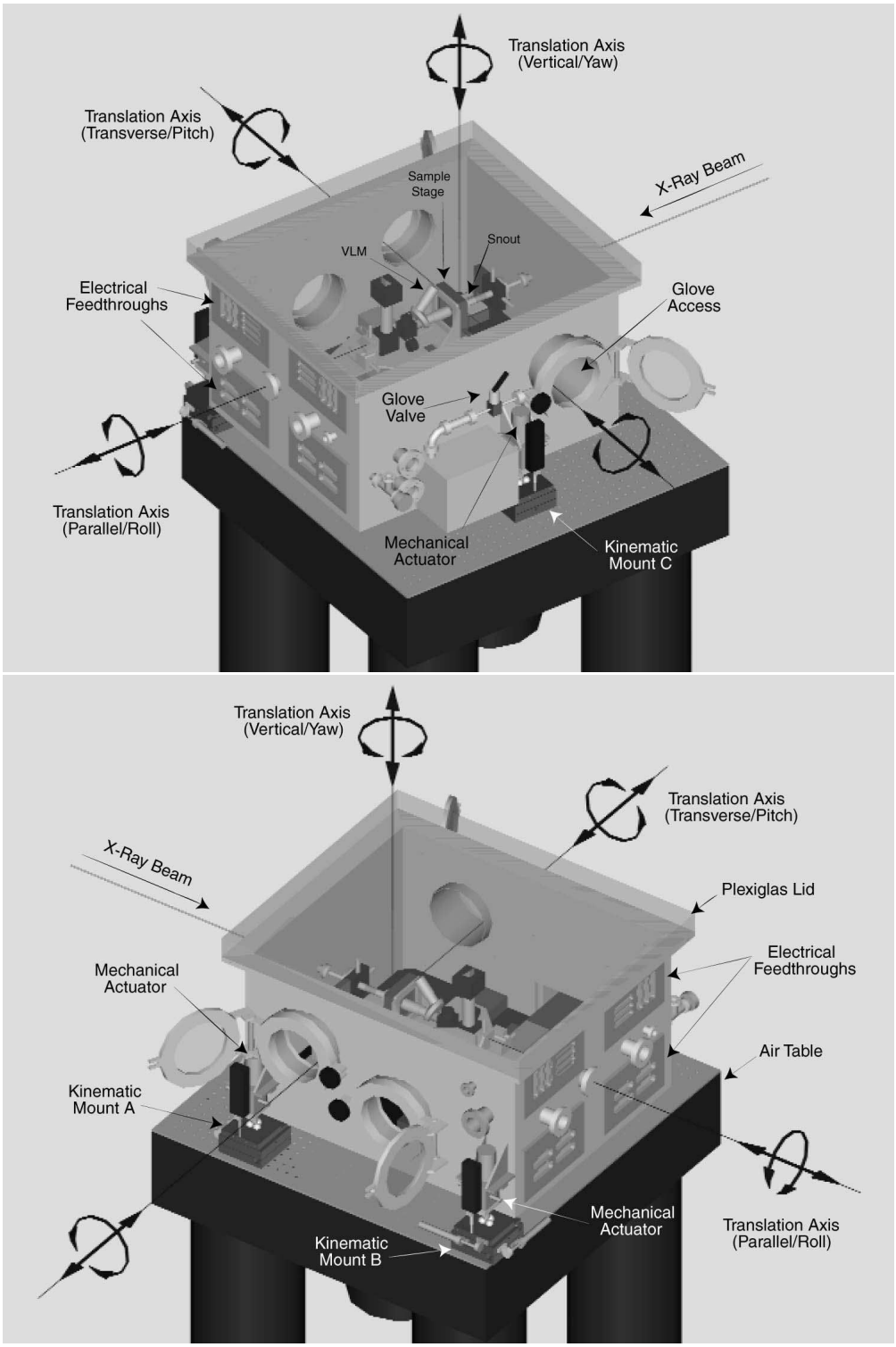

Figure 2.3: The STXM 4 microscope chamber [reprinted from [19]].

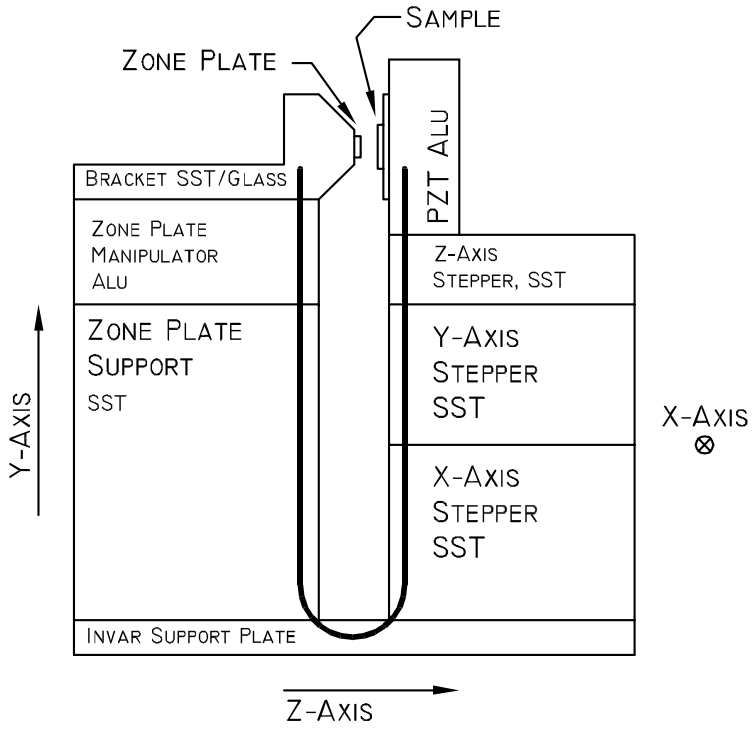

Figure 2.4: Schematic of zone plate and sample assembly [reprinted from [18]]. Zone plate and sample are connected over a U-shaped arm. An Invar plate at the bottom and matched materials (stainless steel and aluminum) under zone plate and sample help minimize relative thermal drifts between the two.

focus position. The travel ranges of the X sample and the X detector stages are particularly large to allow for the entire sample stage to be moved out of the x-ray beam and for each individual detector to be put onto the x-ray beam axis.

To isolate the microscope from vibrations on the experimental floor it sits on an optical air table. The chamber is supported by a tripod of kinematic mounts, so that the entire microscope can be aligned by moving and rotating it with respect to the x-ray beam.

The absorption of soft x-rays in air is about 10 to 100 times higher (depending on the photon energy) than in a helium atmosphere. Therefore to reduce the absorption of x-rays between exit window and detector the microscope chamber can be pumped out and backfilled with helium gas. As an alternative to the pump down helium can be constantly blown into the beam path. However, removing the air from the chamber is mandatory on the inboard microscope,

Name	Stage	Motor	Enc. Res. [μm]	Range [mm]
XPZT	P-731.20		0.005 (repeatable)	0.100
YPZT	P-731.20		0.005 (repeatable)	0.100
XSTG	UTM100PE1	UE31PE	1.0	100
YSTG	UZM80PP.1	UE41PP	0.10	4
ZSTG	MFN25PP	UE16PP	0.074004	25
XDET	MTM250PP1HL	UE63PP	1.0	250
YDET	UZM80PP.1	UE41PP	0.10	4
ZDET	UTM50PP1HL	UE41PP	1.0	50
ZOSA	MFN08PP	UE16PP	0.074004	8

Table 2.1: STXM 4 devices. Devices with ending PZT are two axes of a sample piezo stage.[3] Devices with ending STG are sample stepper stages,[2] with DET detector stepper stages[2] and OSA is the stepper[2] for the order sorting aperture. Encoder resolutions and travel ranges are as given by the manufactureres.

when the nitrogen or oxygen chemistry of a sample are of interest. To make the chamber vacuum compatible it provides a variety of vaccum feedthroughs for electronic connections on the downstream wall. Most control and data acquisition electronics sit in a rack next to the microscope along with a computer running control software and graphical user interface (GUI).

2.2 Motivation for the upgrade

The 4$^{\text{th}}$ generation STXM for sample positioning relied exclusively on the encoder feedback of the stepping motors and capacitance micrometer feedback of the piezo stage. There are potential problems in this method. For once the motor motion itself is not perfectly accurate. Especially the motion of the Z stepper motor used for refocusing at energy changes is critical. Its slight wiggling results in transverse and angular shifts of the sample that make it impossible to reproduce image fields with high precision. On the other hand over the rather long acquisition time (in the order of several hours) of spectromicroscopic stacks other kinds of drifts may occur. This refers mostly to changes in the mechanical path distance between zone plate setup and sample mount due to temperature fluctuations, but also vibrations introduced by the environment. The thermal drifts are on a small but noticeable scale compared to the imaging resolution. Mostly they are a problem, if the sample running out of focus in the Z direction, while drifts in the X and Y directions

can be compensated for by choosing slightly larger image fields, but leading to increasing acquisition times. These problems can be addressed by a laser interferometer system to measure and correct the relative positions of zone plate and sample.

The first effort to employ a two axis (X/Y) laser interferometer in STXM was done in the 1980's at the NSLS mini-undulator beamline X17T [14]. But its moderate resolution of 31.6 nm was not enough to keep up with modern zone plate development and it was subsequently replaced by an analog feedback system with capacitance micrometers. Another two axis system with 2.5 nm resolution was implemented later on at the ALS [10]. It improved the reproducibility of the field of view to the degree needed for permanent operations in a state of the art scanning x-ray microscope. In addition to this we decided to install a third laser interferometer for the Z axis as well to improve perpetuation of focus positions. The three axes laser interferometer system defines a relative coordinate system between focusing optics and sample independent of drifts in the mechanical setup (Sec. 2.3).

The biggest source of drifts in the image fields however has always been the relative misalignment of the microscope Z axis towards the x-ray beam axis. Mechanical improvement of the alignment is possible, but time consuming and cumbersome. We now employ a software controlled way of correcting for the misalignment in stacks (Sec. 2.6.3).

In the same retrofit the electronics and data acquisition system was upgraded. In the old system the voltages driving piezo motion were controlled via an external IOtech digital to analog converter. The detector data were acquired in IOtech scalars and analog to digital converters and transferred scan line by scan line into computer memory over a slow IEEE-488 interface, also known as General Purpose Interface Bus (GPIB). During the data read out the x-ray beam was dwelling at the beginning of each scan line causing an excess of radiation damage on one side of the scan area. The new system is able to acquire whole scans in a continuous and time saving fashion, also reducing the radiation damage on the sample (Sec. 2.4.2).

The new system combines all positioning and data acquisition boards (Sec. 2.5) in a single computer box running Microsoft Windows 2000. A C++ microscope server is running on the same machine. The user can communicate remotely with the microscope server over TCP/IP sockets from anywhere there is internet access (Sec. 2.6.1). This is mainly done via a dedicated graphical user interface (GUI) written in the Interactive Data Language (IDL). Besides gen-

eral microscope control the GUI offers advanced features like image processing and statistics. It is also available without microscope control features for data inspection.

The entire upgrade was a joined effort of students in the x-ray microscopy group under the direction of Chris Jacobsen. Part of Mirna Lerotić's Ph.D. thesis work [20] was dedicated to testing and operations of the laser interferometer system. She was also responsible for the interfacing and programming of the controller for the interferometer motors and related C++ classes. Daniel Flickinger did the mechanical assembly of the laser and interferometer system as minor project towards his degree of Master of Scientific Instrumentation. Benjamin Hornberger, on the side of his Ph.D. work on differential phase contrast microscopy [21], wrote the major parts of the excellent graphical user interface. The hardware and programming of the new data acquisition and position streaming electronics as well as the new scan concept and improvements to the overall microscope control was my responsibility. I also worked out the networking code with remote and automatic control of the microscopes, programmed and implemented a new controller for the stepper motors and added a filter for statistical noise to the GUI. Thanks to Michael Feser for his contributions in the start-up of the whole project.

2.3 Mechanical layout of the interferometer hardware

At the time STXM 4 had been to designed to contain the necessary microscope components with little extra space. So it was a challenge to fit all parts for the interferometer upgrade and the mounting structures into the existing chamber.[4] The helium-neon laser head[5] (with two orthogonally polarized frequencies close to 633 nm and 1 mW maximum beam power) is mounted at the outside can of the microscope and the laser beam is fed into the chamber trough a standard glass viewport. The assembly inside the chamber is shown in Fig. 2.5. Rendered in grey are custom made aluminum towers designed to hold all optical components in place. Shown in brown are beam splitters, benders and differential interferometer heads. The yellow parts are three mirrors (X, Y and Z) on the sample receptacle. (For overview purposes the zone

[4] work by Daniel Flickinger

[5] Agilent Technologies model 5517C

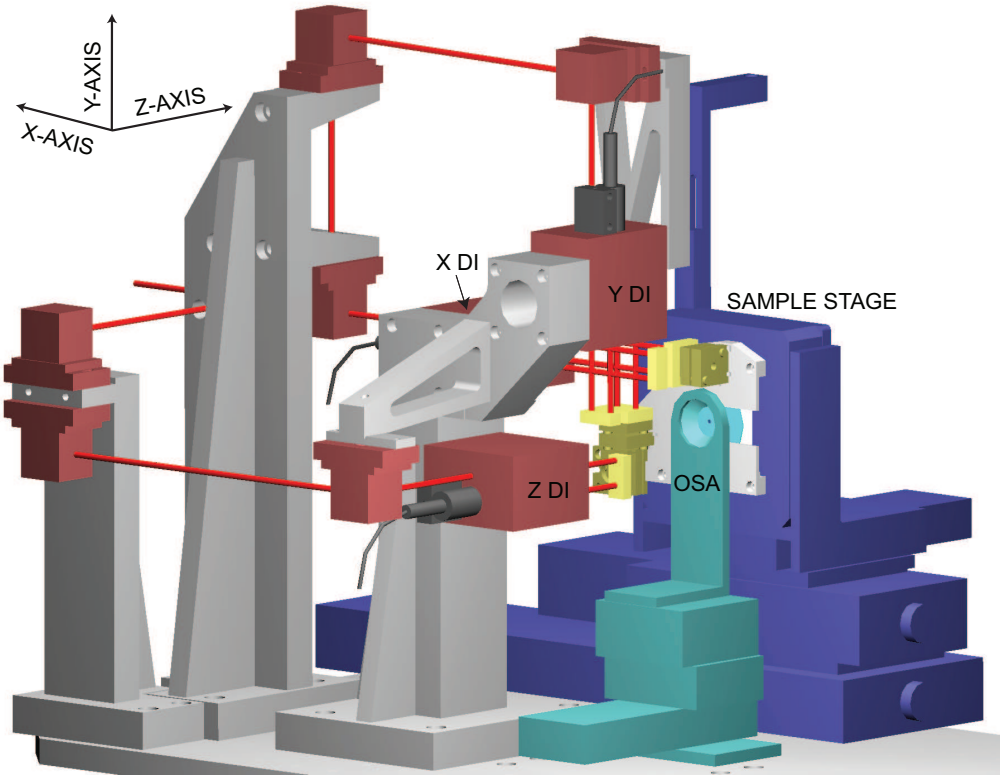

Figure 2.5: Rendering of the STXM 5 interferometer setup.[4] Shown in brown are the commercial beam splitters that divide the laser beam into equal parts, the beam benders for directing the beams and the three differential interferometer (DI) heads. The grey parts they sit on is the support system, custom made to fit into the existing microscopes. The laser beams (red) reflect off the three sample measurement mirrors (yellow). Not shown is the zone plate setup with its three reference mirrors.

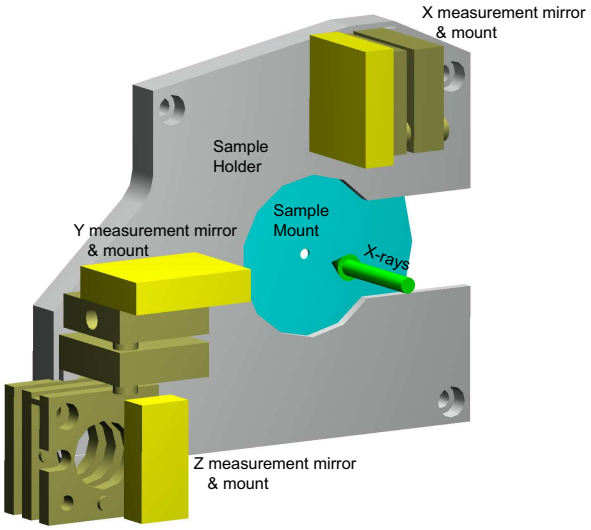

Figure 2.6: Rendering of the STXM 5 sample mount.[4] The surfaces planes of the X and Y measurement mirrors (yellow) were chosen to lie on the sample position, in order reduce distortion effects. For mechanical reasons, this was not possible for the Z mirror (yellow). The sample grid sits in the center (white whole) of the sample mount (blue), which is held in place by magnets in the sample

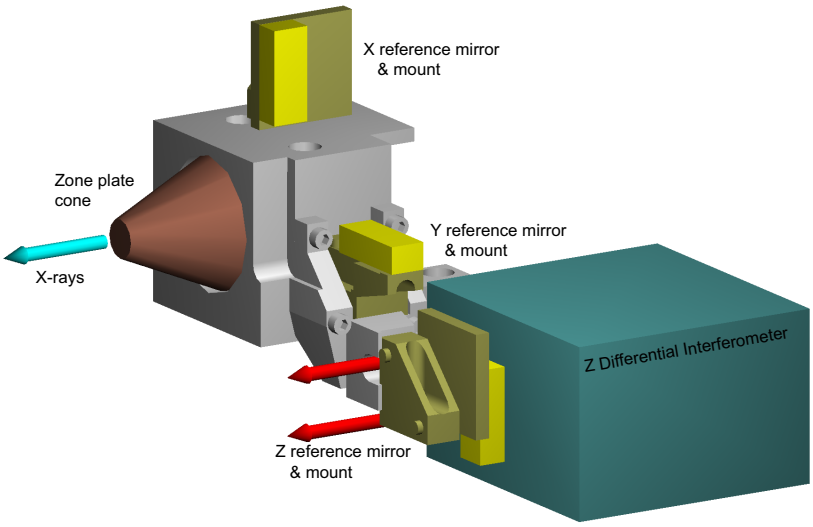

Figure 2.7: Rendering of the STXM 5 zone plate assembly.[4] The glass cone (brown) holding the zone plate sits on a aluminum block (grey) with enough room to hold all three reference mirrors (yellow). Shown for the Z axis are the differential interferometer head (turquoise) and the two laser beams (red) directed towards the Z measurement mirror on the sample holder.

plate holding structure is not shown.) After the laser beam (red) enters the chamber it is divided by two beam splitters (33/66 and 50/50) into three equal parts, each of which is directed by beam benders towards a plane mirror type differential interferometer head.[6] Each interferometer head produces a total of 4 beams. One laser frequency is then sent to be reflected off a reference mirror (on the zone plate assembly) and the other to a measurement mirror (on the sample receptacle). For higher precision the laser beam is made to bounce twice off of each mirror. The two beams are then rejoined and the interference signals are transmitted via fiber optics cables through a vacuum feedthrough in the chamber wall. Receivers[7] outside of the chamber convert the signals from optical to electronic, which are then fed into a PCI board[8] on the microscope control computer.

Sample holder (see Fig. 2.6) and zone plate mount (see Fig. 2.7) each carry three plane reflecting mirrors (shown in yellow), one for each euclidean microscope axis. The mirrors are made of a borosilicate glass substrate (for low expansion) with a protected silver coating. At 633 nm wavelength the reflectivity of the mirrors is given as 96% and their surface flatness as $\lambda/20$ by the manufacturer[9]. The mirrors are glued to flexure stages for manual alignment perpendicular to the laser beam.

For unknown reasons after a while of operations in the inboard microscope the silver coating deteriorated. It was etched away starting from the mirror edges, where the protective coating is the weakest. The problem was addressed by recoating inboard's mirrors with gold, which is less reactive than silver. The reflectivity of gold at 633 nm is still 92% and could be enhanced to 94% with a special dielectric coating. The silver mirrors in the outboard microscope have shown no degradation until today.

2.4 Working principle

The laser interferometer system along with a new motor controller made a new concept for high resolution scans possible. The working principle of both will

[6] Agilent Technologies model 10719A

[7] Agilent Technologies model 10780F

[8] Agilent Technologies model N1231A

[9] Reynard Corp., San Clemente, CA, USA

be explained in this section.

2.4.1 Laser interferometer feedback

The hardware of the interferometer system has already been described in Sec. 2.3. But how does the new system actually work?

The two frequencies present in the laser beam are separated by the differential interferometer according to their orthogonal polarizations (see Fig. 2.8) and then one is directed to the reference the other to the measurement mirror. To double the sensitivity to changes in the relative mirror position each beam is reflected twice. If one of the mirrors is moving, the reflected beam gets Doppler-shifted ($\pm 2\Delta f$) to a slightly different frequency. Both parts are then recombined and sent to the receiver. The beat from the interference of the two frequencies is used as measurement frequency to determine relative motion between the two mirror surfaces. The resolution of the positioning information is given as $\lambda/2048 = 632.991354\,\mathrm{nm}/2048 \approx 0.309\,\mathrm{nm}$ for each of the three interferometer axes (X, Y and Z). The receiver then converts the light signal into an electronic signal, which is fed into a computer board.[8]

This board calculates digital position information from the laser signal input and provides them on three 24 bit parallel outputs that are fed into accessory boards[10] of a programmable multi-axis controller[11] (PMAC) that controls three high resolution sample motors: X and Y sample piezo and Z sample stepper. The other microscope stepper motors are still controlled by a Newport controller. Tab. 2.2 shows in detail how each motor is controlled and what feeback system it uses.

The PMAC accessory boards have two 24 bit inputs, one for the actual position of the sample and another for the desired position. These desired positions are provided by another computer board, as we will see in Sec. 2.5. The PMAC is trying to match actual and desired positions by moving a motor accordingly. So the sample is moved if either its desired position is updated or its actual position relative to the zone plate changes (due to thermal drifts for example). By streaming desired positions to the PMAC in a constant flow one can set the sample into continuous motion following a chosen trajectory as we do in

[10] Delta Tau model ACC-14D

[11] Delta Tau model PMAC2-PCI

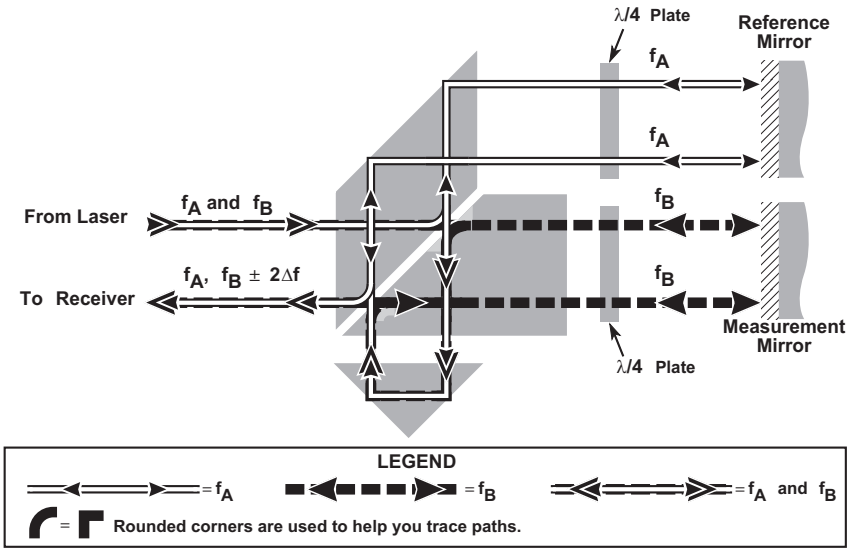

Figure 2.8: Working principle of the Agilent 10719A differential interferometer head. The two frequencies (f_A and f_B) in the laser beam are separated by their orthogonal polarization. One part reflects off the measurement mirror and the other off the reference mirror. $\lambda/4$ plates between mirrors and interferometer rotate the polarization direction of the beams and thereby direct the beams to follow the paths shown. Each beam is reflected twice by the same mirror to double the sensitivity to changes in the mirror position. The recombined beam is then sent to the receiver.

scanning. For simple moves to a new position the controller can also receive a command directly from the computer. The way the controller responds to position changes can be influenced by tuning the feedback loop via adjustments to proportional, integral and derivative (PID) gain parameters. More details about the Agilent laser interferometer system and the Delta Tau PMAC can be found in the Ph.D. thesis by Mirna Lerotić [20].

2.4.2 Scan concept

In principle all microscope devices can be scanned versus each other, with the exception that Z axis devices can only be the slow scanning device. In addition the beamline stepper motor controlling the SGM position is used to tune the x-ray energy and can even be used in spectral fly scans - so called "point spectra" of a specific sample spot. To uphold optimal focus conditions at energy changes, ZOSA and ZSTG are moved accordingly. Theoretically

Name	Controller	Feeback system
XPZT	Delta Tau PMAC2	Agilent interferometer (or cap. micrometer)
YPZT	Delta Tau PMAC2	Agilent interferometer (or cap. micrometer)
XSTG	Newport MM-3000 or XPS	Optical encoder
YSTG	Newport MM-3000 or XPS	Optical encoder
ZSTG	Delta Tau PMAC2	Agilent interferometer (or optical encoder)
XDET	Newport MM-3000 or XPS	Optical encoder
YDET	Newport MM-3000 or XPS	Optical encoder
ZDET	Newport MM-3000 or XPS	Optical encoder
ZOSA	Newport MM-3000 or XPS	Optical encoder

Table 2.2: Control of STXM 5 devices. For devices controlled by the Delta Tau PMAC2 the feedback is usually provided by the Agilent interferometer, but can also be chosen to be provided by the traditional system.

data sets with many dimensions could be acquired, but in practice scanning is restricted to 1D and 2D. Spectromicroscopic stacks, which are 3D data sets, are acquired as a series of 2D images at different x-ray energies that are saved as separate files. In the subsequent analysis the images can be merged into a data cube after an automatic alignment using Fourier cross correlations [22].

Tab. 2.3 lists the scan types that are employed in standard operation. Custom scans with freely chosen scan devices are possible in addition, but only used for diagnostics.

2D scans naturally have a fast axis on which there is constant motion and a slow axis that is only advanced at the end of a fast scan line. Scans with a stepper motor as fast device are controlled by the computer in a line by line fashion with the acquired data of a scan line being transferred into the main memory after each line. In STXM 4 this was true for all scan types and since the scanning and data acquisition electronics were not the fastest, there was a delay between each scan line. During this time the x-ray beam would sit a the beginning of a scanline as create an excess of radiation damage. In stacks, where images of the same sample region are acquired many times, the damage on one side of the scan could become severe (see Fig. 2.9).

The new positioning and data acquisition electronics (see Sec. 2.5) in STXM 5 allowed to improve the scan concept in two ways:

Scan type	Fast device	Slow device	Purpose
Piezo	XPZT or YPZT	YPZT or XPZT	High resolution images
Stepper	Any stepper	Any other stepper	Large field images
Focus	XPZT or YPZT	ZSTG	Finding x-ray focus
Spectrum	SGM and ZSTG	N/A	Spectrum of individual sample spot
Contrast	XPZT or YPZT	SGM, ZSTG and ZOSA	Finding photon energy with best contrast

Table 2.3: Scan types. When the SGM is scanned, ZSTG is usually moved simultaneously to keep the sample in x-ray focus.

1. It is possible to check on data and transfer them into main memory as they are acquired. (Also the communication with the data acquisition board is done over a PCI bus, which is much faster than the GPIB interface that was used previously.)

2. Desired positions for motors controlled by the PMAC can be streamed to the controller simultaneously in real time. So before a scan involving two motors with interferometer feedback starts, we set up a buffer of all motor positions in the scan and can then acquire the whole scan in a single shot.[12]

So while stepper scans in STXM 5 are still acquired line by line, it is now possible to grab the data of one scan line while data for the next line is already acquired, reducing wait times. Bigger were the improvements however for high resolution piezo scans, that are entirely controlled by the new PMAC. Besides the high resolution laser interferometer feedback, they can be acquired as a whole with collected data being transferred at leisure into main memory and displayed to the user. This increased the overall scan speed and reduced the radiation damage at the beginning of scan lines (see Fig. 2.9).

For stepper motors a fast scan line is done by sending the motor to move from starting to ending position at the speed chosen by the user as pixel dwell time. At the end of a scan line the carriage is made to fly back to the starting

[12]This is technically possible for all three axes at the same time but since we restrict ourselves to 2D scans it was chosen to arrange streaming inputs to only two of the PMAC accessory boards.

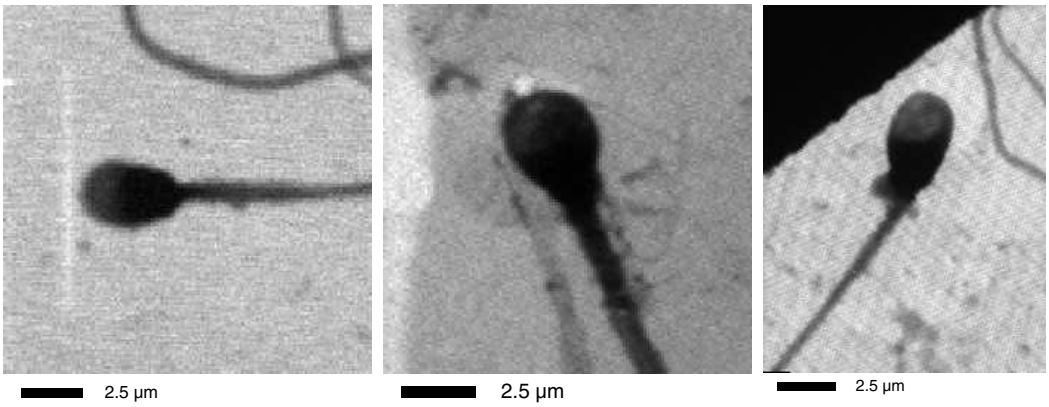

Figure 2.9: Comparison of radiation damage in STXM 4 and 5. An overview scan in STXM 4 (left) shows the damage at the beginning of each scan line after a single image. The damage is much higher after a spectromicroscopic stack of a sample region (middle). Due to the new scan concept in STXM 5 (right) a stack with similar overall exposure creates no comparable damage on the left edge.

point at maximum speed. We add a few pixels extra distance before the start and after the end points to allow for some ac- and deceleration respectively. The data from these extra regions are discarded. The step pulses driving the motors are used to trigger the data acquisition. Since stepper motors do not move very constantly, a clock signal[13] is recorded alongside the detected x-ray signal. The clock signal is later used to normalize the x-ray flux.

For scans with interferometer motors we set up a buffer of actual motor positions throughout the scan. This position profile for the fast axis is calculated according to start and ending position and scan speed as for steppers. But unlike for stepper motors where acceleration and flyback speed are given by the stage hardware, these parameters had to be chosen by us. Different scenarios were tested and eventually the best parameter values hard coded into the control software. To allow the stages to settle down after the flyback we also introduced a short waiting time, which however is nowhere near the time need for data read out in the old system. The slow axis positions in the buffer are linearly increased at the end of each scan line. Since the position streaming is very precisely timed, a clock signal does not need to be recorded. The data acquisition is timed by a trigger pulse from the streaming board. Details about the electronics behind this are given in Sec. 2.5.

[13] constant TTL signal of usually 100 kHz

2.5 Electronics

The new electronics system involves scanning and motor control on the one hand and data acquisition on the other hand. The routing of the electronic connections is done via a custom made connection interface board (see Sec. 2.5.1). Most boards sit in a sufficiently large rack mount Windows PC running a custom written server program (see Sec. 2.6). Along with most other electronic devices the same rack also holds a Linux PC with the graphical user interface.

Fig. 2.10 shows a schematic of the electronic devices involved in microscope operations. The stepper motor controllers[14] receive commands via GPIB.[15] New are the electronics for the three interferometer controlled axes. A PCI board[8] receives laser signals, converts them to position information and passes them on to a PCI digital servo controller[11] with three accessory ISA boards,[10] one for each interferometer controlled axis. Two external boards then are directed to control X and Y piezo motors[16] as well as the Z stepper motor.[17] The servo controller compares the laser interferometer with the currently desired positions and actively tries to match the two. This happens in a servo loop with a duty cycle of 442 μs. In scanning mode the positions are not provided via the PCI bus, but are streamed to the controller in real time. The streaming is done by a 32 bit digital PCI board[18] providing 16 bit precision for up to two possible scan axes. The assignment of scan axes to the PMAC accessory boards can be changed on the software side depending the current scan type. 16 bit of streamed positions at 0.309 nm resolution allow for step sizes of up to $\pm$10.1 μm. An intelligent bit rollover used by the PMAC allows to move to positions beyond the 16 bit range as long as the maximum size of a single step is not exceeded.

The data acquisition is all handled by a single multifunction PCI board[19] that provides 16 analog to digital converters (ADC) channels with a sampling rate of up to 333 kS/s and 2 counter channels. By default 8 (designed for up to 14) of the ADC channels are used to read the voltage signals from an integrating

[14] Newport model MM3000

[15] National Instruments model PCI-GPIB

[16] Delta Tau ACC-8E

[17] Delta Tau ACC-8S

[18] National Instruments model PCI-6534

[19] National Instruments PCI-6052E

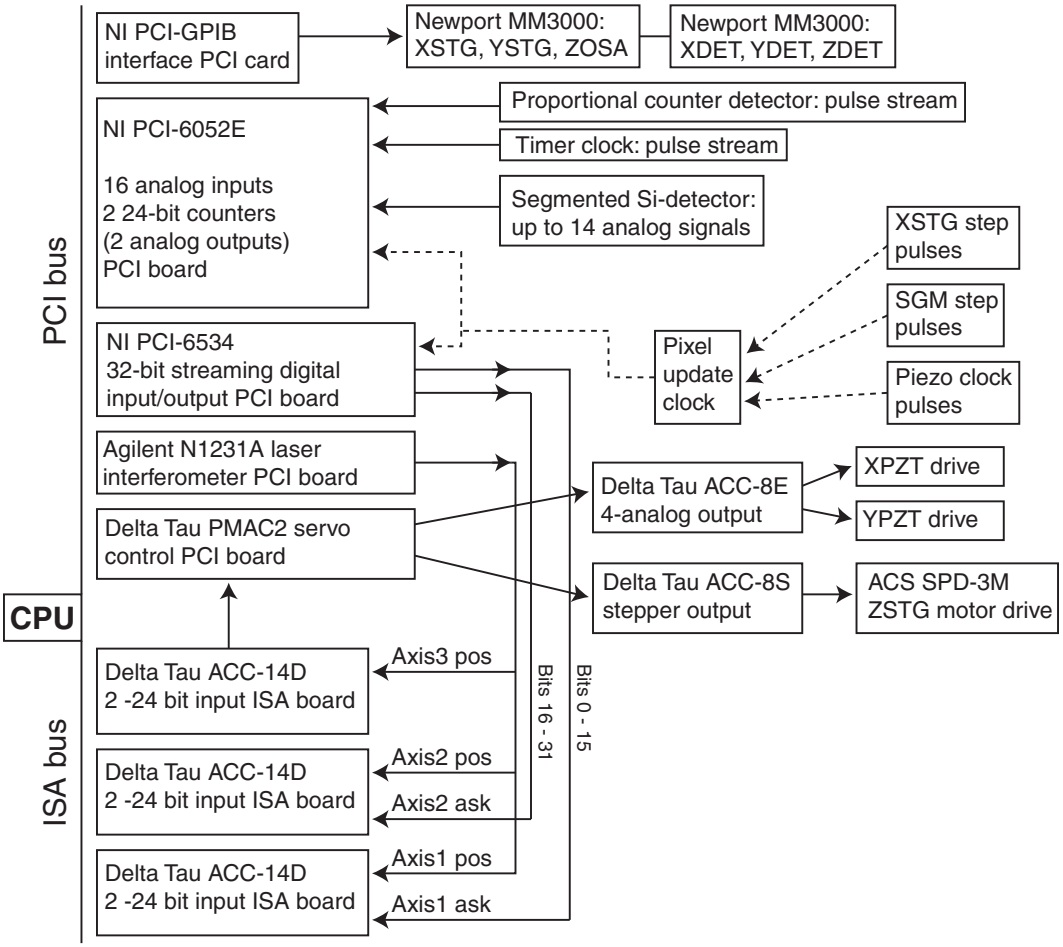

Figure 2.10: Electronics of the microscope control system. The PMAC2 tries to match the laser positions provided by the Agilent N1231A board and the commanded positions streamed by the NI PCI-6534 board. It controls the motors via the external ACC-8S (for Z stepper) and ACC-8E (for X/Y piezos) boards. The NI PCI-GPIB card communicates the control of all other stepper motors and the NI PCI-6052E card digitizes the measured x-ray signals.

segmented silicon detector used for differential phase contrast [9]. One of the counters can read the signal of a proportional counter x-ray detector, an x-ray luminescence detector or a pulse stream from any other kind of detector. The second counter counts a constant 100 kHz reference pulse stream as pixel clock.

To keep the data acquisition synchronous with scan positions we need a signal that coordinates the entire timing of a scan. Which signal is used for this task depends on the type of scan that is being recorded (compare to Tab. 2.3):

Piezo or focus scan: We rely on the timing accuracy of the internal clock of the digital streaming board. Along with the position update, it sends out a pulse that triggers the data acquisition.

Stepper or contrast scan: We tap into the step pulses from the motor controller to the fast axis stepper motor and use the signal to trigger the data acquisition. At the same time it triggers the recording of the pixel clock signal allowing for a normalization of the x-ray flux.

Point spectrum scan: We are trying to keep the sample in focus, while the energy changes. Before the scan starts we calculate the trajectory,[20] that the Z stepper should move on. The step pulses from the SGM then do not only trigger the data acquisition and recording of the pixel clock, but also the position streaming for ZSTG. (Ideal would be to also move ZOSA simultaneously, but the current system does not allow for this.)

Sec. 2.5.1 shows how the signal routing is done in detail.

2.5.1 Connection interface board

For routing of all data streams and control signals we have designed a single printed circuit board to be mounted in the same racks as the control computers. This clock/connection interface board is used to select the master clock signal as well as to provide a connection point for cables from all devices or boards.

Fig. 2.11 shows what signals we are dealing with and how they are being routed. Signal lines concerned with scan timing are shown in red. The master clock pulse is used to coordinate a scan on a pixel-by-pixel bases. The upper

[20] The trajectory is a hyperbola, since the SGM moves linear in wavelength, while the focal length is proportional to the energy.

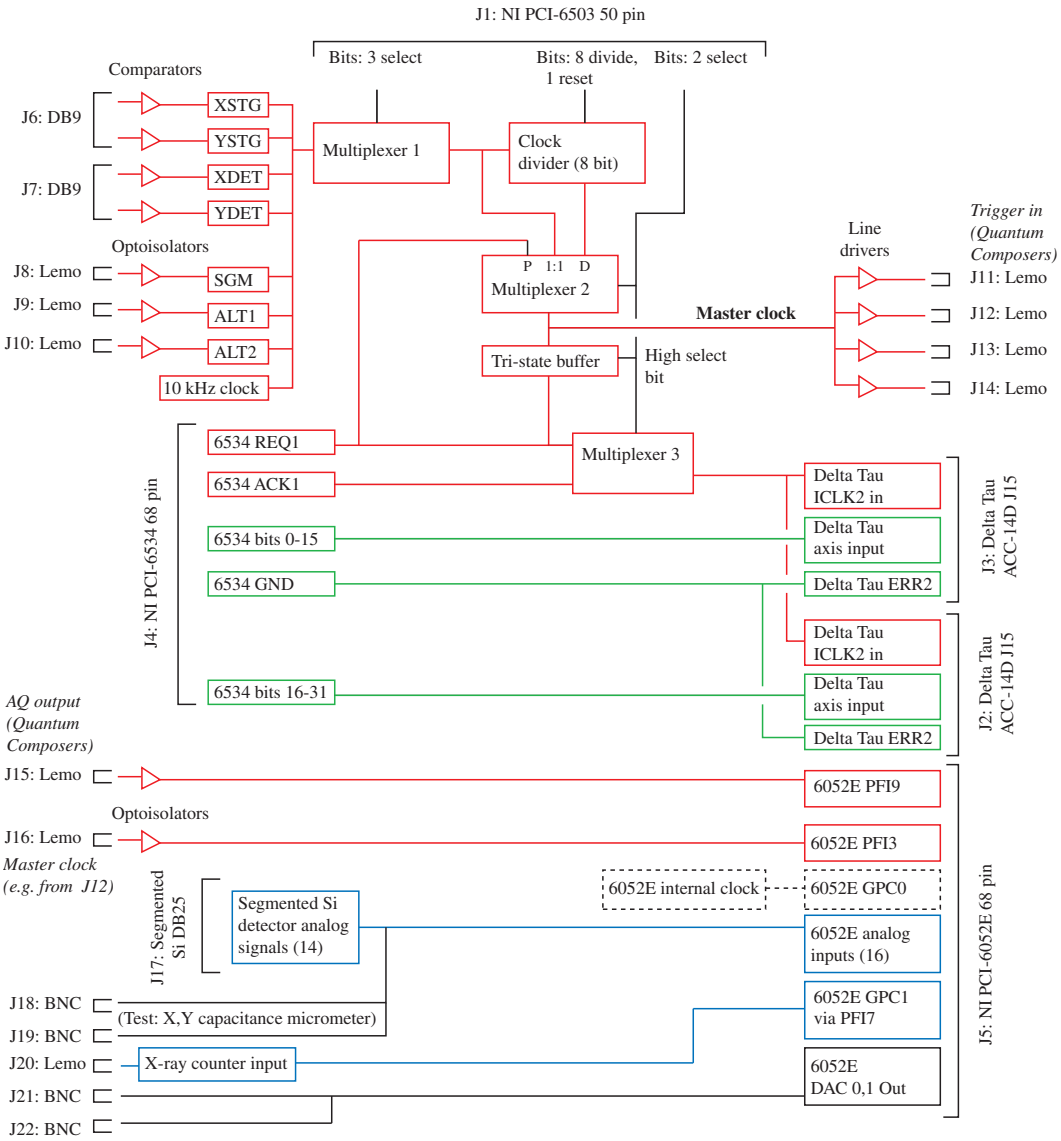

Figure 2.11: Functional diagram of the clock/connection interface board. This board is used to select the master clock signal and to connect all devices and computer boards as needed. The parts are color coded as follows:
red: timing
green: position streaming
blue: detector signals
black: auxiliary

third of the schematic shows what signals it can be chosen from (on the left) and how it is put out to trigger the acquisition of individual data points. The timing is dictated by the motor of the fast scanning axis (see Tab. 2.3). Multiplexer 1 selects between stepper motor scans or spectral scans (SGM). In cases, where these devices produce more than one pulse per image pixel a clock divider is used to block out all additional pulses. The 8 bit divider provides for divisors from 2 to 257, so that one can have pixels of, for example, 1.0 μm size from motors with an intrinsic step size of 0.1 μm. Multiplexer 2 then chooses wether the pure (1:1) or the divided (D) pulse stream are used or - in case of piezo scans - the signal, that their positioning information has been updated (P). Multiplexer 3 deals with a specialty of internal and external triggering of the NI PCI-6534 board. With internal timing, the clock pulse is sent out of REQ1, while an external pulse is feed into REQ1 and the position update is then acknowledged to be stable with an output from ACK1.

The output of Multiplexer 2 is the master clock pulse signal. This signal is routed through line driver chips to provide externally-available output signals to possibly several devices. One of them is usually serves as trigger signal to a multifunction board (NI PCI-6502E), which is used to read analog voltages and/or count pulse streams shown in blue.

Another board (NI PCI-6503) provides up to 24 static digital bits that control the multiplexers and the clock divider chip. The green lines show how the 2×16 bit lines from the digital streaming board (NI PCI-6534) are routed into the Delta Tau accessory boards (ACC-14D).

All connectors were arranged to fit onto a single printed circuit board made to fit in a standard relay chassis for rack mounting. The complete layout[21] of the board is given in App. B. Also detailed pin-assignments of the boards and devices are given in the technical manuals by the x-ray microscopy group at Stony Brook University.[22]

2.5.2 Newport XPS motor controller

Delivery and service for the old stepper motor controllers "Newport MM-3000" was discontinued by the manufacturer. To be prepared for their possible failure

[21] done by Charles Pancake, Electronics Shop, Physics Department, Stony Brook University

[22] on http://xray1.physics.sunysb.edu/user/manuals.php

in the future, we upgrade one of the microscopes to the newer "Newport XPS-C8" with 6 "XPS-DRV01" motor driver cards. These universal driver cards can be programmed to work with almost any stepper (and DC) motor. (The previous system required driver cards specific to each motor model.) While the communication with the older controller was done via a GPIB[15] interface, the newer model is ethernet based which requires no hardware on the host computer side in addition to a standard ethernet adapter. The controller is running an HTTP and FTP server allowing for easy administration and motor control from any web browser with internet connection. For dedicated operations the controller comes with various computer libraries (C++, Basic, LabView, ...) for TCP/IP socket communication enabling service from almost any operating system and even multiple users at once. To provide for an easy switch between the old and the new controller, we added a C++ class for the XPS controller providing the same methods as the old class for the MM3000 (see Sec.2.6).

Unlike the MM-3000, where we had to spy on the step pulses to the motor, to get a rough reference of the stage position, the new XPS controller provides "position compare pulses" directly. These 200 ns pulses are supposed have less than 50 ns latency from crossing designated positions. So the timing with the new controller is linked to the actual stage positions rather than the projected ones. Fig. 2.12 shows a comparison between timing curves of the MM-3000 (dotted) and XPS (blue) controllers. The lines scanned with the X sample stepper stage had 100 pixels of 2 μm size each with a desired (but not reached) dwell time of 1 ms per pixel. Both curves show how the stage accelerates, reaches its maximum defined speed[23] of 0.8 mm/s and then decelerates. The curve for the MM-3000 shows how step pulses are being sent out following a calculated curve. The curve for the XPS controller however follows the actual movement of the stage and is therefore not as smooth. Also the acceleration with the XPS seems to be a little higher.

The position compare output signals from a special 6 pin connector[24] are of open collector type and accept up to 30 V and 40 mA. In an adapter we use the 5 V output on the same connector with a 470 Ω resistor as pull-up to ensure fast transitions. The trigger lines can then be plugged into the existing inputs (J6/7) on the connection interface (see Fig. 2.11). (In a redesign the pull-up resistors might be added to the printed circuit board directly.)

[23] This was a soft limit defined for the MM-3000. Trusting the better pixel timing of the XPS, the maximum speed was later raised to the hardware limit of 2 mm/s.

[24] LEMO FGG.0B.306.CLAD52

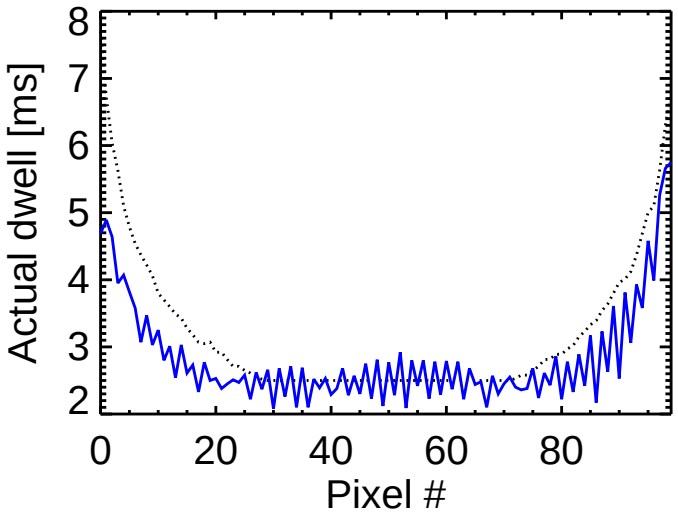

Figure 2.12: Comparison between timing curves of Newport MM-3000 (dotted) and XPS (blue) controllers. Shown is the actual duration of individual pixels in a 100 pixel scan line of 2 μm pixel size.

2.6 Software

A big part in the STXM 5 upgrade was the rewriting of the dedicated microscope software. Besides the need to incorporate code for operating the new hardware (see Sec. 2.5) and implementing a new scan concept (see Sec. 2.4.2), it was also a goal to improve the capabilities of the graphical user interface (GUI). In STXM 4 the GUI had been written in Qt[25] to form one big program comprising the microscope control code written in C++. The whole program would only run on two dedicated machines at the beamline and did not interface well with existing image processing and data analysis code in IDL. To make full use of IDL's superior image processing and GUI programming capabilities while at the same time building on previously existing C++ code for device control, STXM 5 is now operated by three separate programs:

`sm_server`: A microscope server program written in C++ is executing commands controlling the entire microscop hardware. This program is running permanently (and exclusively) on a rack-mount PC holding all the

[25] by Michael Feser

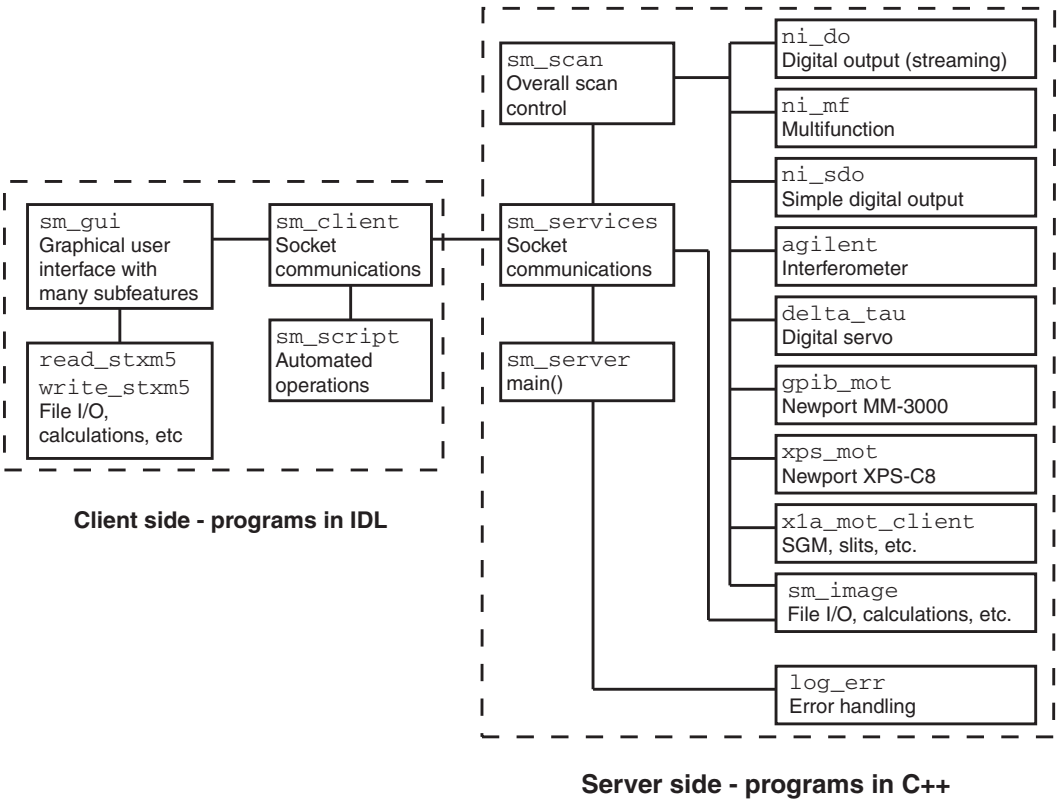

Figure 2.13: Software architecture. The software was kept as modular as possible. The server side was written in C++ and the client side in IDL

necessary control electronics.

`sm_gui`: A GUI written in IDL[26] displays and processes taken data. It can handle all STXM data independently from the microscope hardware and on any machine and operating system (Windows, Linux, Mac) that is running at least the "IDL Virtual Machine"[27]. If the pertaining computer has an internet connection to the microscope server machine (see Sec. 2.6.1), the GUI can be run in an extended version communicating with `sm_server` to control all microscope functions.

`sm_script`: Another IDL program allows to control most microscope features from the command line. It is typically used for automatized operation of the microscopes, following an ASCII script of control commands. Control scripts can be conveniently created with a graphical tool in `sm_gui`.

The architecture of the STXM 5 software is shown in Fig 2.13. We tried to keep things as modular as possible. (So for example the C++ class controlling the Newport MM-3000 motor controller could simply be replace with a new class for the XPS controller.) Since most of the manufacturers of the microscope control computer boards do not offer software or drivers for Unix platforms, the rack-mount PC running `sm_server` is operated under Windows 2000. It combines individual classes for all microscope device groups as well as for beamline control, file I/O, socket communication and error logging. The server machine is not meant to be accessed directly by beamline users.

The IDL GUI (see Fig. 2.14) is available to users by default on a Linux box, if they choose not to run it on their own computers. In its basic version the GUI allows to browse through data and offers features like image processing and statistics, noise plotting and fitting of spectral peaks. The full version in addition allows complete microscope control for alignment and operation, live monitoring of acquired data and to set up and run spectromicroscopic stacks in script mode (by invoking `sm_script`).

2.6.1 Networking

The communication between the server program and the GUI is done over two TCP/IP sockets - the server program obviously taking the role of network

[26] by Benjamin Hornberger

[27] a tool to run precompiled IDL code

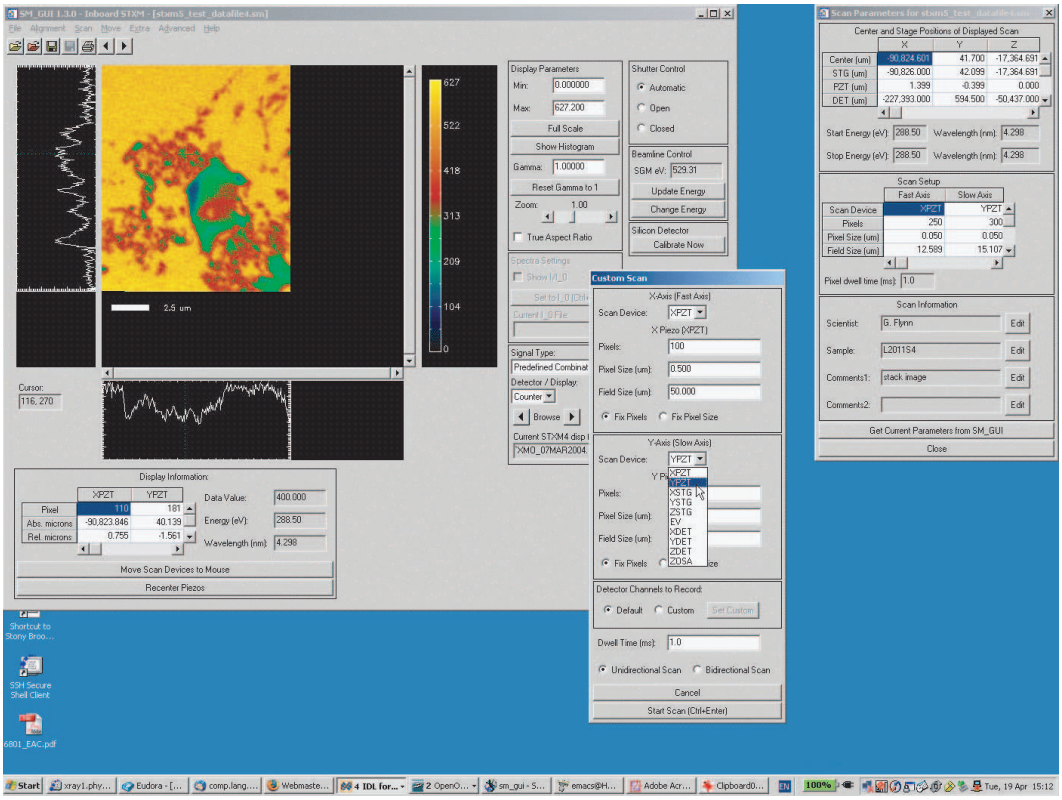

Figure 2.14: Graphical user interface. Custom written in IDL[26] it is dedicated to control STXM 5 at the NSLS. Besides all microscope control and data display (live as well as stored) it also offers image processing, statistics and a series of advanced features.

server and the GUI the one of the client. One socket is used for command the other for data flow. The data socket is used for example during a scan where the client asks periodically for the most recent data to be displayed in live-update, so the progress of a scan can be monitored while being collected. To avoid conflicts the server allows only one client program to connect at a time. To allow the communication between heterogeneous computer systems all data transferred over the network is encoded in the external data representation (XDR) by the sender and decoded to the local representation by the receiver. All standard commands are translated to short unsigned integers, so that the microscope can be controlled even over a slow dial-up connection. Only the live-update during a scan requires a moderately fast connection of ∼300 kbps or more. This is a big improvement to the old code, where the entire GUI had to be exported from the server machine, making it almost impossible to use even with the fastest internet connection.

More features make the remote control of the microscopes easier:

- The CCD images from the visible light microscope in the STXM chamber are being web cast[28] for viewing in any web browser.
- Thumbnails of all data taken appear on the Stony Brook x-ray microscopy group's web site[29] with at most 10 minutes delay. This is meant for easy monitoring of automatic operation of the microscopes, especially when users leave the beamline.
- The Newport XPS motor controller (see Sec. 2.5.2) allows to operate microscope motors in a web browser independently from our custom written software.

The thumbnails require a whole chain of steps to be provided on the web. After a periodic cronjob on the main X1A beamline machine copies recent files to the web server machine at Stony Brook University, another conjob there runs an IDL script to create PNG images from the data files. On demand a PHP script on the web site then searches for available thumbnail images and creates the HTML code to display them on one page and offer all files for download.

Note: Brookhaven National Lab restricts outside access to their network for security reasons. This means, that a user who wants to control STXM from

[28] with an Axis 241Q Video Server

[29] http://xray1.physics.sunysb.edu/data/thumbs.php

outside BNL needs an account on their SSH gateway to be able to tunnel all necessary ports to a local machine. The user manual for STXM 5[22] lists all port numbers and explains in detail how the tunnels are set up.

2.6.2 Noise filter

There are many possible sources for periodic noise in a STXM image: electric line noise in the detector, residual ambient light in the chamber[30] from the fluorescent light bulbs on the experimental floor or noise present in the x-ray beam to name a few. The GUI offers a notch filter [23] to reject frequencies from systematic noise.

This filter in the frequency domain works as follows: The Fourier transform $F(u, v)$ of the image is multiplied with a filter function $H(u, v)$ and the result is inversely transformed to regain a real space image:

$$\text{Filtered Image} = \mathscr{F}^{-1}\left[H(u,v)F(u,v)\right] \tag{2.1}$$

The 2D discrete Fourier transform can be defined as

$$F(u,v) = \frac{1}{N_x N_y} \sum_{x=0}^{N_x-1} \sum_{y=0}^{N_y-1} f(x,y)\, \mathrm{e}^{-2\pi \mathrm{i}\left(\frac{ux}{N_x}+\frac{vy}{N_y}\right)} \tag{2.2}$$

and the inverse transform as

$$f(x,y) = \sum_{u=0}^{N_x-1} \sum_{v=0}^{N_y-1} F(u,v)\, \mathrm{e}^{2\pi \mathrm{i}\left(\frac{ux}{N_x}+\frac{vy}{N_y}\right)} \tag{2.3}$$

where x, y are the indices the real space image array and u, v the indices of the Fourier space array. N_x, N_y are the numbers of image points in both dimensions.

The sampling intervals in the spatial domain $\Delta x, \Delta y$ relate to the sampling

[30] only relevant for detectors sensitive to visible light, like a silicon chip detector [9]

intervals in the frequency domain $\Delta u, \Delta v$ as

$$\Delta u = \frac{1}{N_x \Delta x} \quad \text{and} \tag{2.4}$$

$$\Delta v = \frac{1}{N_y \Delta y} \, . \tag{2.5}$$

While the above definition of the Fourier transform will have the zero frequency at the zero element of the array, it is convenient for visualizations and handling to rearrange the data points such that the array is centered around the zero frequency. For an odd number of pixels in either dimension i this is exactly possible, since the the frequencies can be rearranged as

$$\frac{1}{N_i \Delta i} \left(-(\tfrac{N_i - 1}{2}), \ldots, -1, 0, 1, \ldots, \tfrac{N_i - 1}{2} \right) \, . \tag{2.6}$$

However, since arrays with an even number of elements have no center element, the frequencies have to be arranged as

$$\frac{1}{N_i \Delta i} \left(-\tfrac{N_i}{2}, -(\tfrac{N_i}{2} - 1), \ldots, -1, 0, 1, \ldots, \tfrac{N_i}{2} - 1 \right) \tag{2.7}$$

with the zero frequency right next to the center. The shifted Fourier transform (for the even case) can be written as $F(u - N_x/2, v - N_y/2)$. The shift has to be undone, before an inverse transform is applied.

In the case of (STXM) images $f(x, y)$ is real, so that the Fourier transform is conjugate symmetric:

$$F(u, v) = F^*(u, v) \tag{2.8}$$

$$\Rightarrow |F(u, v)| = |F(-u, -v)| \tag{2.9}$$

So in a shifted array the spectrum of the Fourier transform is symmetric about the center of the array. The same has to be true for any filter in the frequency domain that we want to apply.

In a piezo scan, where the pixel dwell time is constant throughout the scan, periodic noise will appear as diagonal[31] streaks in the image (see left of Fig. 2.15). The noise filtering tool in `sm_gui` can display the 2D Fourier transform of the

[31] or vertical, if the time between scan lines happens to be a multiple of the noise period

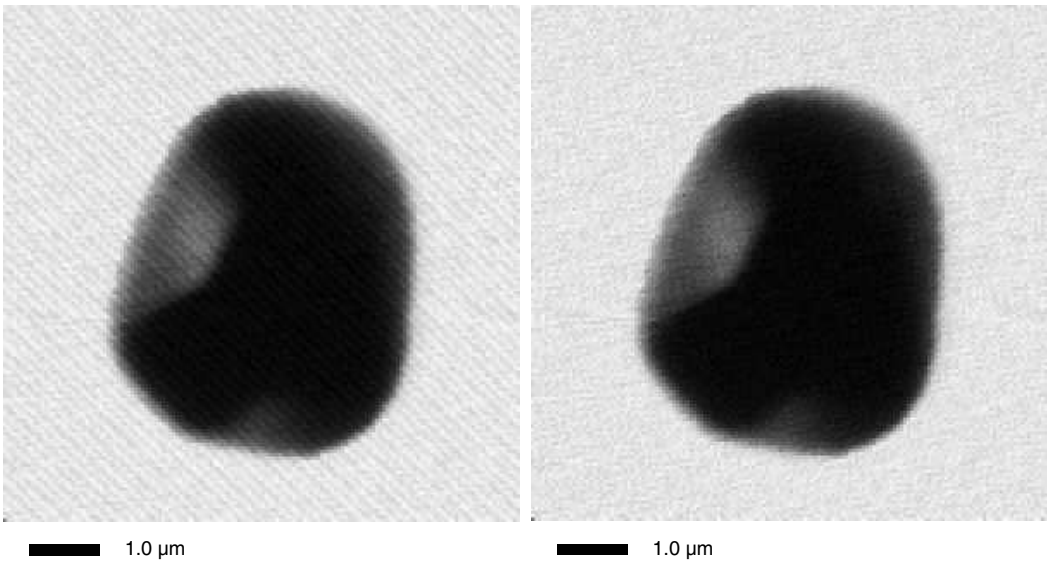

Figure 2.15: Demonstration of noise filtering. The left image shows diagonal streaks of line noise. On the right is the same image after the noise has been filtered out.

image (see top of Fig. 2.16) and overplot it with an axis (green) showing the corresponding temporal frequencies. This particular case has frequency peaks around 60 Hz and 120 Hz and of course also at points symmetric around the center. Gonzalez and Woods [23] propose three types of notch filters to reject the frequency areas around the peaks:

Ideal filter: The simplest way is to set all elements in within a specified distance from the peak to zero. However the sharp edges of an ideal filter can lead to characteristic artifacts like "ringing".

Gaussian filter: To avoid ringing a filter with gradually rising edges like for example a 2D Gaussian bell-curve can be applied.

Butterworth filter: Another example with smooth edges is a Butterworth filter (typically of second order).

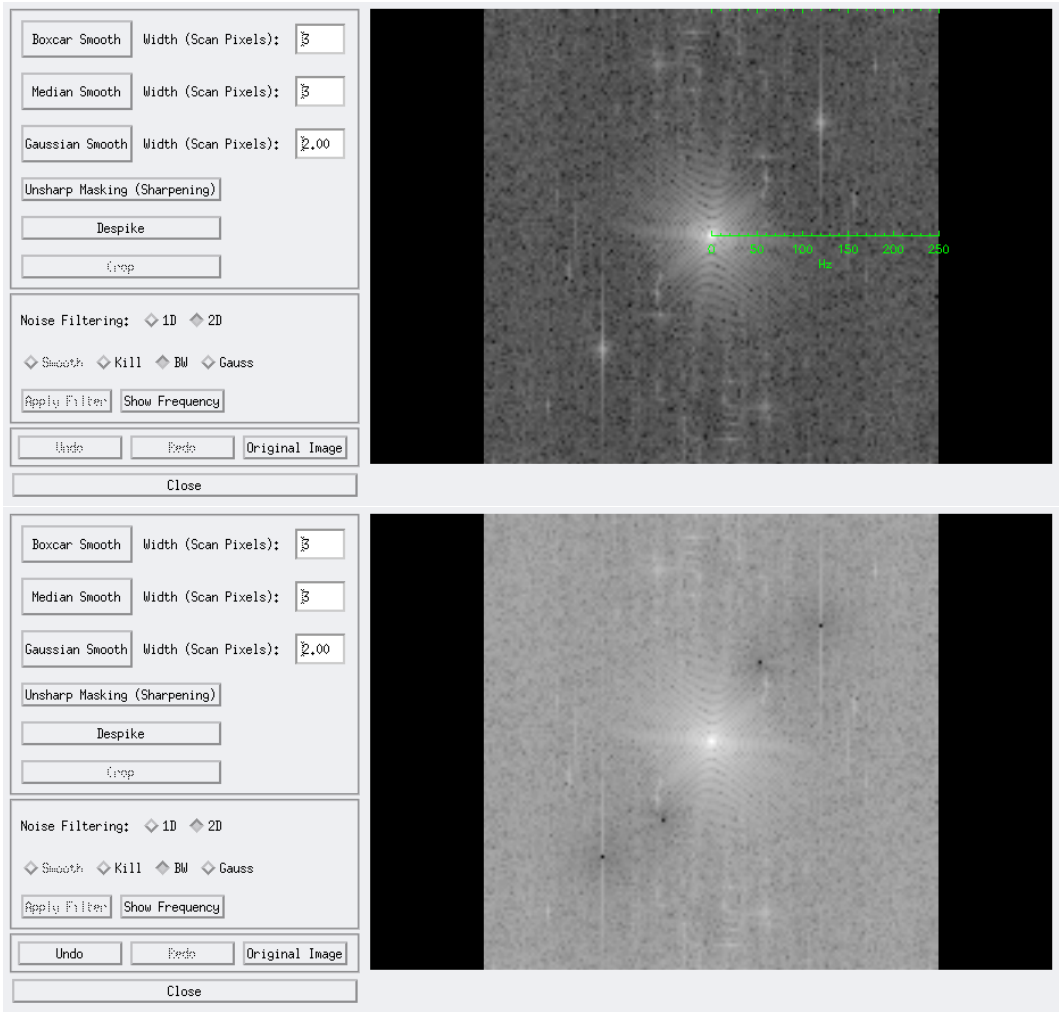

Figure 2.16: Fourier transform for noise filtering. The upper image shows the 2D Fourier transform of the noisy image. Overlaid in green is an axis of corresponding temporal frequencies. The lower image shows the Fourier transform after applying a Butterworth filter at two different points.

The ideal notch reject filter can be defined as

$$H(u,v) = \begin{cases} 0\,, & \text{if } D_1(u,v) \le D_0 \text{ or } D_2(u,v) \le D_0 \\ 1\,, & \text{otherwise} \end{cases} \tag{2.10}$$

$$D_1(u,v) = \left[(u - N_x/2 - u_0)^2 + (v - N_y/2 - v_0)^2\right] \tag{2.11}$$

$$D_2(u,v) = \left[(u - N_x/2 + u_0)^2 + (v - N_y/2 + v_0)^2\right] \tag{2.12}$$

where the two notches of radius D_0 are centered at the symmetric locations (u_0, v_0) and $(-u_0, -v_0)$.

The Gaussian notch reject filter is defined as

$$H(u,v) = 1 - \mathrm{e}^{-\frac{D_1(u,v)D_2(u,v)}{2\,D_0^2}}\,, \tag{2.13}$$

with $D_1(u,v)$ and $D_2(u,v)$ as in Eqs. 2.11 and 2.12, respectively.

The Butterworth notch reject filter is given as

$$H(u,v) = \frac{1}{1 + \left[\frac{D_0^2}{D_1(u,v)D_2(u,v)}\right]^n} \tag{2.14}$$

where the order n is usually chosen as 2 for our purposes.

The GUI has radio buttons to choose between the filter types and lets the user select center and radius of the notch by dragging the mouse over an area in the displayed Fourier transform. Fig. 2.16 at the bottom shows the Fourier transform after a Butterworth filter has been applied at the locations of two frequency peaks. The symmetric locations are included automatically. The final result of the noise filtering can be seen on the right of Fig. 2.15.

2.6.3 Drift correction

If the axis of motion the Z sample stepper is tilted with respect to the x-ray beam axis, the x-ray focus will fall onto different positions on sample at different energies. This is, because the ZSTG position (meaning the distance between sample and ZP) has to be adjust as the energy is changed. The same is true, if the coordinate system of the interferometer setup, defined by the mirror alignment, is off. This misalignment leads to a linear drift of the sample relative to the defined field of view in a stacks and can also ruin pointspectra.

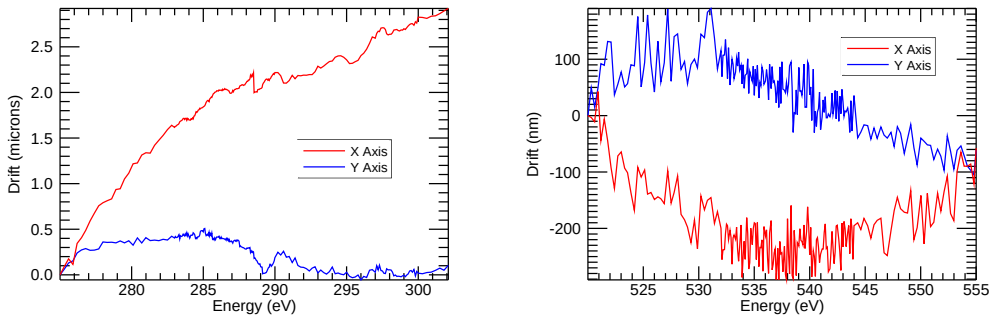

Figure 2.17: Plot of STXM drifts. Before the interferometer upgrade typical drifts were in the range of a few microns (left). After the interferometer upgrade and with active correction the drift could be reduced by one order of magnitude (right).

A manual realignment of the microscope chamber or mirrors is cumbersome and easily disturbed in a system floating on air. In the STXM 5 software we added routines for active drift correction.

For example before starting a long stack, the user can acquire one scan at the low energy and another at a higher end, and then have an automatic script calculate the current drift from the two images. A linear correction is then added to the positioning parameters at different x-ray energies. Together with the precision of the new laser positioning system this correction improved the reproducibility of an image field by one order of magnitude. Fig. 2.17 shows an example of drifts in the old (left) and the new system (right).

To correct for the drift in point spectra, along with the positions for ZSTG (see Sec. 2.5) we are streaming corrections on the piezo axis with the larger drift. Better would be to stream corrections on both axes (X and Y), but the current hardware setup only allows the stream 16 bit positions on two axes. To improve this, one could purchase digital streaming boards with more than 32 bits and split them up equally on all three axes, or in a redesign of the connection interface board (see Sec. 2.5.1) one could reroute 8 lines from the second streaming axis to allow for small corrections in both transverse directions. In this scenario Z positions would still be streamed with 16 bit precision and corrections on X and Y with 8 bit precision each. 8 bit at 0.309 nm resolution would allow for step sizes of up to ±39.6 nm, which can suffice for small drifts and small energy steps in a spectrum.

2.7 Results and outlook

We have already seen few improvements by the STXM 5 upgrade in previous sections. The new scan concept reduced the acquisition time of piezo scans as well as the radiation damage at the beginning of scanlines (see Sec. 2.4.2. High resolution laser positioning and active drift correction, if used consistently, reduce the drift of the focal spot during changes of the x-ray energy (see Sec. 2.6.3.

The perpetuation of the focus in the Z direction could also be improved, as is illustrated in Fig. 2.18 showing a stack of a diatom sample at the carbon edge. The time difference between the first and the last image being taken was over 8 hours. The lower rows of real images show, that the sample is kept in focus over this extended period of time. At each new energy the laser feedback system allows to correct the real Z positions in closed loop. While this had already been presented by Mirna Lerotić [20], the upper rows have been added to the figure shown here. They display difference maps of an image and its successor. The images were thresholded with their median intensities before taking the difference. The maps show differences of single pixels only at the edges of the diatom structure. There are no considerable distortions of the image field throughout the stack.

STXM 5 has been running on both branches beamline X1A for over 3 years now and albeit the overall success shown in this chapter, there is of course always room for further (at least minor) improvements. Like in any other system of increasing complexity, the sources of errors also grow in number. But while this is an ever ongoing fight at many battlefronts, there are a few concrete points to be mentioned:

- As mentioned in earlier sections a thorough redesign of the connection interface can improve the operations of the microscope in a series of ways. (Better drift correction in spectral scans, no need for adapters like for interfacing the Newport XPS motor controller ...)

- The servo cycle of 442 μs in the Delta Tau PMAC is hardly fast enough for current operations and will certainly not suffice to run STXM well below the millisecond dwell time regime. (Shorter dwells would be desirable with a higher performance source as for example NSLS-II will be in the future.)

- Due to the lack of space in the STXM chamber, the alignment of the

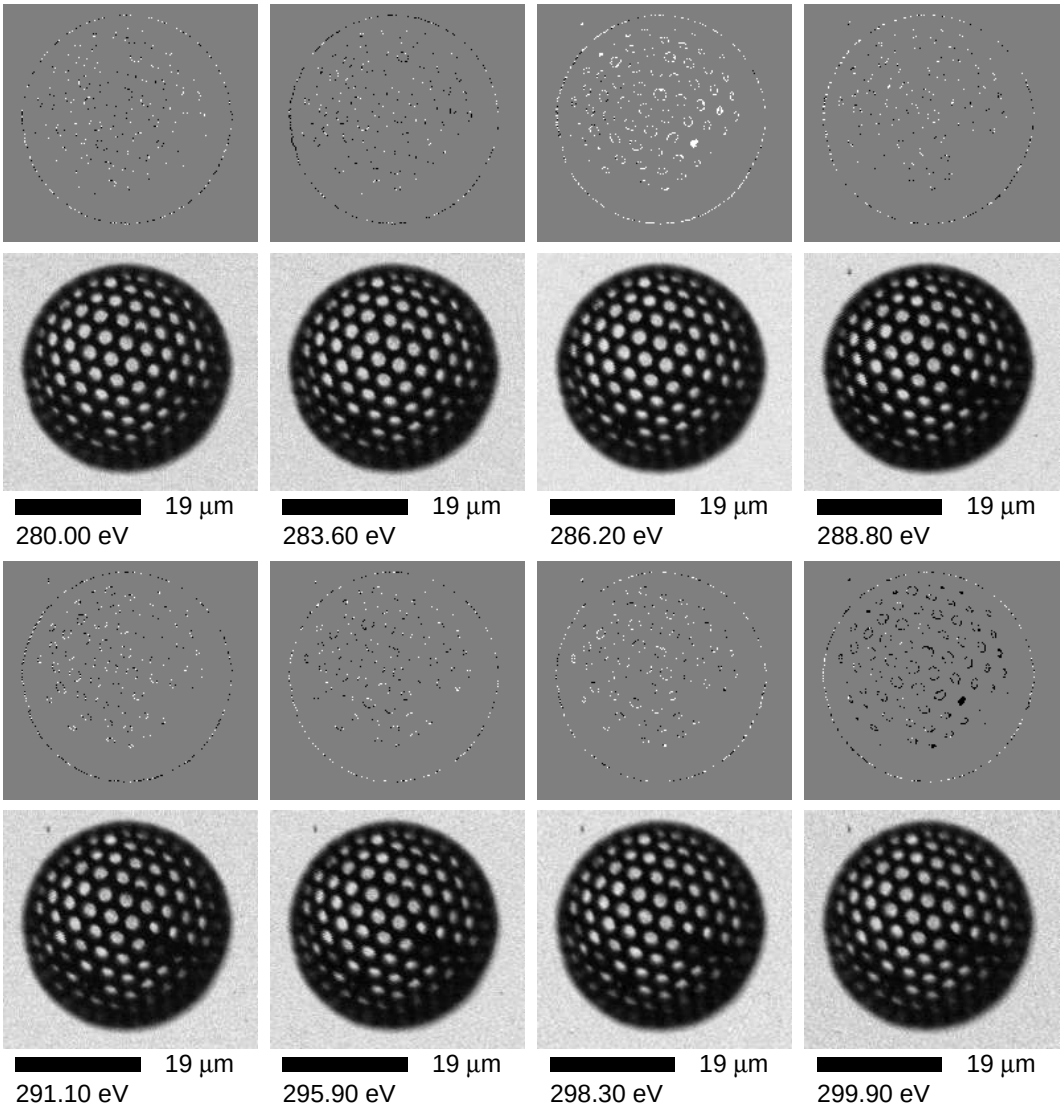

Figure 2.18: A few images from a stack taken of a diatom sample with the new system. The stack images in the lower rows show, that the closed loop position corrections keep the sample in focus over an extensive period of time [as already presented in [20]]. The upper rows show the difference (thresholded) of an image and its succeeding image (cyclic). The differences are restricted to single pixel areas. This indicates no considerable distortions of the image field within the data set.

interferometer mirrors on sample mount and zone plate assembly is extremely cumbersome.

- Fluctuations in the helium flow on the outboard microscope influence the optical path length of the laser system. Especially when the helium flow is turned on or off this can lead to noticeable disturbances.

But in spite of these (minor) quirks STXM at the NSLS should remain an instrument attractive to users from many fields and countries in the years to come.

Chapter 3

Non-negative Matrix Factorization

3.1 Introduction

Spectromicroscopy is the powerful combination of spectroscopy and microscopy allowing the study the chemistry of specimens at the spatial resolution of an infrared, x-ray or electron microscope. (The latter in particular when plural inelastic scattering can be neglected or corrected for.) An example is the use of near-core-edge spectroscopic resonances due to partially occupied molecular orbitals, such as in x-ray absorption near-edge structure (XANES) spectroscopy or electron energy-loss near-edge structure (ELNES) spectroscopy (where the term "spectrum imaging" is common). Fourier transform infrared (FTIR) and coherent anti-Stokes Raman (CARS) spectroscopies also provide chemical speciation with spatial resolution. Satellite imaging of spectral reflectivity (sometimes called "hyperspectral imaging") again provides information with similar characteristics though at a larger size scale.

For many specimens, spectromicroscopy provides rich and complex data. In the soft x-ray XANES examples discussed here, the data are formed by a set of images with 10^4–10^5 pixels each at one of 10^2 or more photon energies. Because so many spectra are obtained in one measurement, it is impractical to examine them individually. If the specimen is known to be comprised of only a few nonreactive phases of materials with known spectral response, one can do a simple mapping of the presence of these materials in the specimen. However, if the specimen contains other materials or reactive phases with different, unknown spectral response, one must attempt to recover these spectra from the data for subsequent analysis. This is often the case with biological or environmental science specimens, where there may be great variation in spectroscopic response at the finest measurable length scales.

Principal component analysis (PCA) [24], which requires relatively little computing power, delivers an orthonormal basis set for representation of all spectra within the data set; in most cases one can use a small subset of these spectra to represent all the non-noise variations in the data. In this way one gains insight into the main differences between various chemical signatures in spectromicroscopy data [25, 26], but with a major limitation: all component spectra beyond the first are difference spectra with positive and negative responses, and therefore they do not have direct physical interpretation. One way to overcome these limitations is to use the non-noise subset of the principal components as a reduced, orthogonal search space for cluster analysis [27]. This has been used by Lerotic et al. [28, 29] to group pixels together based on their spectroscopic similarity and obtain average spectra from these groups.

A subsequent matrix inversion provides maps of the relative presence of these representative spectra in the data. While this approach has proven to be of great use, it is not without its limitations in that the set of signature spectra obtained may incompletely and/or redundantly span the space of all spectroscopic responses in the specimen, which has the effect of recovering negative (non-physical) concentration in some pixels. (A discussion on this topic can be found in the last chapter of the Ph.D. thesis by Mirna Lerotić [20]).

The proper choice of a factorization method is mainly determined by the kind of results one wishes to achieve [30]. The eigenspectra found by PCA itself do not represent real spectra of any chemical components in the specimen. As an alternative we present here non-negative matrix factorization (NMF), which is an iterative technique of separating our data into two factors under non-negative constraint. The calculation is more demanding in terms of CPU time, but the results of a successful computation may be identified as real without further processing.

A number of multivariate statistical analysis (MSA) approaches have been used to similarly obtain characteristic spectra that can be used for subsequent analysis. Kotula et al. [31] applied constraint alternating least squares algorithms and relaxed the orthogonality constraint to extract pure instead of the usually mixed components from PCA. Bonnet et al. [32] had shown earlier that the underlying model of an entire data series can be found in the course of the analysis, which can make the a priori definition of an evolution model for interpolation (or extrapolation) unneccesary.

3.2 Data

3.2.1 Simulated data sets

In order to demonstrate the qualities of NMF, we created two simulated data sets as examples for specimens with well known composition and component spectra. We used experimentally measured carbon K-edge absorption spectra of pure thin films of collagen, leucine and tyrosine. The spectra of the amino acids tyrosine and leucine were measured by Kaznacheyev et al. [33], and the collagen spectrum was measured by A. Osanna (unpublished).

The less complex test data is a set of 4 letters (A-D) over a flat background

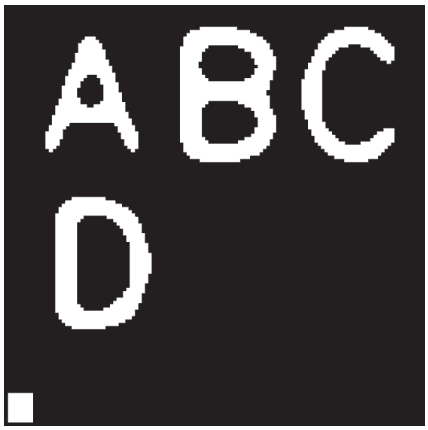

Figure 3.1: The black area in the first test specimen was assigned the transmission spectrum of 110 nm of collagen, 60 nm tyrosine and 30 nm leucine. Letter A was assigned the transmission spectra of 100 nm of collagen and 100 nm of leucine, B 100 nm collagen and 100 nm tyrosine, C 20 nm of collagen and 180 nm of leucine, D 20 nm of collagen and 180 nm of tyrosine. The square at lower left was assigned to be nonabsorbing so as to provide an I_0 flux normalization region.

(see Fig. 3.1). The specimen was constructed to have a uniform thickness of 200 nm in a 128 by 128 pixel array, with a 10 by 10 pixel hole at the lower left corner. The background, which covers most of the specimen, was assumed to be 55% collagen, 30% tyrosine and 15% leucine; the letter shaped regions were assumed to have different compositions. The letter A was given a composition of 50% collagen and 50% leucine, B 50% collagen and 50% tyrosine, C 10% collagen and 90% leucine and D 10% collagen and 90% tyrosine.

To better approximate more complex specimens we also created a test data set in the form of a hemisphere in an "empty" background (see Fig. 3.2). The hemisphere with radius of 64 pixels (giving a total of $P = 129 \cdot 129 = 16641$ pixels) and a maximum thickness of 200 nm consists mainly of tyrosine. A smaller hemisphere of collagen, that forms the core, is one third of the size of the large hemisphere. The remaining component leucine forms a sphere segment with a segment radius equal to the radius of the larger hemisphere, and the height of the smaller hemisphere, except with the smaller hemisphere subtracted.

We then simulated a flux of 1000 photons 'incident' on both artificial samples at each pixel and energy. The energies of the photons were chosen from the near-edge absorption region of carbon between 282 and 302 eV in 133 evenly

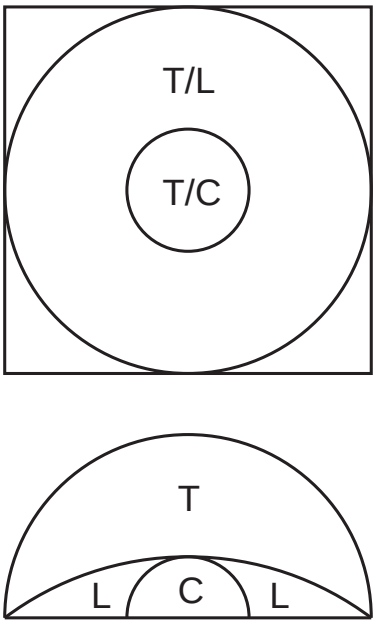

Figure 3.2: The second test specimen has a hemisphere of collagen of 67 nm height as core. It is surrounded by a sphere segment of leucine of equal height. The rest of the 200 nm high larger hemisphere is filled with tyrosine. The remaining area of the square sample was left to be nonabsorbing so as to provide an I_0 flux normalization region.

spaced steps. To approximate the shot noise present in real data, we then added Gaussian distributed random numbers with a mean of zero and standard deviations of the square roots of the "transmitted" intensities (with the results constrained not to be negative).

3.2.2 Experimental data sets

We also show analysis results of three real data sets, which have all been acquired in the scanning transmission x-ray microscope (STXM) at beamline X1A of the National Synchrotron Light Source (NSLS).

The first set was taken[1] on a sample of embedded wood fibers, microtomed into sections of roughly 200 nm thickness and mounted on silicon nitride windows

[1] work of Chris Phanopoulos (Huntsman International LLC) and Alan Michette (King's College, London)

of 50 nm thickness. This sample was chosen for a demonstration of NMF, because it is relatively incomplex (like the first simulated data set) and point spectra for reference had been taken of the pure main components. These are *wood* as the main fiber body, *cellulose* in the cell walls, *lignin*, which is also known to appear in the cell walls and in the middle lamella holding the cells together, and *LR White Resin* as embedding medium.

The other two data sets were taken[2] of particles[3] collected from comet *81P/Wild 2* in NASA's *Stardust* mission [34, 35]. The particles in general were extracted from tracks in aerogel. Those particular ones had afterwards been embedded in epoxy and sectioned using an ultramicrotome. This caused problems in the analysis with methods like cluster analysis, since all spectra were dominated by the epoxy background.

3.3 Analysis of x-ray spectromicroscopy data

Fundamental for the absorption of x-rays in a thin film of thickness t is the Lambert-Beer law

$$I(E) = I_0(E)\, \mathrm{e}^{-\mu(E)\, t} \,. \tag{3.1}$$

It describes the transmitted x-ray flux $I(E)$ as it depends on the incident flux $I_0(E)$ and an energy dependent absorption coefficient

$$\mu(E) = 2 r_e N_A \frac{hc}{E} \frac{\rho}{A} f_2(E) \,. \tag{3.2}$$

In the above expression, $r_e = 2.818 \cdot 10^{-15}\,\mathrm{m}$ is the classical electron radius, $N_A = 6.022 \cdot 10^{23}\,\mathrm{mol}^{-1}$ is Avogadro's number, $h = 6.626 \cdot 10^{-34}\,\mathrm{Js} = 4.136 \cdot 10^{-15}\,\mathrm{eVs}$ is Planck's constant, $c = 2.998 \cdot 10^8\,\mathrm{m/s}$ is the vacuum speed of light, A is the atomic weight, ρ is the density, and $f_2(E)$ is the imaginary part of the oscillator strength per atom as tabulated by, for example, Henke et al. [36]. The first fraction in Eq. 3.2 can also be read as x-ray wavelength λ, since it relates to the energy E as

$$E \cdot \lambda = hc = 1239.842\,\mathrm{eV} \cdot \mathrm{nm} \,. \tag{3.3}$$

[2] by George Flynn (SUNY Plattsburgh) and Sue Wirick (Stony Brook University)

[3] numbers *FC12,0,16,2,4* and *FC12,0,16,1,2*

If $\mu(E)$ is known and the optical density $D(E)$ of the film is defined as

$$D(E) = -\ln\left(\frac{I(E)}{I_0(E)}\right) = \mu(E)t\ , \tag{3.4}$$

we can calculate the thickness as $t = D(E)/\mu(E)$. However, specimens in microscopy are usually not uniform! By taking a series of electron energy-loss spectra at adjacent positions in spectrum imaging [37, 38], or a sequence of x-ray images over a series of energies in spectromicroscopy [22, 39], information is obtained on both the spatial and spectroscopic variations in the specimen. We will describe the data thus obtained in terms of an optical density or data matrix $D_{N\times P}$, where $n = 1,\ldots,N$ indexes the energies and $p = 1,\ldots,P$ indexes pixels. ($p = i_{\text{col}} + (i_{\text{row}} - 1)\cdot n_{\text{rows}}$ is a compound index derived from the image indices $i_{\text{col}} = 1,\ldots,n_{\text{cols}}$ and $i_{\text{rows}} = 1,\ldots,n_{\text{rows}}$.) Assuming there are $s = 1,\ldots,S$ spectroscopically distinct components in the specimen, we write the data matrix $D_{N\times P}$ as

$$D_{N\times P} = \mu_{N\times S} \times t_{S\times P}\ , \tag{3.5}$$

which is the product of matrices for absorption spectra $\mu_{N\times S}$ and thickness maps $t_{S\times P}$.

In the case where the exact absorption spectrum for each of the $s = 1\ldots S$ components in $\mu_{N\times S}$ is known, Eq. 3.5 can be solved for the entire set of spatially resolved thickness maps $t_{S\times P}$ via matrix inversion:

$$t_{S\times P} = (\mu_{N\times S})^{-1} \times D_{N\times P} \tag{3.6}$$

One way to find these quantitative maps of the specimen's composition is to invert the known spectra matrix $\mu_{N\times S}$ by singular value decomposition [40, 41]. However, if we have unknown spectroscopic components or reactive phases, we must attempt to recover both the spectra $\mu_{N\times S}$ and thickness maps $t_{S\times P}$ from the data $D_{N\times P}$. A variety of multivariate statistical analysis approaches have been used to accomplish this, as pioneered in electron microscopy by Bonnet et al. [42, 43]. One approach is to use principal component analysis (PCA), which has found previous use in x-ray spectromicroscopy [25, 26], by forming a spectral covariance matrix $Z_{N\times N} = D_{N\times P} \times D^T_{P\times N}$. One can then carry out an eigenanalysis of this matrix of

$$Z_{N\times N} \times C_{N\times S_{\text{abstract}}} = C_{N\times S_{\text{abstract}}} \times \Lambda_{S_{\text{abstract}}\times S_{\text{abstract}}} \tag{3.7}$$

where $S_{\text{abstract}} = N$. $\Lambda_{S_{\text{abstract}}\times S_{\text{abstract}}}$ is a diagonal matrix whose diagonal

elements are eigenvalues $\lambda(s)$ for $s = 1, \ldots, S_{\text{abstract}}$, and $C_{N \times S_{\text{abstract}}}$ is an eigenspectrum matrix. Given that C is a matrix of eigenvectors, we can use its orthogonality ($C^{-1} = C^T$) to find a set of corresponding eigenimages as

$$R_{S_{\text{abstract}} \times P} = C^T_{S_{\text{abstract}} \times N} \times D_{N \times P} \, . \tag{3.8}$$

However, these eigenspectra and eigenimages are not directly physically interpretable, for they contain both positive and negative values of optical density $D = \ln(I/I_0)$. This is natural for principal component analysis which seeks to find successive difference spectra that represent the variations present in the data; however, it is not helpful for direct interpretation because negative values of D correspond to negative absorption, which is not physical. In recognition of this, Lerotic et al. [28, 29] have used principal component analysis as a way to generate a noise-filtered and orthogonalized data matrix

$$D'_{N \times P} = C_{N \times \bar{S}_{\text{abstract}}} \times R_{\bar{S}_{\text{abstract}} \times P} \tag{3.9}$$

from a subset $\bar{S}_{\text{abstract}}$ of the eigenspectra, and have then used unsupervised pattern recognition or cluster analysis to segment the data, obtain a set of spectra $\mu_{N \times \bar{S}_{\text{abstract}}}$ from averaging over the pixels in each of the $s = 1 \ldots \bar{S}_{\text{abstract}}$ of the segmented regions and recover thickness maps of these signature spectra using Eq. 3.6.

The approach of principal component analysis followed by cluster analysis has proven to be of great use in dealing with the complexity of x-ray spectromicroscopy data. However, it is not uniformly successful in all analyses. The act of averaging over all spectra within a segment or cluster can obscure subtle variations within a cluster, or yield a set of spectra that do not completely span the space represented by the spectra at all pixels. When this is the case, maps of specimen thickness $t_{\bar{S}_{\text{abstract}} \times P}$ will contain negative and thus erroneous values. When these negative values are larger than the noise floor about zero optical density, improved approaches to spectromicroscopy analysis are required.

3.4 Non-negative matrix factorization

With principal component and cluster analysis, the goal was to find a set of spectra $\mu_{N \times \bar{S}_{\text{abstract}}}$ that represent all significant spectroscopic variations in

the set of measurements represented by all pixels P. We describe here an alternative approach: non-negative matrix factorization, as demonstrated by Lee and Seung [30, 44] for face recognition applications. In spectromicroscopy, our goal is to find a combination of spectra $\mu_{N\times S}$ and thicknesses $t_{S\times P}$ which represent well the measured data $D_{N\times P}$. As a measure for this Lee and Seung propose the following function F:

$$F = \sum_{N,P}(D_{N\times P} \cdot \ln(\mu_{N\times S} \times t_{S\times P}) - \mu_{N\times S} \times t_{S\times P}) \tag{3.10}$$

This cost function has a maximum[4] at $\mu_{N\times S} \times t_{S\times P} = D_{N\times P}$ and those pixels with larger optical densities $D_{N\times P}$ are weighted more strongly in the sum. Mathematically, F is related to the Kullback-Leibler divergence [45], a distance measure between two probability distributions (representing the data, and an approximation thereof) based on Poisson likelihood. In order to reach a local maximum of F, we follow Lee and Seung and set up an iteration with the following update rules (for a proof see App. A.1):

1. Initialize $\mu_{N\times S}$ and $t_{S\times P}$ to contain random non-negative values.

2. Generate an updated estimate of $\mu_{N\times S}$:

$$\mu_{N\times S} := \mu_{N\times S} \cdot \left(\frac{D_{N\times P}}{\mu_{N\times S} \times t_{S\times P}} \times t^T_{P\times S}\right) \tag{3.11}$$

   For those pixels where $\mu_{N\times S} \times t_{S\times P}$ gives larger values than those present in the data $D_{N\times P}$, this estimate update will drive $\mu_{N\times S}$ towards smaller values and vice versa.

3. Normalize each new spectrum, so as to transfer all of their relative weightings into the thickness maps $t_{S\times P}$:

$$\mu_{Ns} := \frac{\mu_{Ns}}{\sum_n \mu_{ns}} \tag{3.12}$$

4. Generate a new estimate of the thickness map $t_{S\times P}$ using the present

[4]The cost function has been simplified from its original form
$F = \sum_{N,P}(D_{N\times P} \cdot \ln(D_{N\times P}/(\mu_{N\times S} \times t_{S\times P})) - D_{N\times P} + \mu_{N\times S} \times t_{S\times P})$
by leaving out constant terms. This does not affect the update rules described later, but changes the extremum from a minimum to a maximum.

estimate for $\mu_{N\times S}$ and the data $D_{N\times P}$:

$$t_{S\times P} := t_{S\times P} \cdot \left(\mu_{S\times N}^{T} \times \frac{D_{N\times P}}{\mu_{N\times S} \times t_{S\times P}} \right) \tag{3.13}$$

5. Iterate over steps (2) to (4) until converged.

In order to avoid divide-by-zero errors in Eqs. 3.11 and 3.13, we find the set of pixels $\{S_0\}$ for which the present estimate of $\mu_{N\times S} \times t_{S\times P}$ is zero and set $\frac{D}{\mu\times t}\{S_0\} := 0$ when calculating a new update.

Besides the weighted cost function F given above, another possible function and iterative sequence is based on minimizing the Euclidean distance between $D_{N\times P}$ and $\mu_{N\times S} \times t_{S\times P}$, given by

$$F_E = \sqrt{\sum_{N,P} (D_{N\times P} - \mu_{N\times S} \times t_{S\times P})^2} \,. \tag{3.14}$$

To minimize the value of this new cost function, a different set of update rules is required (for a proof see App. A.2):

1. Initialize $\mu_{N\times S}$ and $t_{S\times P}$ to contain random non-negative values.

2. Generate a new estimate of $\mu_{N\times S}$:

$$\mu_{N\times S} := \mu_{N\times S} \cdot \frac{D_{N\times P} \times t_{P\times S}^{T}}{\mu_{N\times S} \times t_{S\times P} \times t_{P\times S}^{T}} \tag{3.15}$$

3. Normalize the new spectra:

$$\mu_{Ns} := \frac{\mu_{Ns}}{\sum_n \mu_{ns}} \tag{3.16}$$

4. Generate a new estimate of $t_{S\times P}$:

$$t_{S\times P} := t_{S\times P} \cdot \frac{\mu_{S\times N}^{T} \times D_{N\times P}}{\mu_{S\times N}^{T} \times \mu_{N\times S} \times t_{S\times P}} \tag{3.17}$$

5. Iterate over steps (2) to (4) until converged.

Again to avoid divide-by-zero errors, in this case we find the set of pixels $\{S_\mu\}$ where $[\mu_{N\times S} \times t_{S\times P} \times t^T_{P\times S}]$ is zero and set $\mu\{S_\mu\} := 0$ in step (2), and the set of pixels $\{S_t\}$ where $[\mu^T_{S\times N} \times \mu_{N\times S} \times t_{S\times P}]$ is zero and set $t\{S_t\} := 0$ in step (4).

3.4.1 Finding the correct number of spectra

The general problem implies that the correct number of components S is not known a priori. Our approach to this is to start out with a reasonably large number $S < \frac{N\cdot P}{N+P}$ and then reduce the number of components over the course of the iterations.

Typically, if the chosen number of components is larger than the real number of components, this will produce a series of spectra which are similar to each other. If the deviation (difference over average amplitude) between two spectra falls beneath a certain threshold, we merge those two according to their thickness weights. A threshold value of around 3% deviation per energy bucket has been found to work quite well. Another indicator for a "good merger" is if the value of the overall cost function changes by only a negligible relative amount as components are merged. In addition it would also be possible to merge components by hand after the inspection of intermediate results. However, the progress of the NMF calculations on the simulated data sets (Sec. 3.5.1), where we can compare the results with the original spectra, shows that a fully unsupervised factorization can be successful.

Another option is to remove spectra, that are obviously not representing any real component and/or are very thin. However this is not without risk. Unreal spectra that have been removed have been found to reproduce later on in many cases. Possibly they are contributed to noise present in the data. It may be better to keep those components and ignore them in an interpretation of the results. Also, while the removal of thin spectra does not affect the residual sum of squares too much, valuable information about traces of components might be lost.[5] But it is difficult to make this a general statement.

Results from a cluster analysis can be a good pointer to how many components to begin the NMF calculation from. Starting from a comparably small number of components leads to a substantial gain in computation time, since not only fewer iterations are required, but iterations are also faster, given that smaller

[5] An example of such a thin component with valuable information is shown in Fig. 3.14.

matrices are involved. While the number of clusters found indicates how many different spectral components are present in the sample, using the set of cluster spectra as starting matrix μ does not have a noticeable advantage over random initialization.

3.4.2 Smoothing spectra

Previous knowledge about the desired results can be exploited. Improved NMF algorithms have been devised to find sparse [46–49] or non-smooth [50] representations of the original data. We on the other hand are specifically interested in overlapping, non-sparse thickness maps. By acquiring spectral samples at a finer spacing than intrinsic peak widths and monochromator resolution dictate, we can expect the spectra to be "smooth". That is, they and their derivatives don't contain single point jumps or spikes. However, μ and t are initialized with random elements unrelated to each other, so by definition they are not smooth to begin with. A remedy for this is to introduce curve smoothing into the iteration algorithm [51]. After each step we perform a boxcar or gaussian smoothing on the spectra. A three to five point boxcar smooth and a gaussian smooth of the same effective width have been found to work equally well for the type of data analyzed here. While all spectral peaks are worn away by consecutive smoothing, they are reimposed by the measured data at each iteration step. However to restore peaks to their full height, it is advisable to run a few steps without curve smoothing at the end of an iteration.

3.4.3 PCA for noise reduction

Noise present in the measured data matrix D is a problem for finding a good factorization. It introduces a set of "artificial" components and distorts the spectra of real components. We have attempted to remedy this by using a reduced version of our data from PCA (Eq. 3.9). By throwing out higher principal components with small eigenvalues and noisy eigenspectra/-images from our data we can remove a substantial amount of the noise.

3.4.4 Targets

The spectra of one or more components may be known a priori. These spectra can be set as targets at the beginning of the NMF calculation to be reimposed at each iteration after recalculating μ (Eq. 3.11). Also the algorithm prevents targets from being included in a merger. If a "free" spectrum becomes similar to a target, its thickness is added to the target and the spectrum itself is removed. However, tests have shown that for an incomplete set of target spectra already small deviations from the actual spectra present in the data set lead to unsatisfactory results. Thus targets are difficult to apply to real data sets.

3.5 Results

3.5.1 Simulated data sets

For the "letters" data set, we chose the first three principal components to make up the reduced data matrix and a three point gaussian smooth at each iteration. Fig. 3.3 shows the results for the divergence related cost function. All three spectra (collagen, leucine and tyrosine) could be reproduced fairly closely. The original spectra are shown in solid red and the reconstituted spectra in dashed lines. The solid blue lines at the bottom of each plot show the difference between the two. The errors are small enough to allow for chemical identification of the components.

The progress of the same NMF calculation is shown in Fig. 3.4. Plotted are the values of the divergence related objective function (Eq. 3.10), the residual error cost function (Eq. 3.14) and the number of components over the course of the iteration. The divergence value would be monotonously increasing for a constant number of components and without curve smoothing. But at points where we reduce the number of components the value can decrease. Similar rules apply for the residual error. It is not strictly monotonously minimized under the divergence update rules (Eqs. 3.11-3.13), but the considerable rise in its value over the progress of the iteration is predominantly owed to decreases in the number of components.

At the last few iteration steps, which were run without curve smoothing, the divergence as well as the residual error show large jumps. This indicates

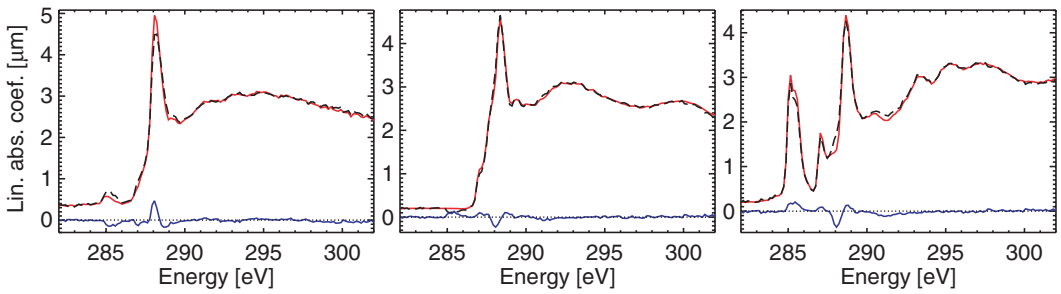

Figure 3.3: Results from the "letters" test data set calculated with the divergence cost function. Shown are the the original spectra (collagen, leucine, tyrosine) as solid red lines. The reconstituted spectra are shown as dashed lines. The differences are plotted in blue at the bottom.

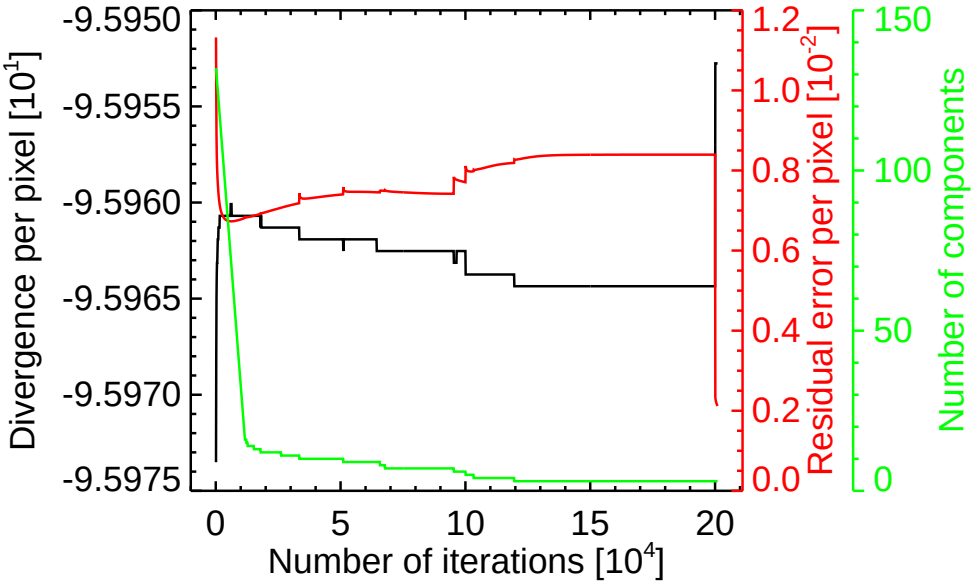

Figure 3.4: Progress of the "letters" test data set calculated with the divergence cost function. Shown are the divergence (black), the residual error (red) and the number of components (green) versus the number of iterations. One can see how the divergence drops while the number of components gets reduced. For a constant number of components the divergence should be monotonously increasing. There are large jumps in the divergence and residual error for the last few iterations, where curve smoothing was relaxed.

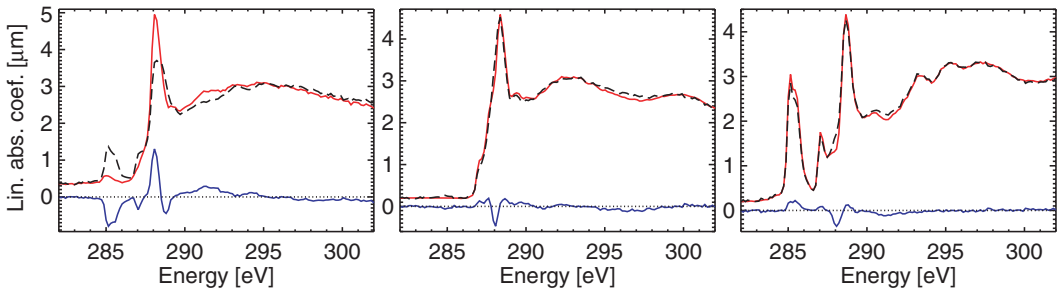

Figure 3.5: Results from the "letters" test data set calculated for the Euclidean distance cost function. Shown are the original spectra (collagen, leucine, tyrosine) as solid red lines. The reconstituted spectra are shown as dashed lines. The differences are plotted in blue at the bottom.

that curve smoothing is counterproductive in a purely mathematical sense. Nevertheless our experience shows that smoothing plays an integral part in finding meaningful results.

Fig. 3.5 shows the reconstruction results for the Euclidean distance cost function. The results for the letter test data set are inferior to the divergence related cost function previously discussed. In particular, the peak heights in the collagen spectrum are considerably off.

The more complex second simulated data set showed somewhat different results. For the divergence cost function all conventional approaches did not lead to satisfying results. A reconstruction of the same simulated data set without photon noise added however was successful (Fig. 3.6). Using all three original

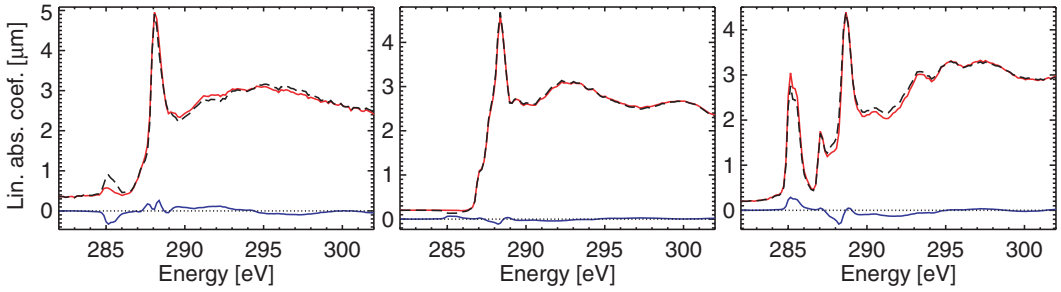

Figure 3.6: Results from the "cell" test data set without photon noise added for the divergence cost function. Shown are the original spectra (collagen, leucine, tyrosine) as solid red lines. The reconstituted spectra are shown as dashed lines. The differences are shown in blue at the bottom.

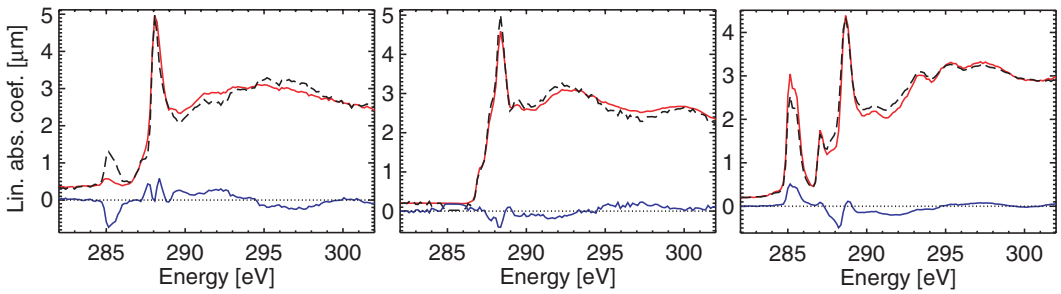

Figure 3.7: Results from the "cell" test data set with the Euclidean distance measure update rules. Shown are the original spectra (collagen, leucine, tyrosine) as solid red lines. The reconstituted spectra are shown as dashed lines. The differences are shown in blue at the bottom.

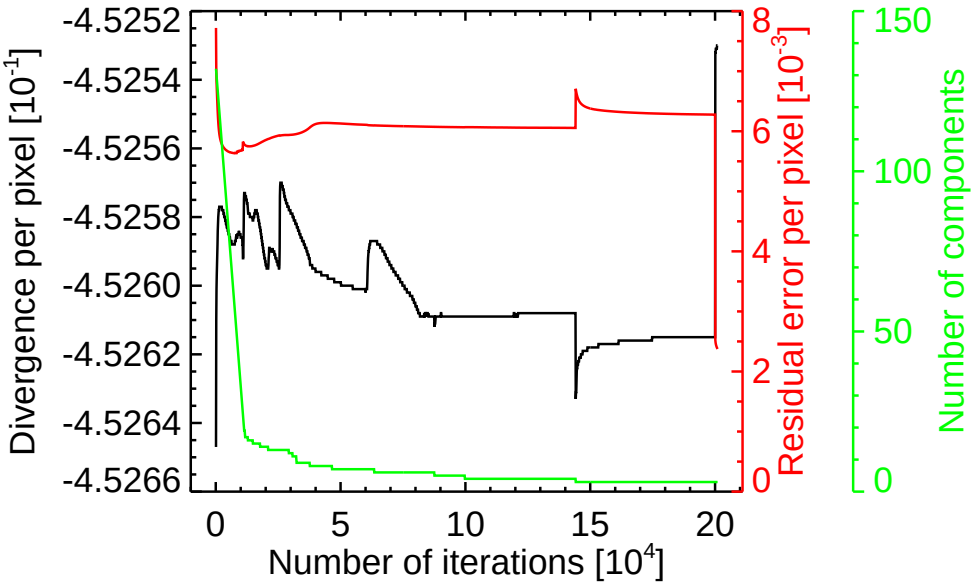

Figure 3.8: Progress of the "cell" test data set with the Euclidean distance measure update rules. Shown are the divergence (black), the residual error (red) and the number of components (green) versus the number of iterations. One can see how the residual error rises while the number of components gets reduced. For a constant number of components the Euclidean distance should be monotonously increasing. For the last few iterations without curve smoothing there are large jumps in the divergence and residual error.

spectra as targets for factorizing the noisy data set, the algorithm worked in finding the pertaining thickness maps. But in this case one can employ Eq. 3.6 and get the same result much faster. Using only a subset of the three spectra as targets did not lead to convincing results either.

On the other hand the algorithm for the Euclidean distance cost function performed satisfactorily. The reconstructed spectra in Fig. 3.7 can be readily identified as the chemical spectra used for the data simulation. The divergence related calculations were not even able to reduce the number of spectra to a sufficiently small value. Fig. 3.8 again shows the values of divergence, Euclidean distance and number of components over the progress of the NMF calculation.

3.5.2 Experimental data sets

The spectra of the wood data set have been scaled to match the reference spectra (the normalization in the NMF algorithm was arbitrary) and offset to match the reference spectra in the carbon pre-edge region. The latter step was to compensate for a possibly different non-carbon content in the reference sample. Fig. 3.9 shows spectra and thickness maps of the 4 components which can be identified as wood, embedding medium (LR White Resin), lignin and cellulose. The differences (solid blue line) between the reference spectra taken from pure components (solid red line) and the results from the NMF calculation (dashed line) are small enough to confidently label the components. Fig. 3.10 shows spectra found by cluster analysis and thickness maps calculated from this set of spectra via singular value decomposition (SVD). Spectra (C) and (D) mainly differ in their amplitudes. Cluster analysis was only able to separate the superpositions and not the individual spectra they consist of. Shown in red on the maps are regions of negative thickness. This is a shortcoming of the SVD method and indicates that the set of cluster spectra is not an entirely correct representation of all the spectra present in the original data set.

Because the *Stardust* particles had been embedded in epoxy for sectioning, all of the spectra found via cluster analysis were dominated by the epoxy spectrum (see Fig. 3.11). One approach to finding spectra from the actual *Stardust* particle was to subtract the epoxy optical density from individual cluster spectra. This highly supervised method is described for example by Cody et al. [52]. Fig. 3.12 shows a comparison of results from this method with

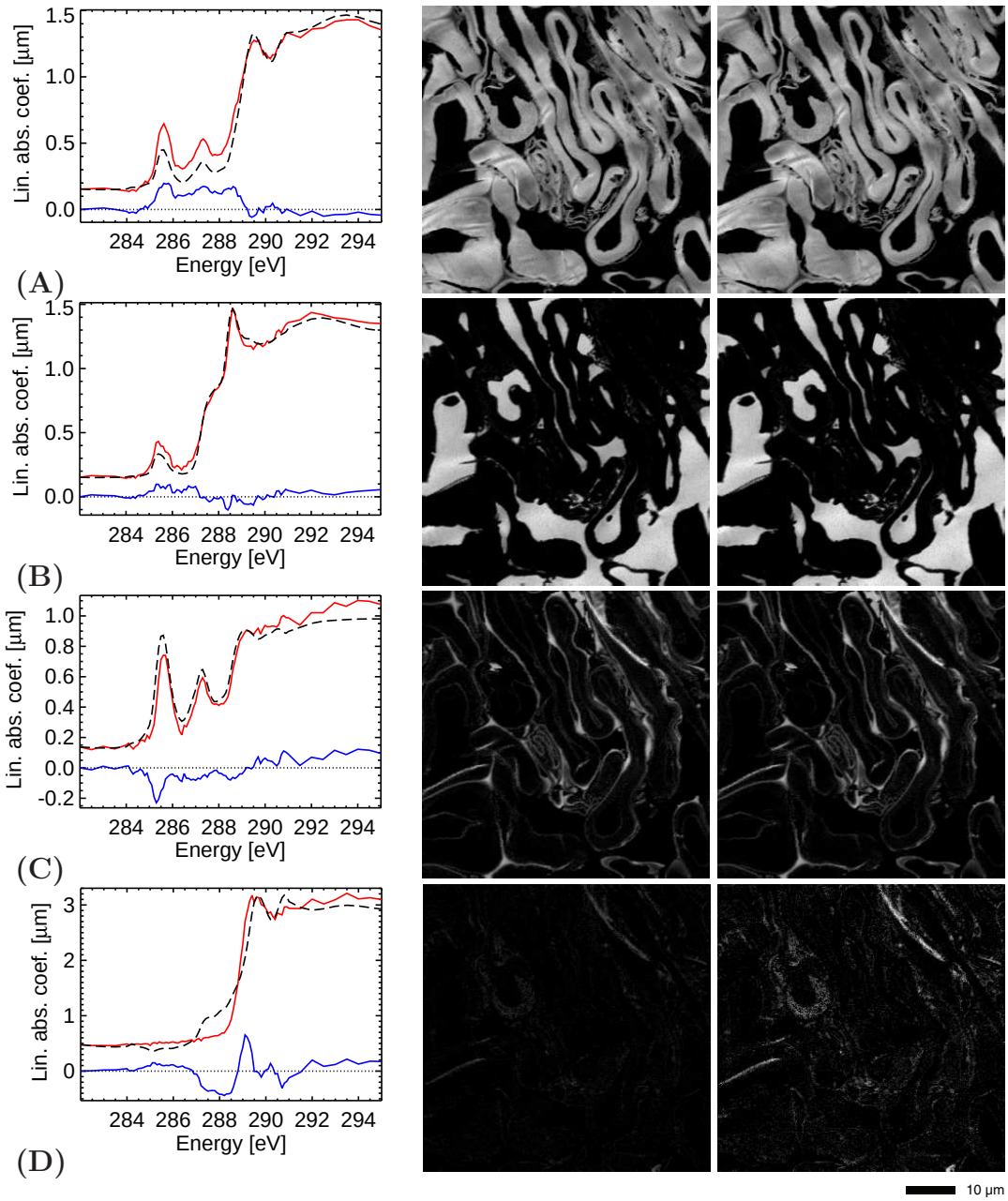

Figure 3.9: Spectra and thickness maps of the wood data set. Shown on the right are the thickness maps and on the left the reference spectra (solid red), spectra found by NMF (dashed) and the difference of the two (solid blue) of (A) wood, (B) LR White Resin, (C) lignin and (D) cellulose. The maps on the left are scaled to the overall thickness, while the maps on the right are scaled to their individual thicknesses.

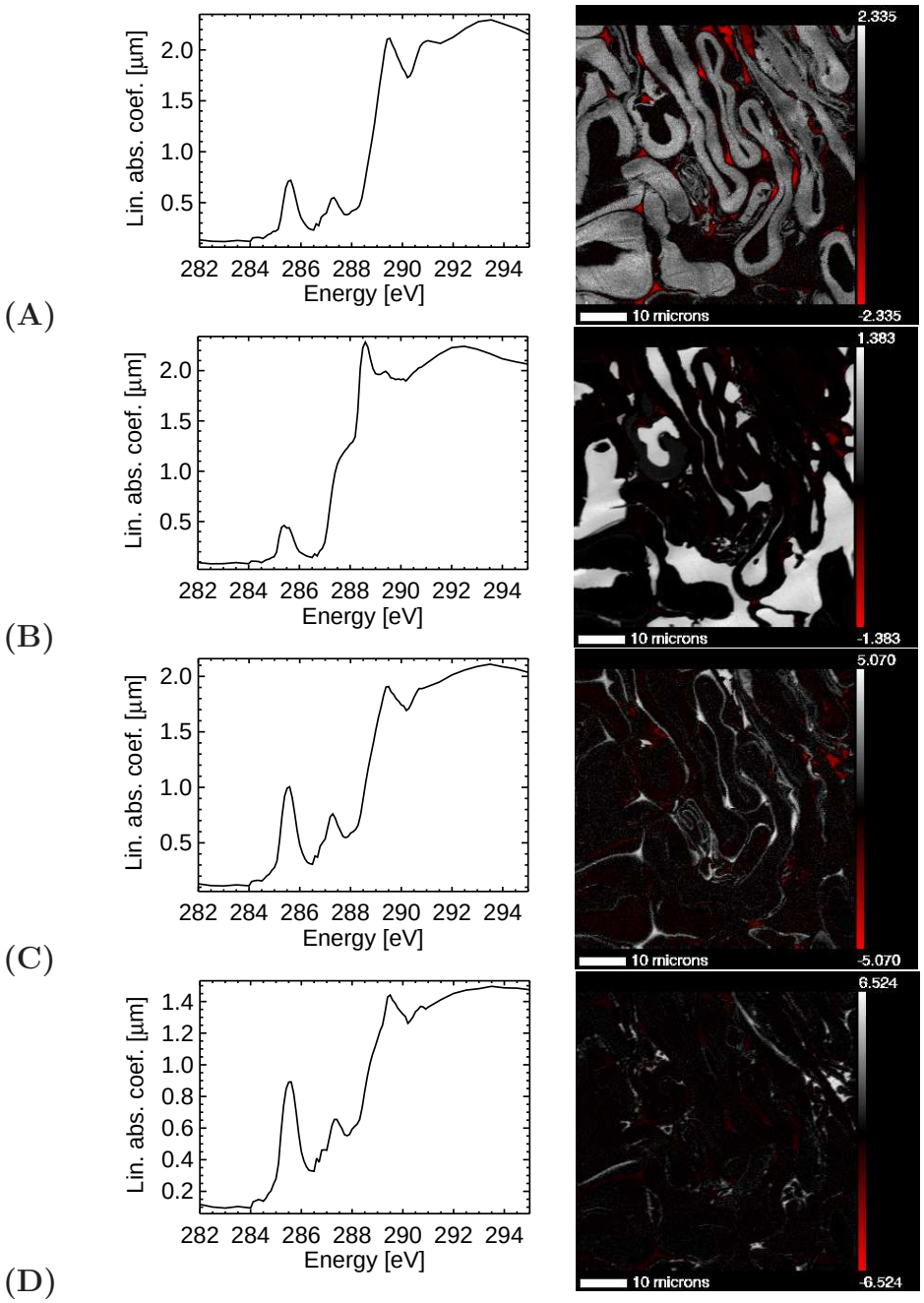

Figure 3.10: Cluster spectra and thickness maps of the wood data set. Shown on the left are the spectra found by cluster analysis and on the right the thickness maps found from these spectra by singular value decomposition. The existence of regions with negative thickness (shown in red) indicates that the set of cluster spectra does not fully match all spectra present in the data.

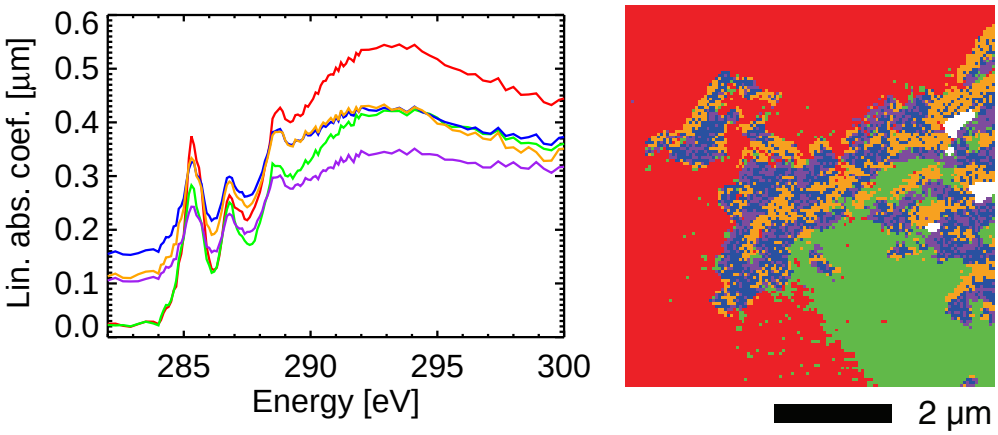

Figure 3.11: Resulting spectra and map from a cluster analysis of the first *Stardust* sample.

results from an NMF calculation. The spectra were adjusted and plotted in the same fashion as for the wood sample. The epoxy component is the thickest by far and closely matches a point spectrum acquired from pure epoxy, while the other two spectra shown have quite similar features to the spectra from epoxy-subtraction. In NMF we were able to find them in an unsupervised fashion without using the knowledge of epoxy present in the sample. It is worth noting that the peak between 285 and 286 eV that was over expressed in the NMF spectrum of (C) is under expressed comparably in (B).

Cluster analysis of the second *Stardust* particle showed results that are mainly variations of epoxy spectra as well (Fig. 3.13). But a movie of optical densities at different energies - when inspecting it carefully - showed a small sample area lighting up between 290 and 291 eV. Is there carbonate in the sample? The cluster results did not reveal anything in that direction. A subsequent NMF calculation was more sucessfull. Fig. 3.14 shows two of the components found by NMF. The first one (A) is can be identified as epoxy (the reference spectrum is overplotted in red), while the second one clearly shows the carbonate absorption peak at 290.4 eV. The overall thickness of the carbonate is thin as shown on the map in the middle. The same map scaled to its individual maximum (on the right) shows the respective area much better.

Not all components found by NMF in this example could be readily identified, but we can say with confidence that a very minor component has been successfully sorted out from a strong background.

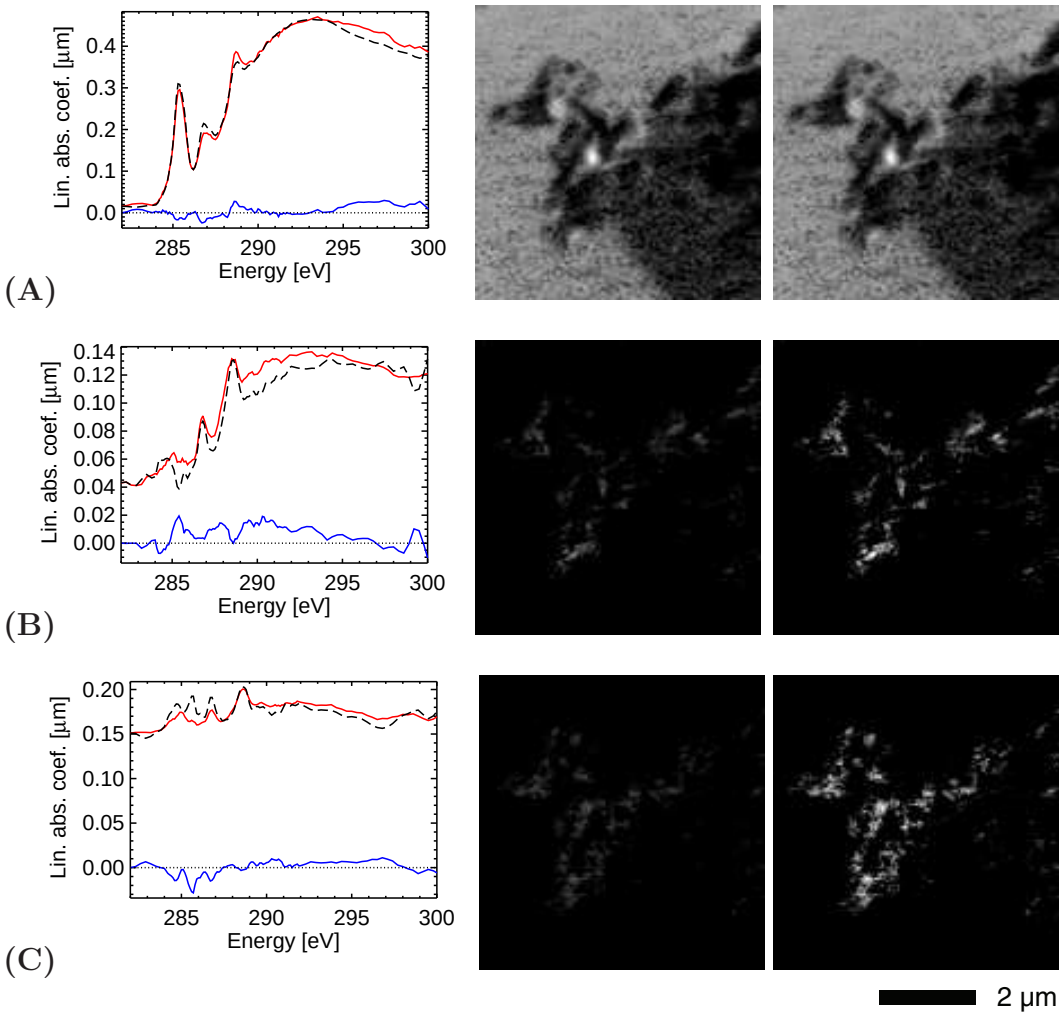

Figure 3.12: Spectra and thickness maps of the first *Stardust* data set. Shown on the right are the thickness maps and on the left the reference spectra (solid red), spectra found by NMF (dashed) and the difference of the two (solid blue) of (A) epoxy and (B) and (C) two other components similar to spectra found by epoxy subtraction from cluster spectra. The maps on the left are scaled to the overall thickness, while the maps on the right are scaled to their individual thicknesses.

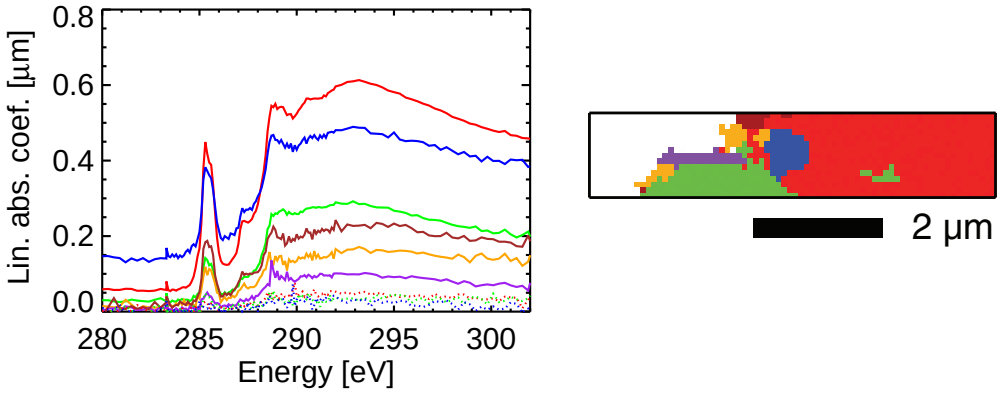

Figure 3.13: Resulting spectra and map from a cluster analysis of the second *Stardust* sample. Clusters corresponding to the dashed spectra at the bottom have been merged into the background.

Liquid water is needed to form carbonates. Therefore the presence of carbonates in comets is unexpected, because comets are believed to have formed in the cold, outer regions of the Solar System, where no liquid water exists. There are at least three possible explanations how carbonate could be found in a sample from *81P/Wild 2*:

1. Impact events can create liquid water even in the outer regions of the Solar System.

2. There is evidence that carbonate can be formed during non-equilibrium condensation of a silicate gas in a H_2O-CO_2-rich water vapor in circumstellar environments like the Solar Nebula [53].

3. The carbonates are of terrestrial origin and a contaminant in the sample.

3.5.3 Timing

The code for this work has been written in the Interactive Data Language (IDL), which has highly optimized array handling capabilities. Nevertheless the computations involved in this work are time consuming. We did a series of test calculations on a system with an AMD Athlon MP 2000+ Processor (1.67 GHz) and sufficient RAM (3 GB). One iteration for a relatively large

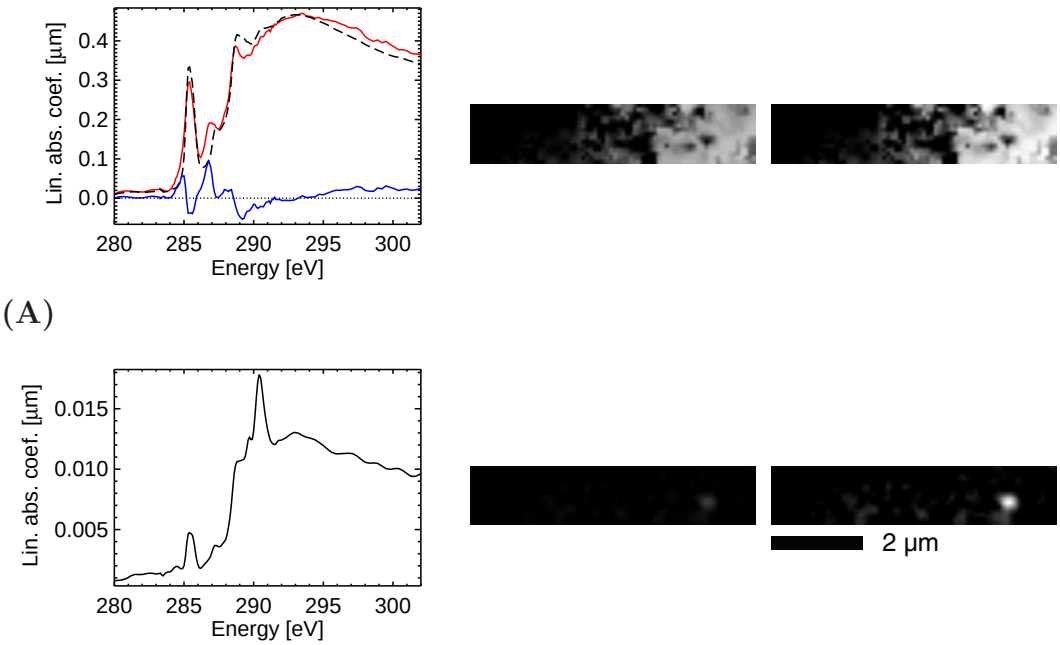

Figure 3.14: Spectra and thickness maps of the second *Stardust* data set. The spectra on the left show (A) a reference spectrum for pure epoxy (solid red), the corresponding spectrum found by NMF (dashed) and the difference of the two (solid blue), (B) a spectrum found by NMF clearly including a carbonate peak at 290.4 eV. Shown in the middle are the corresponding thickness maps scaled to the overall thickness and on the right scaled to their individual thicknesses. The carbonate was not found by cluster analysis (compare Fig. 3.13).

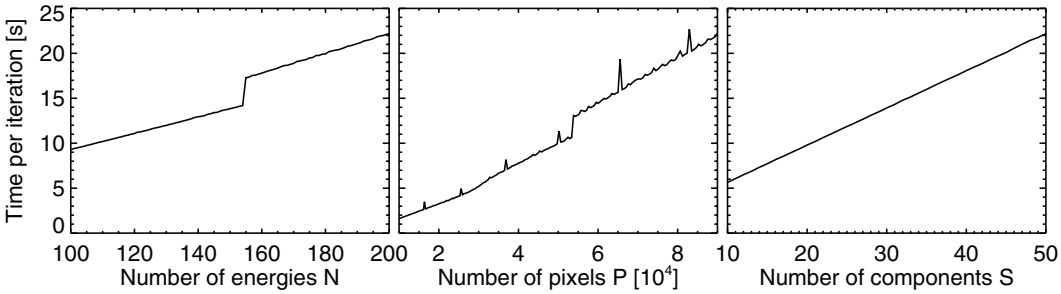

Figure 3.15: Timing of NMF iterations. Shown is the time one entire iteration takes depending on the sizes of the matrices involved. While one of the three parameters involved where increased as shown, the other two were kept at their maximum: $N = 200$, $P = 300^2$ and $S = 50$

data set of $N = 200$ (number of energies), $P = 300^2$ (number of pixels) and $S = 50$ (number of components) took a little over 22 seconds. Computing times were found to be roughly linear in N,P and S, with one iteration for $N = 100$, $P = 100^2$ and $S = 10$ taking about 0.2 seconds.

The timing curves in Fig. 3.15 show two deviations from a strictly linear increase: single steps in the plots for N and P and some fluctuations and spikes in the plot for P. The steps occur from $N = 154$ to $N = 155$ and $P = 231^2$ to $P = 232^2$. Calculations for varying N,P and S showed, that the steps are at points where the products $N \cdot P$ are about constant (but not exaclty, since an iteration contains more steps, than plain matrix multiplications). A change in S never showed any jumps in computing time. This is probably owed to the fact that S is typically small compared to N and especially P. Reducing the amount of RAM from 3 GB to 2 GB did not show any noticable changes either in the position of jumps or the overall computing time. This could be expected, since the total amount of memory needed for an iteration is well below 1 GB. We were satisfied with being able to roughly estimate computation times and did not investigate their peculiarities any further.

Assuming a linear decrease from $S = 50$ to $S = 10$ components (see Fig 3.15) over the course of 10^5 iterations for the relatively large data set of $N = 200$ engeries and $P = 300^2$ pixels, the entire computation time would be over 16 days. To make NMF a standard tool it would require a considerable increase in the computation speed, ideally using parallelized code running on a cluster of multiple nodes with faster computer processors.

3.6 Conclusion

Comparing the results from two different simulated data sets and cost functions it appears the quality of the results justify which cost function to use. The same cost function does not perform equally well on any data set. For the divergence related cost function, noise seems to pose a problem for calculations only if there are considerable variations in component and/or sample thicknesses. NMF may thus be used to find the unknown components in homogeneous solutions or samples of similar kind. This has been demonstrated on a data set from embedded wood fibres. For more complex specimens like cells or *Stardust* particles which contained both mineral and carbonaceous compounds, the Euclidean distance cost function appears to yield better results. We have been able to find features that were not picked up by other analyis methods, but NMF was not able to successfully factorize arbitrarily complex data sets, so there is still room for further advances.

Chapter 4

Studies of Human Sperm

4.1 Introduction

The cleanliness of x-ray absorption spectra compares quite favorably to that of electron energy loss spectroscopy (EELS). Most electron microscopes have an energy resolution of 0.5-0.7 eV leading to blurring of near-edge spectral features (eventhough systems with higher resolution are under development). However, scanning x-ray microscopes like the ones used for our work commonly operate with monochromators of 0.1 eV or better energy resolution. This higher energy resolution as well as the near-complete absence of plural inelastic scattering of x-rays leads to higher sensitivity of spectral fine-structures. Therefore XANES spectroscopy (see Sec. 1.2) has become a common tool in the analysis of biomaterials [33, 54, 55].

Also the ideal specimen thickness for spectroscopy in scanning transmission electron microscopes (STEM) - with typically 80-200 keV electron energy - is less than 100 nm. The transmission of soft x-rays through biomaterials however is strong enough to study whole cells of a few microns size. At x-ray energies in the so-called "water window" between the absorption edges of carbon (290 eV) and oxygen (540 eV) organic materials have a strong absorption contrast relative to ice or water. When imaging hydrated biological specimens of more than about 1 μm thickness at a specific resolution soft x-rays deliver significantly less radiation dose to the sample than electrons do [56, 57]. Especially for sensitive biological samples it is important to keep radiation damage at a minimum. Photons have been found to be about 500 times more effective than electrons in providing near-edge signal around the carbon K-absorption edge [58] for comparable damage created. Cryo-freezing at liquid nitrogen temperatures does little to prevent the breaking of chemical bonds by x-rays, but stabilizes samples and can reduce mass loss to a minimum [59].

Biological cells consist of a whole range of micro-environments from the interior of macromolecules to membrane enclosed regions like organelles, the nucleus or the cytoplasm. This complex organization makes a quantitative, biochemical analysis very demanding. While flow cytometry can reveal the characteristics of individual cells, it does not provide any information on their spatial distribution. A few predefined biomolecules can be located in a cell with high detail for example by the use of immunogold labels, but the biochemical organization in cells, for which specific molecular labels cannot be used, is still not well known.

X-ray microscopy has already been used for a series of sperm studies in the past

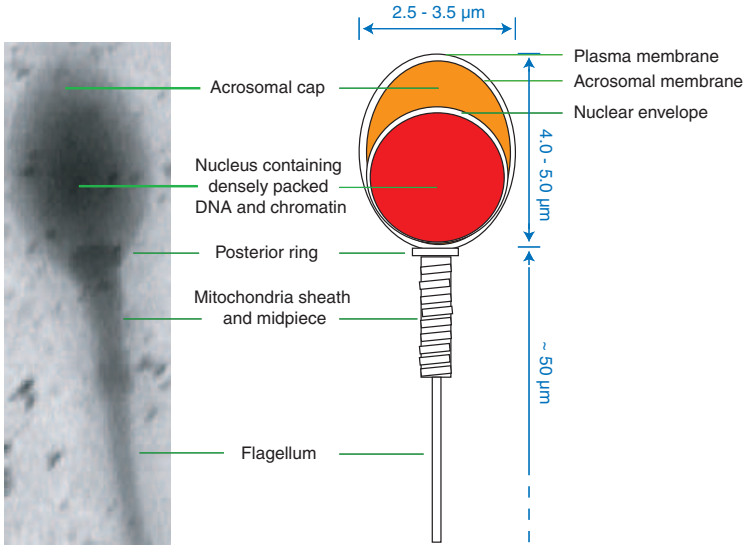

Figure 4.1: Diagram of a human sperm. An x-ray image of a real sperm is shown in comparison.

[60–62]. Combined with spectroscopy it allows one to study the biochemical organization in whole hydrated or dehydrated cells without the used of labels, stains or fixatives. In a collaboration with Yefim Sheynkin, M.D., of the Urology department at Stony Brook University Hospital we used the STXMs at the NSLS to study human sperm. In previous STXM studies of sperm their protein and DNA content had to be estimated using the spectrum of pure bovine serum albumin as a representative protein, as well as the specrum of calf thymus DNA [40]. While this led to biologically useful information on the role of protamine 1 and 2 in the DNA packing in sperm, we wished to see what we could learn without any simplifying a priori assumptions. With new data analysis techniques like PCA [25, 26] and clustering [28, 29] (see Sec. 3.3) we were trying to find correlations between the structural and biochemical organization of the human sperm head one the one side and its conventional morphology and the effect on fertilization on the other.

4.2 Human sperm

Fig. 4.1 shows a schematic diagram of a normal sperm and in comparison an x-ray image of a real sperm. The head should be of oval shape 4.0-5.0 μm long and 2.5-3.5 μm wide (ratio 1.50-1.75) and contain a well defined acrosomal

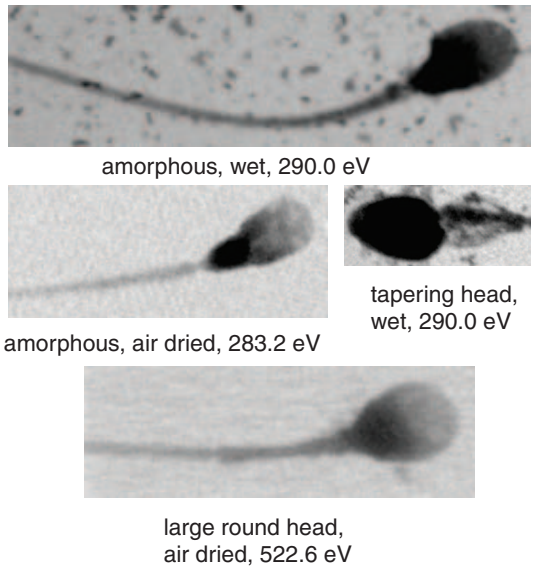

Figure 4.2: X-ray images of sperm with abnormal morphologies.

cap comprising 40-70% of the head area. It is contains enzymes to digest the extracellular matrix of the egg in sperm-oocyte interaction. The acrosomal region can contain membrane bounded vesicles, so-called "vacuoles". The midpiece should be attached axially to the head and about 1.5 times as long with a width of less than 1 μm. The tail after the midpiece should be thinner, about 45 um long and straight.

Recent studies have shown that one in four couples experience difficulties in conceiving [63] with a male factor contributing in more than 50% of these cases [64]. Perhaps 50% of infertile men have either undergone medical or surgical therapy without success or are not even candidates for it. The success rates of assisted reproductive technologies (ARTs) have so far been modest. Even in vitro fertilization (IVF) with intracytoplasmic sperm injection (ICSI), the most advanced ART, has only a 30-40% per cycle pregnancy rate [65, 66].

The andrological assessment of male infertility relies mostly on conventional criteria of sperm quality like concentration, motility and morphology. (Fig. 4.2 shows a few example images of abnormal morphologies.) Guzick et al. [67] however have shown that while threshold values can be used to classify men as subfertile, of indeterminate fertility or fertile, none of the measures are diagnostic of infertility. This indicates that the sperm of infertile men may have

hidden abnormalities in the composition of their nuclei. DNA damage above a certain threshold appears to impair fertilization and embryo development [68, 69], but little is known about the etiologies of sperm DNA damage and its full impact on human reproduction. New findings in the area of sperm DNA might be beneficial to the evaluation and treatment of male infertility. A possible correlation between DNA quality and sperm morphology for instance might prove as valuable pointer in the selection of sperm for IVF.

The morphology studies are primarily done with light microscopy of fixed or stained sperm. But eventhough there is some correlation between sperm morphology and certain biochemical markers, light microscopy does not deliver valuable information on sperm DNA or chromatin abnormalities. Bulk chemical measurements on the other hand average over many morphologies and are not sensitive to individual spermatozoa. While flow cytometry can correlate sperm morphology with total DNA content [70], scanning transmission x-ray microscopy allows us to examine the internal, biochemical structure of individually selected cells with spatial resolution. The selection can be made based upon morphological types.

4.3 Samples and preparation

The sperm samples were provided to us by the Andrology Lab in Stony Brook University Hospital. They were surplus quantities from the diagnosis of male fertility collected by masturbation. The samples were randomly selected without passing on any information on the individual patient or treatment profile.

The fresh samples were washed in phosphate buffered saline (PBS) to remove the optically thick semen and then either kept wet in a special sample holder for STXM [71] or (in most cases) air-dried on standard electron microscopy grids. Efforts have been made to prepare freeze-dried samples as well. We used a custom built cyro plunger for rapid freezing of the sample in order to prevent the formation of ice crystals. After blotting off excess liquid from the grid, the samples were plunged into a liquid ethane bath and then cryo-transferred into a commercial freeze-drier.[1] At pressures below 10^{-4} mbar the samples were gradually warmed up from liquid nitrogen to room temperature over the course of 8 hours or more. However our attempts in freeze-drying did

[1] Electron Microscopy Sciences model EMS775X

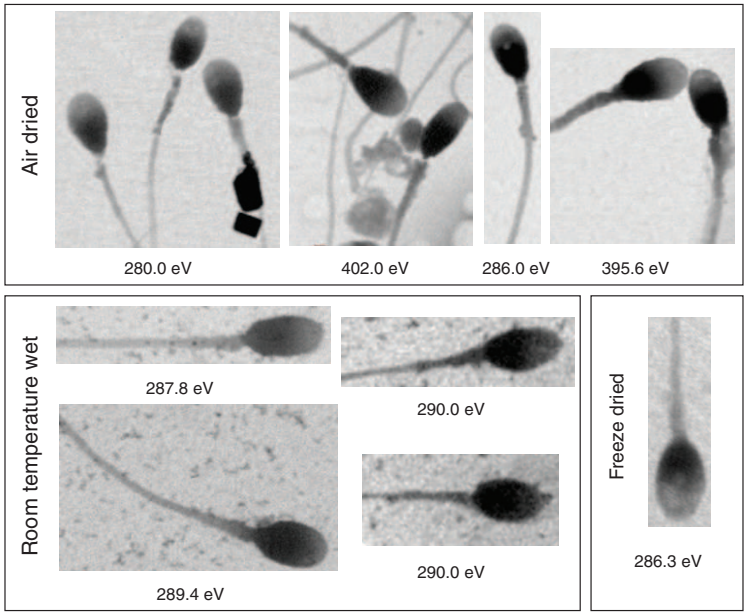

Figure 4.3: X-ray images of human sperm with different preparation methods.

not lead to results superior to those of air-drying. Image results from all three preparation methods can be seen in Fig. 4.3.

A long term goal would be to look at sperm cells frozen-hydrated to keep them as close to their natural environment as possible, while making them less sensitive to radiation damage.

4.4 Analysis results

We collected spectromicroscopic stacks of several individual sperm cells at energies around the K-absorption edges of C, N and O and with spatial resolutions between 40 and 100 nm. The data sets were then analyzed by PCA and cluster analysis to identify areas in the sample with similar biochemical composition. For comparison we also analyzed the sample at the carbon edge with NMF (see Chap. 3). All results shown in this section have been acquired on air-dried specimens.

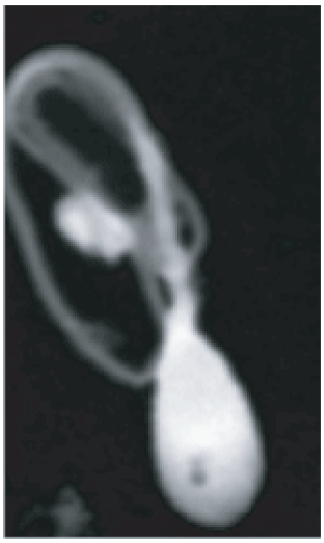

Figure 4.4: Carbon mass distribution.

4.4.1 Carbon edge

Most relevant in biological specimens is the carbon chemistry. Figure 4.4 shows the carbon mass is distribution in a sperm cell.

The result of a cluster analysis of the same data set is shown in Figure 4.5. The color coded image on the left shows four functional regions, as they are separated by the clustering algorithm. The green region in the front of the sperm head represents the enzyme-rich acrosomal cap. The violet region is the actual DNA and histone package to be delivered. The red midpiece with mitochondria is involved in energy production for the sperm motion. The rest of the tail, or flagellum, shown in blue contains mostly lipids. On the right are shown the average spectra of the regions in the same color as the pertaining clusters. For better comparison they are normalized to a value at the high energy end (292eV) and the original values at this energy are shown.

Using the cluster spectra as targets, we can calculate (see Eq. 3.6) thickness maps for each of the components. These maps and cluster spectra are shown in comparison to results by NMF analysis in Figs. 4.6 and 4.7. The cluster spectra are shown in red and the pertaining maps on the very left side, while the dashed NMF spectra go with the remaining maps (scaled to overall thickness on the left and individual thickness in the middle). We can readily identify the components found by NMF as (A) flagellum, (B) DNA package

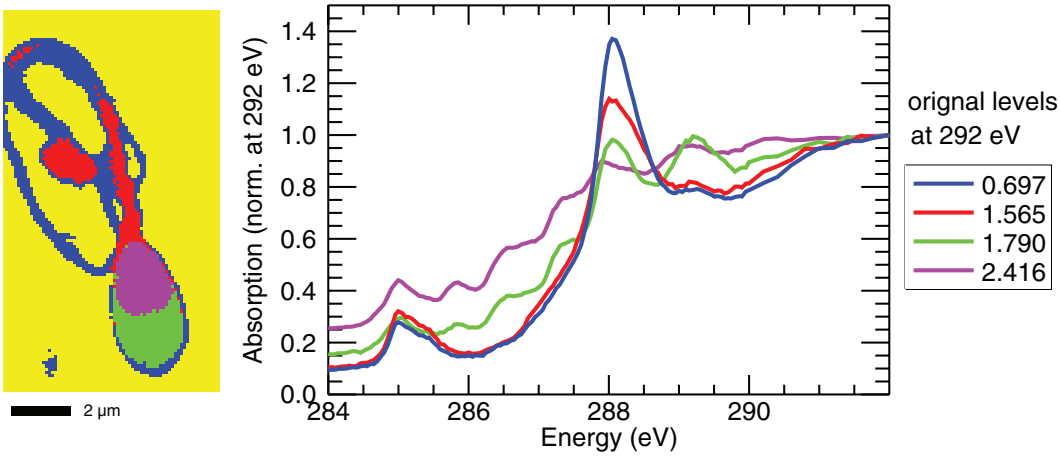

Figure 4.5: Sperm clusters and their average spectra at the carbon edge. The clustering algorithm is able to separate four functional regions (left): the enzyme-rich acrosomal region (green), the DNA package (violet), the midpiece with mitochondria (red) and the flagellum consisting mostly of lipids (blue). The average spectra of each cluster (right) have been normalized at 292 eV.

and (C) acrosomal cap. However two NMF components have been found close to the cluster of the midpiece region. Component (D) is thickest in the very neck region with mitochondria and its spectrum lacks the prominent peak at 288 eV. The spectrum of component (E) is closer to the cluster spectrum in the area around 288 eV and the spatial distribution of this component is not concentrated as much in the neck area. It appears to be intermediate between components (D) and (A).

The areas of negative thickness (red) in the cluster maps indicate, that the cluster spectra do not perfectly represent all chemical signatures in the sample.

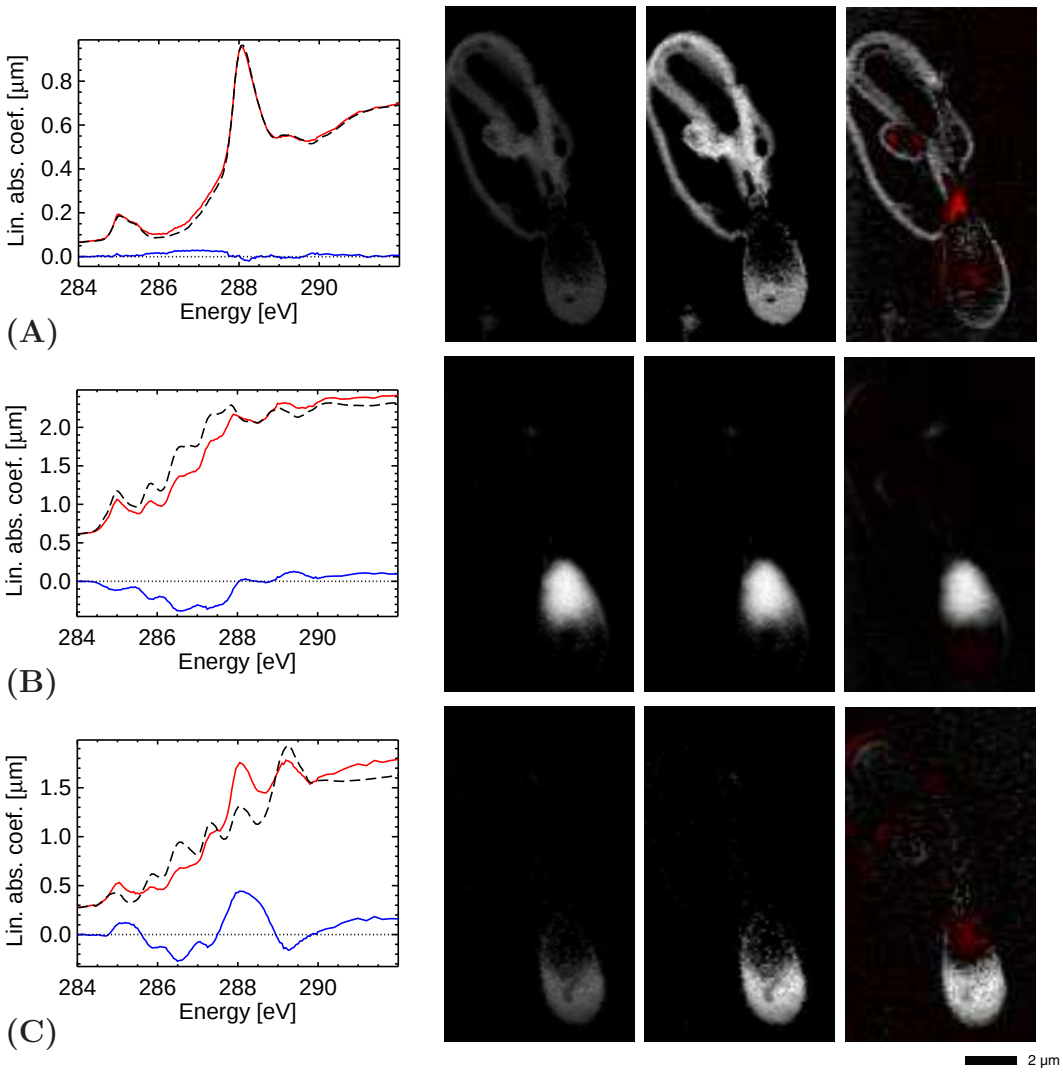

Figure 4.6: Sperm at the carbon edge, NMF and clustering results in comparison. Shown on the left are spectra found by NMF (dashed), spectra found by clustering (solid red) and the difference of the two (solid blue). The cluster spectra are the same as identified in Fig. 4.5. Shown on the right are three thickness maps for each spectrum. The left-most are NMF maps scaled to the overall thickness, while the maps in the middle are scaled to their individual thicknesses. The right most maps show thicknesses calculated from the cluster spectra (red indicating negative thickness). The components can be identified as (A) flagellum, (B) DNA package and (C) acrosomal cap. (continued by Fig 4.7)

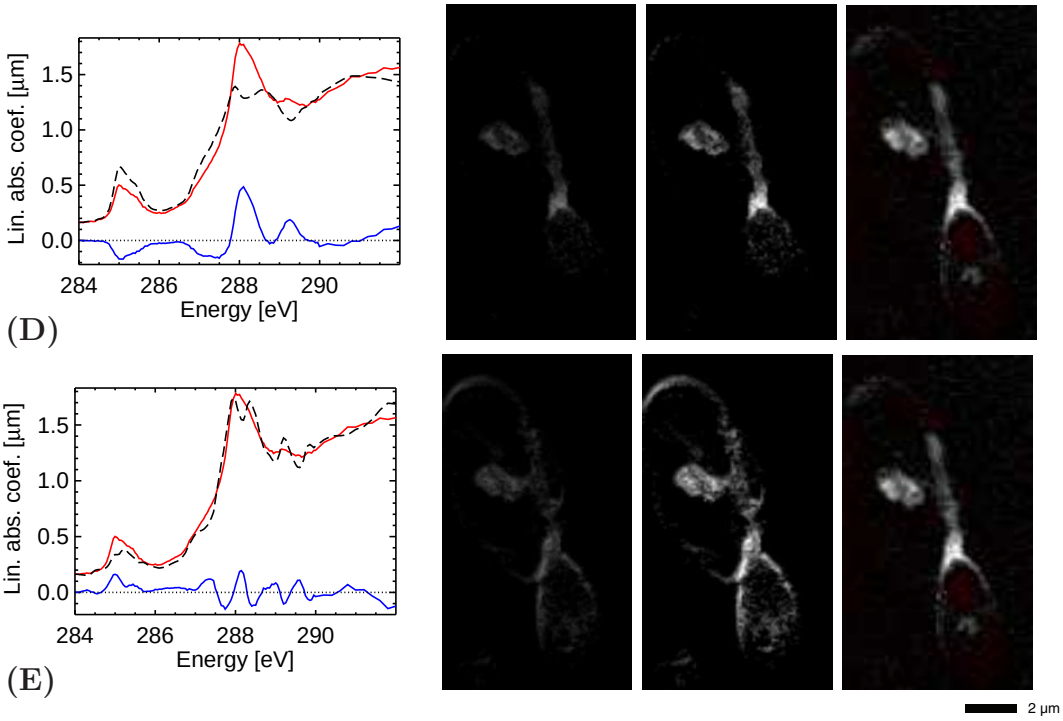

Figure 4.7: Sperm at the carbon edge, NMF and clustering results in comparison (continued from Fig 4.6). Shown here are two different components found by NMF in comparison to the same cluster identified as midpiece. The NMF component (D) is thickest in the very neck region, where the mitochondria are located and its spectrum lacks the prominent peak at 288 eV. Component (E) on the other hand may be more of a mixing between components (D) and (A).

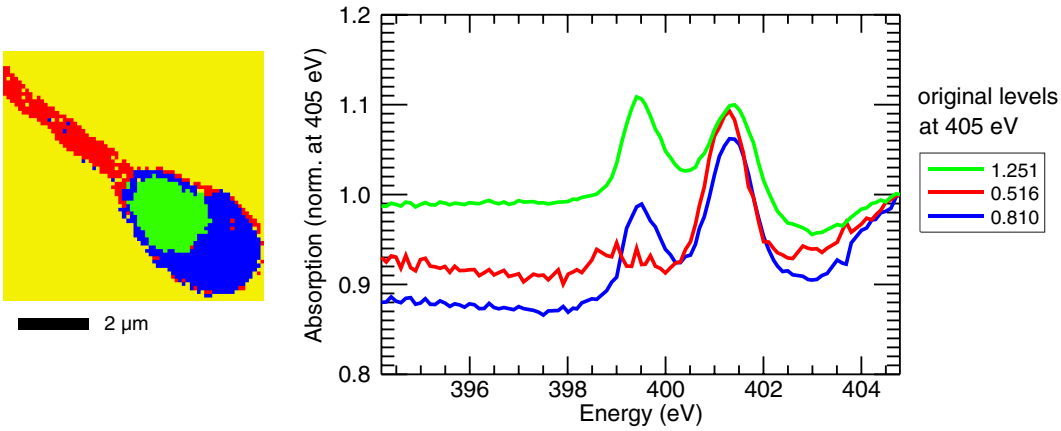

Figure 4.8: Sperm clusters and their average spectra at the nitrogen edge. The clustering result looks similar to the carbon edge results. The average spectra of each cluster have been normalized at 405 eV.

4.4.2 Nitrogen and oxygen edge

Figs. 4.8 and 4.9 show clustering results of sperm cells at nitrogen and oxygen energies, respectively. Even though they were samples from different donors examined at different x-ray energies, we find similar regional distributions by the clustering. The DNA region (green here) can be separated from the the acrosome (blue) and the tail (red) according to their spectral signature. What was not separated out is the flagellar motor region.

The nitrogen edge spectra show a clear difference in the peak at 399.5 eV. It is predominant in the DNA spectrum and hardly noticeable in the midpiece spectrum, while the acrosome spectrum lies in between.

The two peaks in the DNA spectrum around 399.5 eV and 401.5 eV have a comparable separation as the peaks in the DNA spectrum measured for example by Kirtley et al. [54], but are red shifted by about 1.5 eV. This raises the question if the monochromator calibration may have been off at time of the measurement.

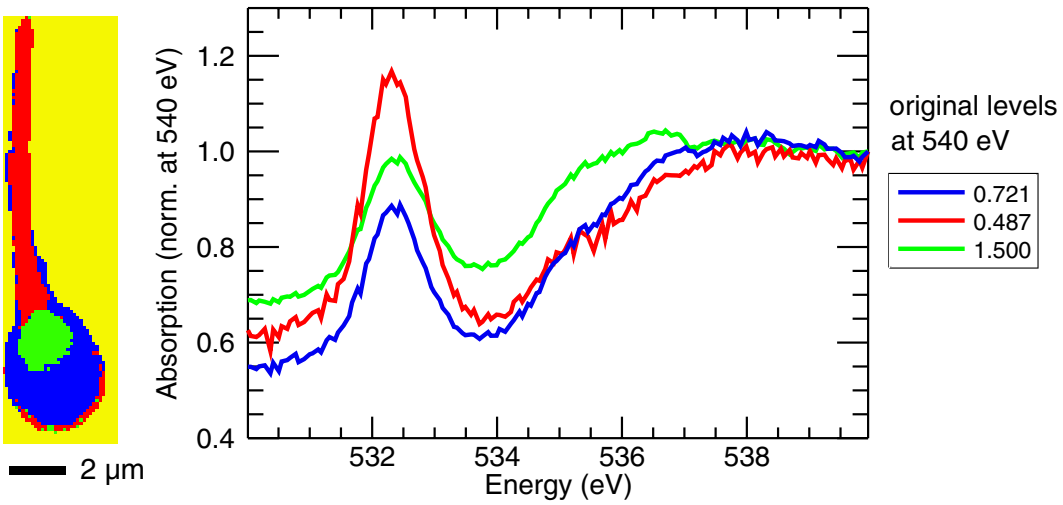

Figure 4.9: Sperm clusters and their average spectra at the oxygen edge. The clustering result looks similar to the carbon and nitrogen edge results. The average spectra of each cluster have been normalized at 540eV.

4.5 Conclusion

Even though the x-ray absorption spectra in human sperm are complex we can get useful information from them. Higher spatial resolution would be helpful for detecting finer substructures. This resolution is currently limited by the focusing optics in x-ray microscopy systems (see Sec. 1.3), but also the thickness of the cells themselves. So besides making efforts towards frozen-hydrated samples for preservation in a cryo microscope, it may also be valuable to look at cryo-microtomed sections to avoid thickness limitations.

Chapter 5

Summary and Outlook

In this thesis we have discussed three parts involved in scanning transmission x-ray microscopy: instrumentation, data analysis and application.

In Chap. 2 we described an upgrade of the NSLS STXM with a laser interferometer and faster electronics. We also explained the new software concept involved and how it is possible to use most microscope functions remotely. The new system is capable of doing certain scans faster and at higher positioning precision. The interferometer feedback ensures long term stability even with mechanical drifts due to temperature changes and imperfections in the hardware of the scanning stages.

In Chap. 3 we described non-negative matrix factorization as a new approach to analyze soft x-ray spectromicroscopy data. We used an iterative algorithm to analyze simulated test data sets as well as data measured from real specimens. We compared some of the results of the factorization with those by an earlier approach using principal component analysis followed by cluster analysis to group image regions according to spectral similarities. While NMF calculations require high computing powers, they can yield valuable information on the chemical composition of unknown specimens in addition to the other techniques described.

In Chap. 4 we finally discussed the application of the STXM instruments and data analysis software to investigate the chemistry of human sperm. We were able to identify the main functional regions in sperm samples without using previously known information or making simplifying assumptions.

While new synchrotrons with brighter x-ray sources are under construction or planning (e.g. PETRA-III and NSLS-II), it will be necessary to further improve the STXM technique to make the best use of the high performance x-ray beams. This includes

- monochromators for higher energy resolution,
- better focusing optics (e.g Fresnel zone plates) to achieve smaller focal spot sizes and high efficiency,
- continued improvements to the scan electronics to allow for dwell times well below the millisecond regime at high positioning precision,
- fast x-ray detectors possibly with capabilities as dark field and differential phase contrast imaging,

- as well as cryo-systems to stabilize specimens to withstand higher radiation doses.

To make the new hardware attractive for users with various scientific backrounds, it is worthwhile to develop software for easy-to-use interfaces. The same goes for analysis software, where there is still room for new and improved techniques providing reliable results in a quick and user friendly manner.

It can certainly be assumed that STXM will keep playing an important role in the world of x-rays, with interesting projects for experienced researchers and developers as well as rookie students.

Appendix A

Proof of NMF Update Rules

A.1 Proof of divergence update rules

We prove here [analogous to [44]], the **Theorem** that the objective function

$$F = \sum_{np} (D_{np} \cdot \ln(\mu t)_{np} - (\mu t)_{np}) \tag{A.1}$$

is non-decreasing under the following update rules:

$$\mu_{ns} \leftarrow \mu_{ns} \sum_{p} \frac{D_{np}}{(\mu t)_{np}} \frac{t_{sp}}{\sum_j t_{sj}} \tag{A.2}$$

and

$$t_{sp} \leftarrow t_{sp} \sum_{n} \frac{\mu_{ns}}{\sum_j \mu_{js}} \frac{D_{np}}{(\mu t)_{np}} \tag{A.3}$$

Definition: $G(\tau, \tau^l)$ is an auxiliary function for $F(\tau)$ if

$$G(\tau, \tau^l) \leq F(\tau) \ , \qquad G(\tau, \tau) = F(\tau) \ . \tag{A.4}$$

Fig. A.1 depicts the role of the auxiliary function in the following lemma.

Lemma 1: Provided that G is an auxiliary function, F is non-decreasing under the update

$$\tau^{l+1} = \arg\max_{\tau} G(\tau, \tau^l) \ . \tag{A.5}$$

Proof: $F(\tau^{l+1}) \geq G(\tau^{l+1}, \tau^l) \geq G(\tau^l, \tau^l) = F(\tau^l)$ □

$F(\tau^{l+1}) = F(\tau^l)$ only if τ^l is a local maximum of $G(\tau, \tau^l)$. In this case $\nabla F(\tau^l) = 0$, if the derivative of F is existing and continuous in a small neighborhood of τ^l. So, an iteration of the update rule in Eq. A.5 lets our estimates sequentially converge to a local maximum $\tau^{\max} = \arg\max_\tau F(\tau)$ of the objective function:

$$F(\tau^{\max}) \geq \ldots F(\tau^{l+1}) \geq F(\tau^l) \ldots \geq F(\tau^2) \geq F(\tau^1) \geq F(\tau^0) \tag{A.6}$$

Lemma 2:

$$G(\tau, \tau^l) = \sum_{ns} d_n \frac{\mu_{ns}\tau_s^l}{\sum_i \mu_{ni}\tau_i^l} \left(\ln \mu_{ns}\tau_s - \ln \frac{\mu_{ns}\tau_s^l}{\sum_i \mu_{ni}\tau_i^l} \right) - \sum_{ns} \mu_{ns}\tau_s \tag{A.7}$$

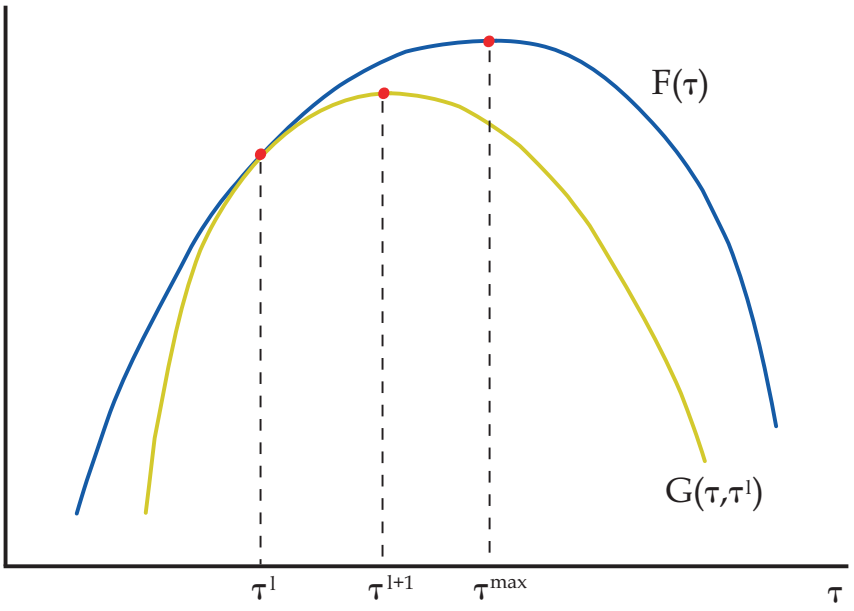

Figure A.1: $F(\tau^{l+1}) \geq F(\tau^l)$: The maximum $\tau^{l+1} = \arg\max_h G(\tau, \tau^l)$ of the auxiliary function $G(\tau, \tau^l) \leq F(\tau)$ is one step closer (or equally close) to the maximum of $F(\tau)$.

is an auxiliary function for

$$F(\tau) = \sum_n d_n \ln \left(\sum_s \mu_{ns} \tau_s \right) - \sum_s \mu_{ns} \tau_s \ . \tag{A.8}$$

We are treating the matrices by columns here. d_n is a column of D_{np} and τ_s is the pertaining column of t_{sp}.

Proof: $G(\tau, \tau) = F(\tau)$ is straightforward. For the proof of $G(\tau, \tau^l) \leq F(\tau)$, the convexity of the ln function gives rise to the following inequalitiy

$$\ln \sum_s \mu_{ns} \tau_s \geq \sum_s \alpha_s \ln \frac{\mu_{ns} \tau_s}{\alpha_s} \tag{A.9}$$

holding for all $\alpha_s \geq 0$ and $\sum_s \alpha_s = 1$. If we choose

$$\alpha_s = \frac{\mu_{ns} \tau_s^l}{\sum_i \mu_{ni} \tau_i^l} \ , \tag{A.10}$$

we get

$$\ln \sum_s \mu_{ns}\tau_s \geq \sum_s \frac{\mu_{ns}\tau_s^l}{\sum_i \mu_{ni}\tau_i^l} \left(\ln \mu_{ns}\tau_s - \ln \frac{\mu_{ns}\tau_s^l}{\sum_i \mu_{ni}\tau_i^l} \right) . \tag{A.11}$$

Using this inequality we can show that $F(\tau) \geq G(\tau, \tau^l)$ □

Proof of Theorem: We can now proof our Theorem by means of Lemma 1. Where its derivative with respect to τ is zero, $G(\tau, \tau^l)$ has a maximum:

$$\frac{dG(\tau, \tau^l)}{d\tau_s} = \sum_n d_n \frac{\mu_{ns}\tau_s^l}{\sum_i \mu_{ni}\tau_i^l} \frac{1}{\tau_s} - \sum_n \mu_{ns} = 0 \tag{A.12}$$

Eq. A.5 can be written as the following update rule:

$$\tau_s^{l+1} = \frac{\tau_s^l}{\sum_n \mu_{ns}} \sum_n \frac{d_n}{\sum_i \mu_{ni}\tau_i^l} \mu_{ns} \tag{A.13}$$

Under this update F in Eq. A.8 is non-decreasing. Changing back from column to matrix form, the update rule is equivalent to Eq. A.3. Analogously the update rule of μ can be shown to be non-decreasing. The roles of t and μ just have to be reversed. □

A.2 Proof of Euclidean distance update rules

We prove here [analogous to [44]], the **Theorem** that the objective function

$$F = \sum_{np} (D_{np} - (\mu t)_{np})^2 \tag{A.14}$$

is non-increasing under the following update rules:

$$\mu_{ns} \leftarrow \mu_{ns} \frac{(Dt^T)_{ns}}{(\mu t t^T)_{ns}} \tag{A.15}$$

and

$$t_{sp} \leftarrow t_{sp} \frac{(\mu^T D)_{sp}}{(\mu^T \mu t)_{sp}} \tag{A.16}$$

The following definition, Lemma 1 and its proof are all analogous to Sec. A.1,

with the difference, that we are looking for a local minimum instead of a local maximum of the auxiliary function.

Definition: $G(\tau, \tau^l)$ is an auxiliary function for $F(\tau)$ if

$$G(\tau, \tau^l) \geq F(\tau) \;, \qquad G(\tau, \tau) = F(\tau) \;. \tag{A.17}$$

Lemma 1: Provided that G is an auxiliary function, F is non-increasing under the update

$$\tau^{l+1} = \arg\min_{\tau} G(\tau, \tau^l) \;. \tag{A.18}$$

Proof: $F(\tau^{l+1}) \leq G(\tau^{l+1}, \tau^l) \leq G(\tau^l, \tau^l) = F(\tau^l)$ □

An iteration of the update rule in Eq. A.18 lets our estimates sequentially converge to a local minimum $\tau^{\min} = \arg\min_\tau F(\tau)$ of the objective function:

$$F(\tau^{\min}) \leq \ldots F(\tau^{l+1}) \leq F(\tau^l) \ldots \leq F(\tau^2) \leq F(\tau^1) \leq F(\tau^0) \tag{A.19}$$

Lemma 2:

$$G(\tau, \tau^l) = F(\tau^l) + (\tau - \tau^l)^T \nabla F(\tau^l) + (\tau - \tau^l)^T K(\tau^l)(\tau - \tau^l) \tag{A.20}$$

with $K(\tau^l)$ being the diagonal matrix

$$K_{si}(\tau^l) = \delta_{si}(\mu^T \mu \tau^l)_s / \tau_s^l \tag{A.21}$$

is an auxiliary function for

$$F(\tau) = \sum_n \left(d_n - \sum_s \mu_{ns} \tau_s \right)^2 \;. \tag{A.22}$$

As in Sec. A.1 we are treating matrices by columns. d_n is a column of D_{np} and τ_s is the pertaining column of t_{sp}.

Proof: It is trivial to verify that $G(\tau, \tau) = F(\tau)$. To show that $G(\tau, \tau^l) \geq F(\tau)$, we compare

$$F(\tau) = F(\tau^l) + (\tau - \tau^l)^T \nabla F(\tau^l) + (\tau - \tau^l)^T (\mu^T \mu)(\tau - \tau^l) \tag{A.23}$$

with Eq. A.20 and reduce $G(\tau, \tau^l) \geq F(\tau)$ to

$$(\tau - \tau^l)^T [K(\tau^l) - \mu^T \mu](\tau - \tau^l) \geq 0 \; . \tag{A.24}$$

We rescale $K - \mu^T \mu$ to prove non-negativity :

$$M_{si}(\tau^l) = \tau_s^l (K(\tau^l) - \mu^T \mu)_{si} \tau_i^l \tag{A.25}$$

Now $K - \mu^T \mu$ is non-negative if and only if M is. We let $\nu = \tau - \tau^l$, and get

$$\begin{aligned}
\nu^T M \nu &= \sum_{si} \nu_s M_{si} \nu_i \\
&= \sum_{si} \nu_s \tau_s^l (K(\tau^l) - \mu^T \mu)_{si} \tau_i^l \nu_i \\
&= \sum_{si} \nu_s \tau_s^l [\delta_{si} - 1](\mu^T \mu)_{si} \tau_i^l \nu_i \\
&= \sum_{si} (\mu^T \mu)_{si} \tau_s^l \tau_i^l \left[\frac{1}{2} \nu_s^2 + \frac{1}{2} \nu_i^2 - \nu_s \nu_i \right] \\
&= \frac{1}{2} \sum_{si} (\mu^T \mu)_{si} \tau_s^l \tau_i^l (\nu_s - \nu_i)^2 \\
&\geq 0 \; .
\end{aligned} \tag{A.26}$$

□

Proof of Theorem: Our Theorem follows from Lemma 1. The minimum of $G(\tau, \tau^l)$ in Eq. A.20 with respect to τ is determined by setting the gradient to zero and the update rule of Eq. A.18 takes the form

$$\tau^{l+1} = \tau^l - \frac{\nabla F(\tau^l)}{2K(\tau^l)} \; . \tag{A.27}$$

Substituting F and K we can simplify the previous equation to

$$\tau_s^{l+1} = \tau_s^l \frac{(\mu^T d)_s}{(\mu^T \mu \tau^l)_s} \; . \tag{A.28}$$

G being an auxiliary function ensures, that F in Eq. A.22 is non-increasing under this update. In matrix form this is the update rule in Eq. A.16. Reverse the roles of t and μ to show analogously that the update rule of μ is non-increasing. □

Appendix B

Electronic Layouts of the Connection Interface Board

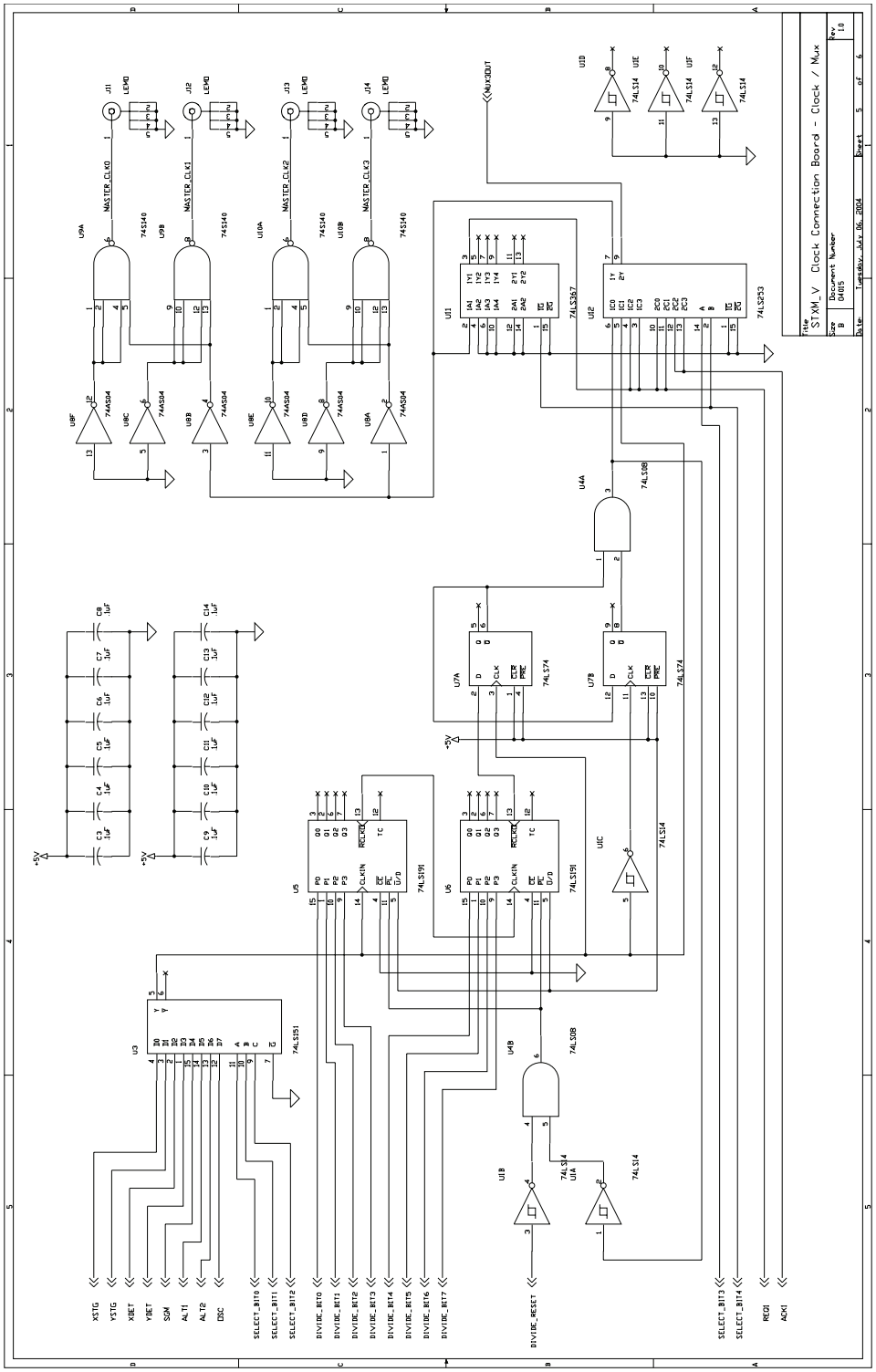

Figure B.1: Layout: Clock divider and multiplexers

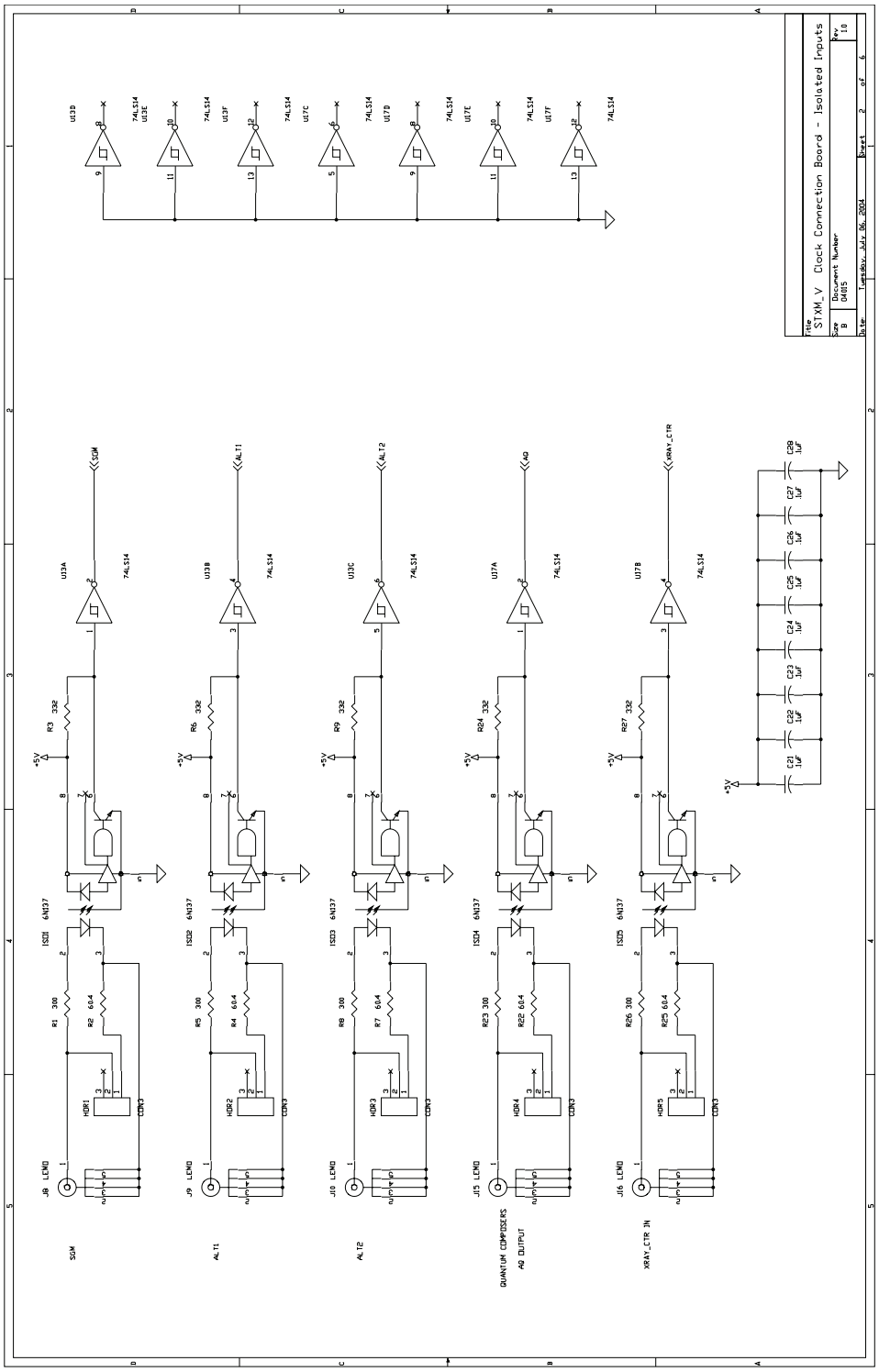

Figure B.2: Layout: Isolated inputs

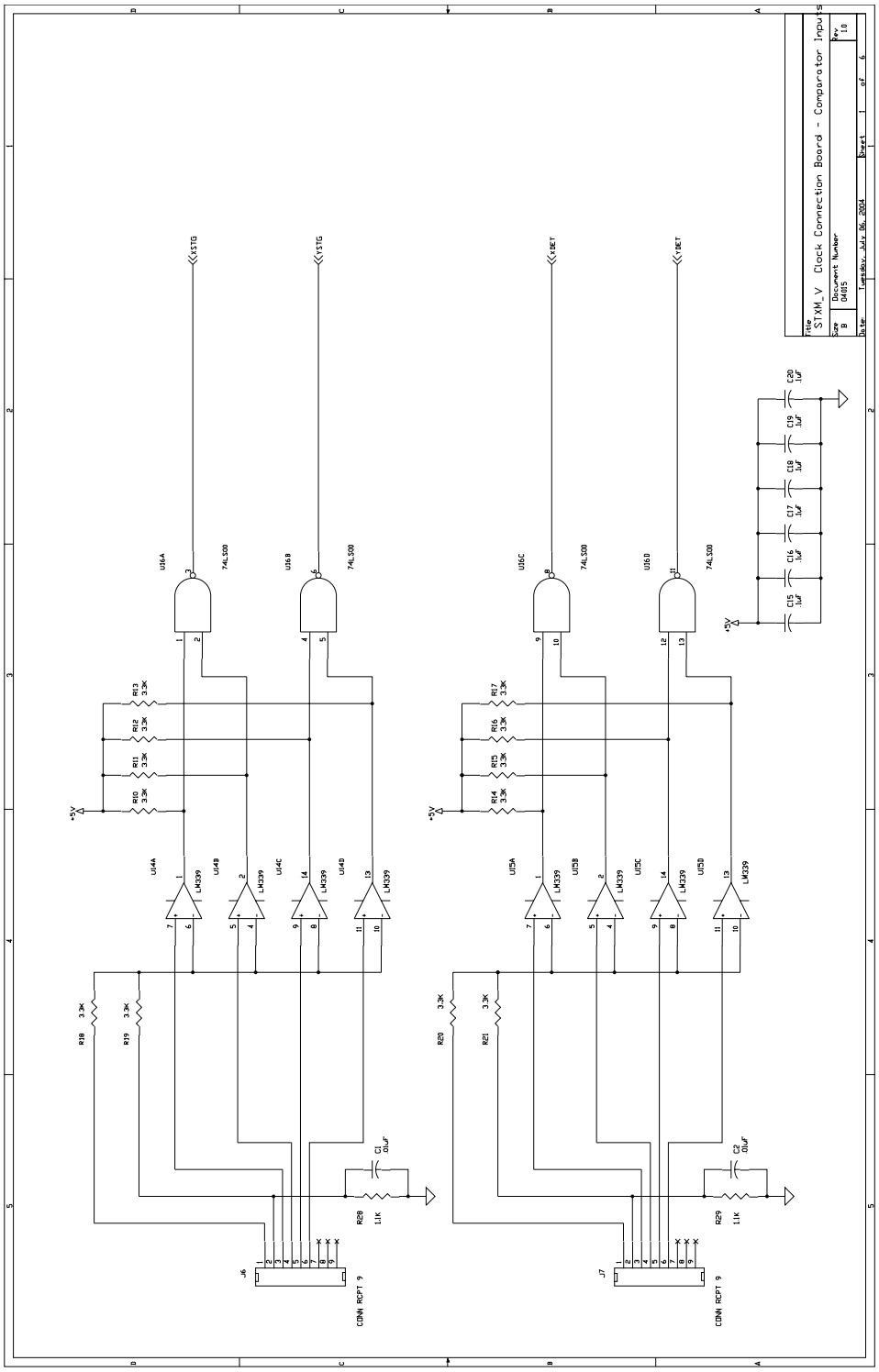

Figure B.3: Layout: Comparator inputs

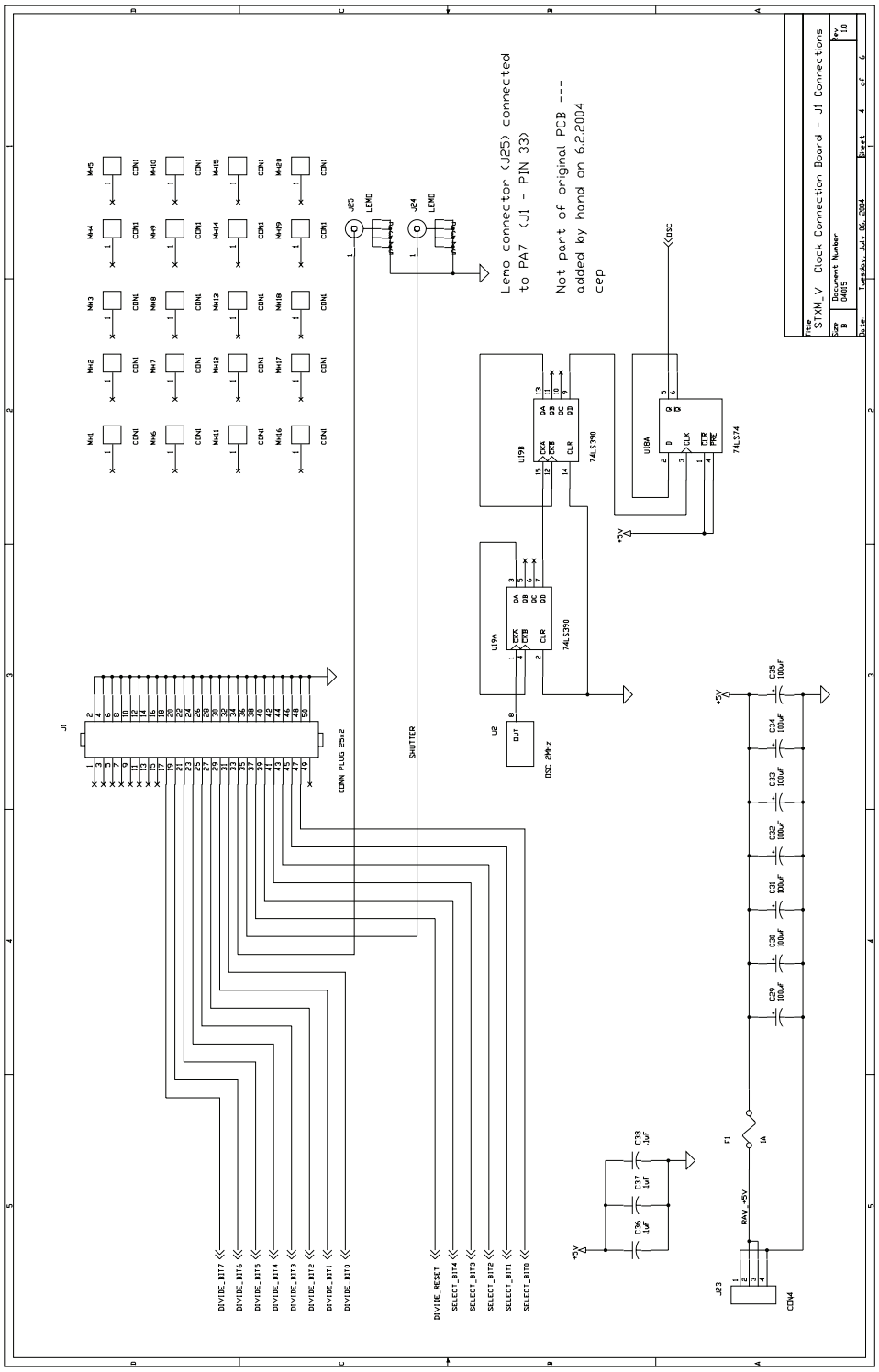

Figure B.4: Layout: J1 connections

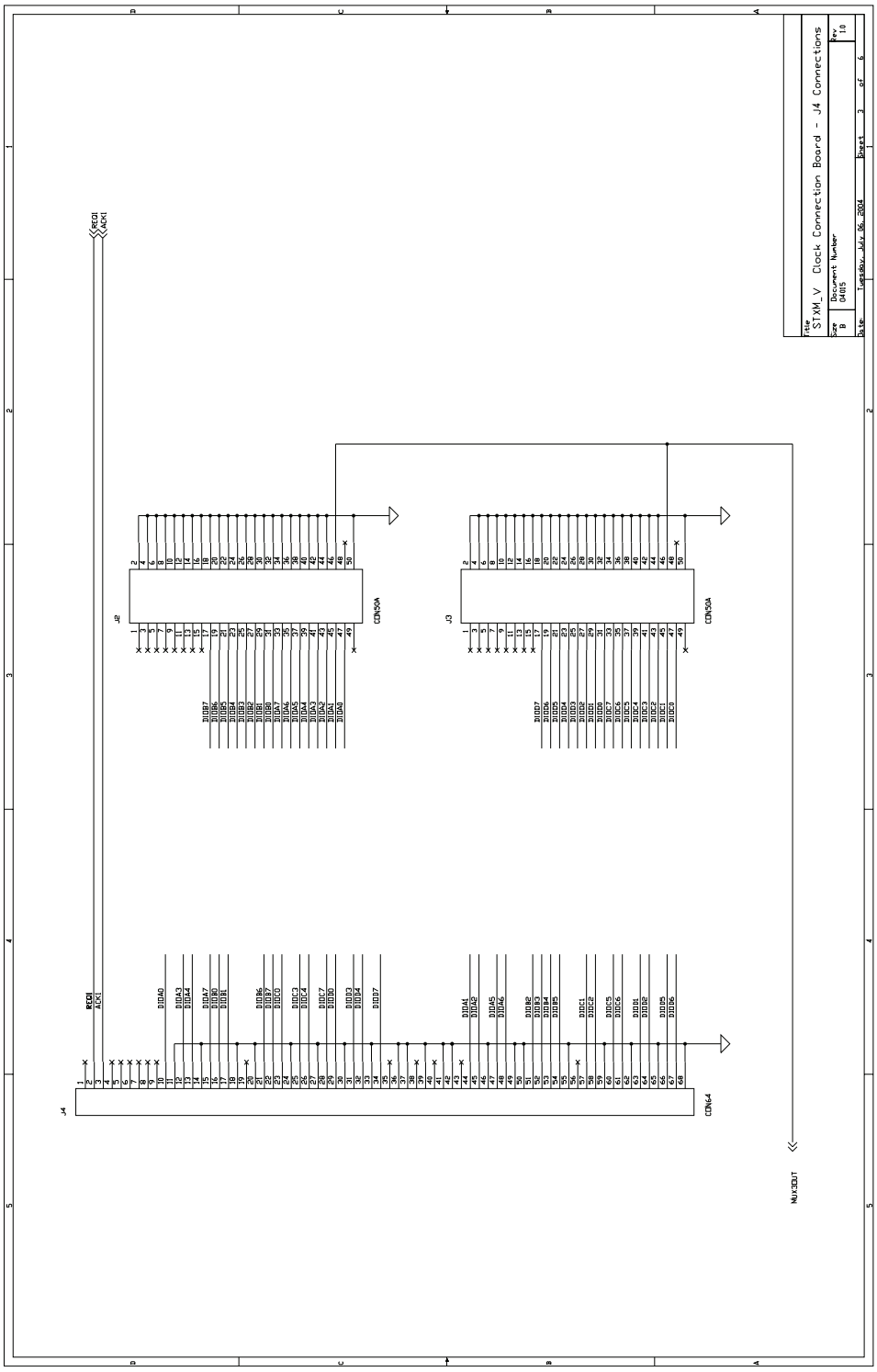

Figure B.5: Layout: J4 connections

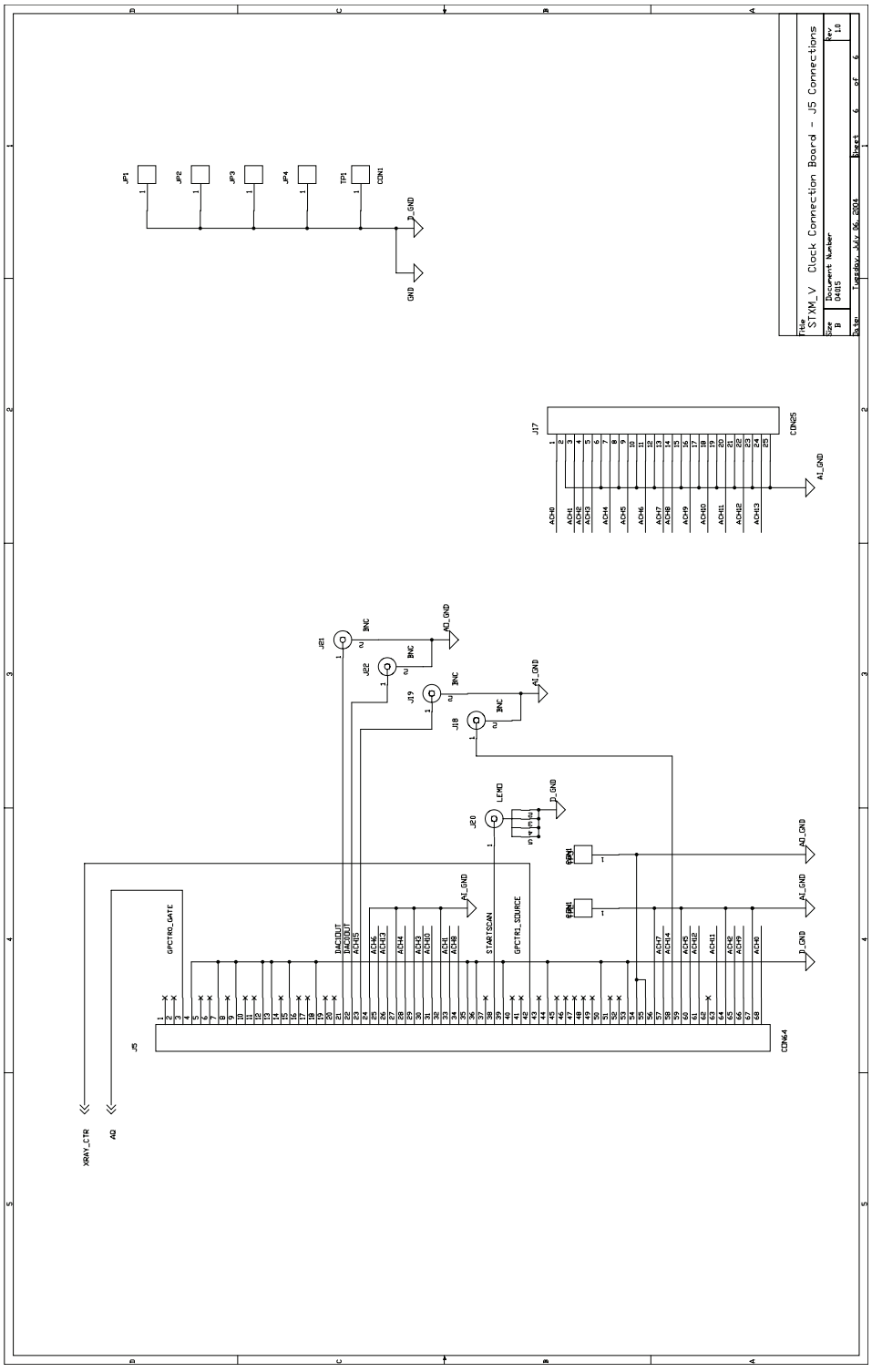

Figure B.6: Layout: J5 connections

Appendix C

Abbreviations and Acronyms

ADC	Analog to Digital Converter
ALS	Advanced Light Source
APS	Advanced Photon Source
ART	Assisted Reproductive Technology
BNL	Brookhaven National Laboratory
CARS	Coherent Anti-Stokes Raman Spectroscopy
CCD	Charge Coupled Device
DI	Differential Interferometer
DNA	Deoxyribonucleic Acid
ELNES	Electron Energy-Loss Near-Edge Structure
ENS	Entrance Slit
EXAFS	Extended X-ray Absorption Fine-Structure
EELS	Electron Energy Loss Spectroscopy
EXS	Exit Slit
EXSY	Vertical Exit Slit
FEL	Free Electron Laser
FTIR	Fourier Transform Infrared Spectroscopy
FTP	File Transfer Protocol
GPIB	General Purpose Interface Bus
GUI	Graphical User Interface
HTML	Hypertext Markup Language
HTTP	Hypertext Transfer Protocol
ICSI	Intracytoplasmic Sperm Injection
IDL	Interactive Data Language
IEEE	Institute of Electrical and Electronics Engineers
IVF	In Vitro Fertilization
NA	Numerical Aperture
NASA	National Aeronautics and Space Administration
NEXAFS	Near-Edge X-ray Absorption Fine-Structure
NMF	Non-Negative Matrix Factorization
NSLS	National Synchrotron Light Source
MSA	Multivariate Statistical Analysis
OSM	Order Sorting Mirrors
OSA	Order Sorting Aperture
PBS	Phosphate Buffered Saline
PCA	Principal Component Analysis
PCI	Peripheral Component Interconnect
PHP	Personal Home Page (Tools)
PNG	Portable Network Graphics
PMAC	Programmable Multi-Axis Controller

SGM	Spherical Grating Monochromator
SSH	Secure Shell
STEM	Scanning Transmission Electron Microscope / Microscopy
STXM	Scanning Transmission X-ray Microscope / Microscopy
SVD	Singular Value Decomposition
TCP/IP	Transmission Control Protocoll / Internet Protocoll
TXM	Transmission X-ray Microscope / Microscopy
XANES	X-ray Absorption Near-Edge Structure
XAS	X-ray Absorption Spectroscopy
X/Y/ZDET	X/Y/Z Axis Detector Stepper Motor Stage
X/YPZT	X/Y Axis Piezo Stage
X/Y/ZSTG	X/Y/Z Axis Sample Stepper Motor Stage
ZOSA	Z Axis OSA Stepper Motor
ZP	Zone Plate

Bibliography

[1] B. Winn, H. Ade, C. Buckley, M. Feser, M. Howells, S. Hulbert, C. Jacobsen, K. Kaznacheyev, J. Kirz, A. Osanna, J. Maser, I. McNulty, J. Miao, T. Oversluizen, S. Spector, B. Sullivan, S. Wang, S. Wirick, and H. Zhang. Illumination for coherent soft x-ray applications: the new X1A beamline at the NSLS. *Journal of Synchrotron Radiation*, 7:395–404, 2000.

[2] J. Stöhr. *NEXAFS Spectroscopy*, volume 25 of *Springer Series in Surface Sciences*. Springer Verlag, Berlin, first edition, 1992.

[3] A. Snigirev, V. Kohn, I. Snigireva, and B. Lengeler. A compound refractive lens for focusing high energy x-rays. *Nature*, 384:49–51, 1996.

[4] M. Born and E. Wolf. *Principles of Optics*. Cambridge University Press, Cambridge, seventh edition, 1999.

[5] J. Kirz. Phase zone plates for X rays and the extreme UV. *Journal of the Optical Society of America*, 64:301–309, 1974.

[6] G. Schmahl and D. Rudolph. Proposal for a phase contrast x-ray microscope. In P. C. Cheng and G. J. Jan, editors, *X-ray Microscopy: Instrumentation and Biological Applications*, pages 231–238, Berlin, 1987. Springer-Verlag.

[7] P. Horowitz and J. A. Howell. A scanning x-ray microscope using synchrotron radiation. *Science*, 178:608–611, 1972.

[8] G. R. Morrison and B. Niemann. Differential phase contrast x-ray microscopy. In Thieme et al. [72], pages I–85–I–94.

[9] M. Feser, B. Hornberger, C. Jacobsen, G. De Geronimo, P. Rehak, P. Holl, and L. Strüder. Integrating silicon detector with segmentation for scanning transmission x-ray microscopy. *Nuclear Instruments and Methods in Physics Research A*, 565:841–854, 2006.

[10] A.L.D. Kilcoyne, T. Tyliszczak, W.F. Steele, S. Fakra, P. Hitchcock, K. Franck, E. Anderson, B. Harteneck, E.G. Rightor, G.E. Mitchell, A.P. Hitchcock, L. Yang, T. Warwick, and H. Ade. Interferometer-controlled scanning transmission x-ray microscopes at the Advanced Light Source. *Journal of Synchrotron Radiation*, 10(2):125–136, 2003.

[11] U. Wiesemann, J. Thieme, R. Früke, P. Guttmann, B. Niemann, D. Rudolph, and G. Schmahl. Construction of a scanning transmission X-ray microscope at the undulator U-41 at BESSY II. *Nuclear Instruments and Methods in Physics Research A*, 467-468:861–863, 2001.

[12] H. Rarback, J. M. Kenney, J. Kirz, M. R. Howells, P. Chang, P. J. Coane, R. Feder, P. J. Houzego, D. P. Kern, and D. Sayre. Recent results from the Stony Brook scanning microscope. In G. Schmahl and D. Rudolph, editors, *X-ray Microscopy*, volume 43 of *Springer Series in Optical Sciences*, pages 203–215, Berlin, 1984. Springer-Verlag.

[13] C. Buckley, H. Rarback, R. Alforque, D. Shu, H. Ade, S. Hellman, N. Iskander, J. Kirz, S. Lindaas, I. McNulty, M. Oversluizen, E. Tang, D. Attwood, R. DiGennaro, M. Howells, C. Jacobsen, Y. Vladimirsky, S. Rothman, D. Kern, and D. Sayre. Soft x-ray imaging with the 35 period undulator at the NSLS. *Review of Scientific Instruments*, 60:2444–2447, 1989.

[14] D. Shu, D. P. Siddons, H. Rarback, and J. Kirz. Two-dimensional laser interferometric encoder for the soft x-ray scanning microscope at the NSLS. *Nuclear Instruments and Methods in Physics Research A*, 266:313–317, 1988.

[15] C. Jacobsen, S. Williams, E. Anderson, M. T. Browne, C. J. Buckley, D. Kern, J. Kirz, M. Rivers, and X. Zhang. Diffraction-limited imaging in a scanning transmission x-ray microscope. *Optics Communications*, 86: 351–364, 1991.

[16] M. Feser, M. Carlucci-Dayton, C. J. Jacobsen, J. Kirz, U. Neuhäusler, G. Smith, and B. Yu. Applications and instrumentation advances with the Stony Brook scanning transmission x-ray microscope. In I. McNulty, editor, *X-ray microfocusing: applications and techniques*, volume 3449, pages 19–29, Bellingham, Washington, 1998. Society of Photo-Optical Instrumentation Engineers (SPIE).

[17] R. DiGennaro, B. Gee, J. Guigli, H. Hogrefe, M. Howells, and H. Rarback. A water cooled mirror system for synchrotron radiation. *Nuclear Instruments and Methods A*, 266:498–506, 1988.

[18] M. Feser. *Scanning transmission x-ray microscopy with a segmented detector*. PhD thesis, Department of Physics and Astronomy, Stony Brook University, 2002.

[19] M. Carlucci Dayton. Nomarski differential phase contrast using a scanning transmission x-ray microscope. Master's thesis, Department of Physics and Astronomy, State University of New York at Stony Brook, 2000.

[20] M. Lerotić. *Finding the patterns in complex specimens by improving the acquisition and analysis of x-ray spectromicroscopy data*. PhD thesis, Department of Physics and Astronomy, Stony Brook University, 2005.

[21] B. Hornberger. *Phase Contrast Microscopy with Soft and Hard X-rays Using a Segmented Detector*. PhD thesis, Department of Physics and Astronomy, Stony Brook University, 2007.

[22] C. Jacobsen, G. Flynn, S. Wirick, and C. Zimba. Soft x-ray spectroscopy from image sequences with sub-100 nm spatial resolution. *Journal of Microscopy*, 197(2):173–184, 2000.

[23] R. C. Gonzalez and R. E. Woods. *Digital Image Processing*. Prentice-Hall, 2nd edition, 2002.

[24] E. R. Malinowski. *Factor analysis in chemistry*. John H. Wiley & Sons, New York, 2^{nd} edition, 1991.

[25] P. L. King, R. Browning, P. Pianetta, I. Lindau, M. Keenlyside, and G. Knapp. Image-processing of multispectral x-ray photoelectron-spectroscopy images. *Journal of Vacuum Science and Technology A*, 7 (6):3301–3304, 1989.

[26] A. Osanna and C. Jacobsen. Principle component analysis for soft x-ray spectromicroscopy. In W. Meyer-Ilse, T. Warwick, and D. Attwood, editors, *X-ray Microscopy: Proceedings of the Sixth International Conference*, pages 350–357, Melville, NY, 2000. American Institute of Physics. ISBN 1-56396-926-2.

[27] B. S. Everitt, S. Landau, and M. Leese. *Cluster Analysis*. Arnold Publishers, London, fourth edition, 2001. ISBN 0-340-76119-9.

[28] M. Lerotic, C. Jacobsen, T. Schäfer, and S. Vogt. Cluster analysis of soft x-ray spectromicroscopy data. *Ultramicroscopy*, 100(1–2):35–57, 2004. doi: 10.1016/j.ultramic.2004.01.008.

[29] M. Lerotic, C. Jacobsen, J.B. Gillow, A.J. Francis, S. Wirick, S. Vogt, and J. Maser. Cluster analysis in soft x-ray spectromicroscopy: finding the patterns in complex specimens. *Journal of Electron Spectroscopy and Related Phenomena*, 144–147:1137–1143, 2005.

[30] D. D. Lee and S. Seung. Learning the parts of objects by non-negative matrix factorization. *Nature*, 401:788–791, 1999.

[31] P.G. Kotula, M.R. Keenan, and J.R. Michael. Automated analysis of SEM X-ray spectral images: A powerful new microanalysis tool. *Microscopy and Microanalysis*, 9:1–17, 2003. doi: 10.1017/S1431927603030058.

[32] N. Bonnet, E. Simova, S. Lebonvallet, and H. Kaplan. New applications of multivariate statistical analysis in spectroscopy and microscopy. *Ultramicroscopy*, 40:1–11, 1992.

[33] K. Kaznacheyev, A. Osanna, C. Jacobsen, O. Plashkevych, O. Vahtras, H. Ågren, V. Carravetta, and A.P. Hitchcock. Innershell absorption spectroscopy of amino acids. *Journal of Physical Chemistry A*, 106(13):3153–3168, 2002.

[34] S. Sandford, J. Aléon, C. Alexander, T. Araki, S. Bajt, G. Baratta, J. Borg, J. Bradley, D. Brownlee, J. Brucato, M. Burchell, H. Busemann, A. Butterworth, S. Clemett, G. Cody, L. Colangeli, G. Cooper, L. D'Hendecourt, Z. Djouadi, J. Dworkin, G. Ferrini, H. Fleckenstein, G. Flynn, I. Franchi, M. Fries, M. Gilles, D. Glavin, M. Gounelle, F. Grossemy, C. Jacobsen, L. Keller, D. Kilcoyne, J. Leitner, G. Matrajt, A. Meibom, V. Mennella, S. Mostefaoui, L. Nittler, M. Palumbo, D. Papanastassiou, F. Robert, A. Rotundi, C. Snead, M. Spencer, F. Stadermann, A. Steele, T. Stephan, P. Tsou, T. Tyliszczak, A. Westphal, S. Wirick, B. Wopenka, H. Yabuta, R. Zare, and M. Zolensky. Organics captured from comet 81P/Wild 2 by the stardust spacecraft. *Science*, 314 (5806):1720–1724, 2006. doi: 10.1126/science.1135841.

[35] D. Brownlee, P. Tsou, J. Aléon, C. Alexander, T. Araki, S. Bajt, G. Baratta, R. Bastien, P. Bland, P. Bleuet, J. Borg, J. Bradley, A. Brearley, F. Brenker, S. Brennan, J. Bridges, N. Browning, J. Brucato, E. Bullock, M. Burchell, H. Busemann, A. Butterworth, M. Chaussidon, A. Cheuvront, M. Chi, M. Cintala, B. Clark, S. Clemett, G. Cody, L. Colangeli, G. Cooper, P. Cordier, C. Daghlian, Z. Dai, L. D'Hendecourt, Z. Djouadi, G. Dominguez, T. Duxbury, J. Dworkin,

D. Ebel, T. Economou, S. Fakra, S. Fairey, S. Fallon, G. Ferrini, T. Ferroir, H. Fleckenstein, C. Floss, G. Flynn, I. Franchi, M. Fries, Z. Gainsforth, J.-P. Gallien, M. Genge, M. Gilles, P. Gillet, J. Gilmour, D. Glavin, M. Gounelle, M. Grady, G. Graham, P. Grant, S. Green, F. Grossemy, L. Grossman, J. Grossman, Y. Guan, K. Hagiya, R. Harvey, P. Heck, G. Herzog, P. Hoppe, F. Hörz, J. Huth, I. Hutcheon, K. Ignatyev, H. Ishii, M. Ito, D. Jacob, C. Jacobsen, S. Jacobsen, S. Jones, D. Joswiak, A. Jurewicz, A. Kearsley, L. Keller, H. Khodja, D. Kilcoyne, J. Kissel, A. Krot, F. Langenhorst, A. Lanzirotti, L. Le, L. Leshin, J. Leitner, L. Lemelle, H. Leroux, M.-C. Liu, K. Luening, I. Lyon, G. MacPherson, M. Marcus, K. Marhas, B. Marty, G. Matrajt, K. McKeegan, A. Meibom, V. Mennella, K. Messenger, S. Messenger, T. Mikouchi, S. Mostefaoui, T. Nakamura, T. Nakano, M. Newville, L. Nittler, I. Ohnishi, K. Ohsumi, K. Okudaira, D. Papanastassiou, R. Palma, M. Palumbo, R. Pepin, D. Perkins, M. Perronnet, P. Pianetta, W. Rao, F. Rietmeijer, F. Robert, D. Rost, A. Rotundi, R. Ryan, S. Sandford, C. Schwandt, T. See, D. Schlutter, J. Sheffield-Parker, A. Simionovici, S. Simon, I. Sitnitsky, C. Snead, M. Spencer, F. Stadermann, A. Steele, T. Stephan, R. Stroud, J. Susini, S. Sutton, Y. Suzuki, M. Taheri, S. Taylor, N. Teslich, K. Tomeoka, N. Tomioka, A. Toppani, J. Trigo-Rodríguez, D. Troadec, A. Tsuchiyama, A. Tuzzolino, T. Tyliszczak, K. Uesugi, M. Velbel, J. Vellenga, E. Vicenzi, L. Vincze, J. Warren, I. Weber, M. Weisberg, A. Westphal, S. Wirick, D. Wooden, B. Wopenka, P. Wozniakiewicz, I. Wright, H. Yabuta, H. Yano, E. Young, N. Zare, T. Zega, K. Ziegler, L. Zimmerman, E. Zinner, and M. Zolensky. Comet 81P/Wild 2 under a microscope. *Science*, 314(5806):1711–1716, 2006. doi: 10.1126/science.1135840.

[36] B. L. Henke, E. M. Gullikson, and J. C. Davis. X-ray interactions: Photoabsorption, scattering, transmission, and reflection at E=50–30,000 eV, Z=1–92. *Atomic Data and Nuclear Data Tables*, 54:181–342, 1993.

[37] C. Jeanguillaume and C. Colliex. Spectrum-image: The next step in eels digital acquisition and processing. *Ultramicroscopy*, 28:252–257, 1989.

[38] J.A. Hunt and D.B. Williams. Electron energy-loss spectrum-imaging. *Ultramicroscopy*, 38:47–73, 1991.

[39] H. Ade, X. Zhang, S. Cameron, C. Costello, J. Kirz, and S. Williams. Chemical contrast in x-ray microscopy and spatially resolved XANES spectroscopy of organic specimens. *Science*, 258:972–975, 1992.

[40] X. Zhang, R. Balhorn, J. Mazrimas, and J. Kirz. Mapping and measuring

DNA to protein ratios in mammalian sperm head by XANES imaging. *Journal of Structural Biology*, 116:335–344, 1996.

[41] I. N. Koprinarov, A. P. Hitchcock, C. T. McCrory, and R. F. Childs. Quantitative mapping of structured polymeric systems using singular value decomposition analysis of soft x-ray images. *Journal of Physical Chemistry B*, 106:5358–5364, 2002.

[42] N. Bonnet, E. Simova, S. Lebonvallet, and H. Kaplan. New applications of multivariate statistical analysis in spectroscopy and microscopy. *Ultramicroscopy*, 40:1–11, 1992.

[43] N. Bonnet, N. Brun, and C. Colliex. Extracting information from sequences of spatially resolved EELS spectra using multivariate statistical analysis. *Ultramicroscopy*, 77:97–112, 1999.

[44] D. D. Lee and S. Seung. Algorithms for non-negative matrix factorization. *Advances in Neural Information Processing Systems 13: Proceedings of the 2000 Conference*, pages 556–562, 2001.

[45] S. Kullback and R. A. Leibler. On information and sufficiency. *The Annals of Mathematical Statistics*, 22(1):79–86, 1951.

[46] T. Feng, S. Z. Li, H.-Y. Shum, and H. Zhang. Local nonnegative matrix factorization as a visual representation. *Proceedings of the 2nd International Conferenc on Development and Learning*, pages 178–183, 2002.

[47] P. O. Hoyer. Non-negative sparse coding. *Proceedings of the IEEE Workshop on Neural Networks for Signal Processing*, pages 557–565, 2002.

[48] W. Liu, N. Zheng, and X. Lu. Non-negative matrix factorization for visual coding. *Proceedings of the IEEE International Conference on Acoustics, Speech, and Signal Processing*, 3:293–296, 2003.

[49] P. O. Hoyer. Non-negative matrix factorization with sparseness constraints. *Journal of Machine Learing Research*, 5:1457–1469, 2004.

[50] A. Pascual-Montano, K. Kochi, D. Lehmann, and R. D. Pascual-Marqui. Nonsmooth nonnegative matrix factorization. *IEEE Transactions on Pattern Analysis and Machine Intelligence*, 28(3):403–415, 2006.

[51] H.T. Gao, T.H. Li, K. Chen, W.G. Li, and X. Bi. Overlapping spectra resolution using non-negative matrix factorization. *Talanta*, 66:65–73, 2005.

[52] G. Cody, H. Ade, C. Alexander, T. Araki, A. Butterworth, H. Fleckenstein, G. Flynn, M. Gilles, C. Jacobsen, A. Kilcoyne, K. Messenger, S. Sandford, T. Tyliszcak, A. Westphal, S. Wirick, and H. Tabuta. Quantitative organic and light element analysis of comet Wild 2 particles using C-, N-, O- Micro-XANES. *Meteoritics & Planetary Science*, submitted, 2008.

[53] A. Toppani, F. Robert, G. Libourel, P. de Donato, O. Barres, L. d'Hendecourt, and J. Ghanbaja. A 'dry' condensation origin for circumstellar carbonates. *Nature*, 437:1121–1124, 2005. doi: 10.1038/nature04128.

[54] S. M. Kirtley, O. C. Mullins, J. Chen, J. van Elp, S. J. George, C. T. Chen, T. O'Halloran, and S. P. Cramer. Nitrogen chemical structure in DNA and related molecules by x-ray absorption spectroscopy. *Biochimica et Biophysica Acta*, 1132:249–254, 1992.

[55] A. P. Hitchcock, C. Morin, Y. M. Heng, R. M. Cornelius, and J. L. Brash. Towards practical soft x-ray spectromicroscopy of biomaterials. *Journal of Biomaterials Science. Polymer Edition*, 13(8):919–937, 2002.

[56] C. Jacobsen, R. Medenwaldt, and S. Williams. A perspective on biological x-ray and electron microscopy. In Thieme et al. [72], pages II–93–102.

[57] R. Grimm, H. Singh, R. Rachel, D. Typke, W. Zillig, and W. Baumeister. Electron tomography of ice-embedded prokaryotic cells. *Biophysical Journal*, 74:1031–1042, 1998.

[58] E. G. Rightor, A. P. Hitchcock, H. Ade, R. D. Leapman, S. G. Urquhart, A. P. Smith, G. Mitchell, D. Fischer, H. J. Shin, and T. Warwick. Spectromicroscopy of poly(ethylene terephthalate): comparison of spectra and radiation damage rates in x-ray absorption and electron energy loss. *Journal of Physical Chemistry*, B 101(11):1950–1960, 1997.

[59] T. Beetz and C. Jacobsen. Soft x-ray radiation-damage studies in PMMA using a cryo-STXM. *Journal of Synchrotron Radiation*, 10(3):280–283, 2003.

[60] B. W. Loo, Jr., S. Williams, S. Meizel, and S. S. Rothman. X-ray stereomicroscopy: high resolution 3-D imaging of human spermatozoa in aqueous suspension with natural contrast. *Journal of Microscopy*, 166:RP5–RP6, 1992.

[61] T. Vorup-Jensen, T. Hjort, J. V. Abraham-Peskir, P. Guttmann, J. C. Jensenius, E. Uggerhøj, and R. Medenwaldt. X-ray microscopy of human

spermatozoa shows change of mitochondrial morphology during capacitation. *Human Reproduction*, 14:880–884, 1998.

[62] J. Abraham-Peskir, E. Chantler, C. McCann, R. Medenwaldt, and E. Ernst. Ultrastructure of human sperm using x-ray microscopy. *Medical Science Research*, 26:663–667, 1998.

[63] L. Schmidt, K. Munster, and P. Helm. Infertility and the seeking of infertility treatment in a representative population. *British Journal of Obstetric Gynecology*, 102:978–984, 1995.

[64] D. S. Irvine. Epidemiology and aetiology of male infertility. *Human Reproduction*, 13(suppl. 1):33–44, 1996.

[65] Assisted reproductive technology in the united states: 2000 results generated from the american society for reproductive medicine/society for assisted reproductive technology registry. *Fertility and Sterility*, 81(5): 1207–1220, 2004.

[66] J. O'Brien and A. Zini. Sperm DNA integrity and male infertility. *Urology*, 65(1):16–22, 2005.

[67] D. S. Guzick, J. W. Overstreet, P. Factor-Litvak, et al. Sperm morphology, motility, and concentration in fertile and infertile men. *New England Journal of Medicine*, 345(19):1388–1393, 2001.

[68] A. Ahmadi and S. C. Ng. Fertilizing ability of DNA-damaged spermatozoa. *Journal Of Experimental Zoology*, 284(6):696–704, 1999.

[69] C. Cho, H. Jung-Ha, W. D. Willis, et al. Protamine 2 deficiency leads to sperm DNA damage and embryo death in mice. *Biology Of Reproduction*, 69(1):211–217, 2003.

[70] U. B. Hacker-Klom, W. Göhde, E. Nieschlag, and H. M. Behre. DNA flow cytometry of human semen. *Human Reproduction*, 14(10):2506–2512, 1999.

[71] U. Neuhäusler, C. Jacobsen, D. Schulze, D. Stott, and S. Abend. A specimen chamber for soft x-ray spectromicroscopy on aqueous and liquid samples. *Journal of Synchrotron Radiation*, 7:110–112, 2000.

[72] J. Thieme, G. Schmahl, E. Umbach, and D. Rudolph, editors. *X-ray Microscopy and Spectromicroscopy*, Berlin, 1998. Springer-Verlag.